7-2021

Direct Torque Control for Silicon Carbide Motor Drives

Mohammad Hazzaz Mahmud
University of Arkansas, Fayetteville

Direct Torque Control for Silicon Carbide Motor Drives

A dissertation submitted in partial fulfillment
of the requirements for the degree of
Doctor of Philosophy in Engineering with a concentration in Electrical Engineering

by

Mohammad Hazzaz Mahmud
Ahsanullah University of Science and Technology
Bachelor of Science in Electrical and Electronic Engineering, 2013
Lamar University
Master of Science in Electrical Engineering, 2016

July 2021
University of Arkansas

This dissertation is approved for recommendation to the Graduate Council.

Yue Zhao, Ph.D.
Dissertation Director

Juan C. Balda, Ph.D.
Committee Member

Jingxian Wu, Ph.D.
Committee Member

Shengfan Zhang, Ph.D.
Committee Member

ABSTRACT

Direct torque control (DTC) is an extensively used control method for motor drives due to its unique advantages, e.g., the fast dynamic response and the robustness against motor parameters variations, uncertainties, and external disturbances. Using higher switching frequency is generally required by DTC to reduce the torque ripples and decrease stator current total harmonic distortion (THD), which however can lower the drive efficiency. Through the use of the emerging silicon carbide (SiC) devices, which have lower switching losses compared to their silicon counterparts, it is feasible to achieve high efficiency and low torque ripple simultaneously for DTC drives.

To overcome the above challenges, a SiC T-type neutral point clamped (NPC) inverter is studied in this work to significantly reduce the torque and flux ripples which also effectively reduce the stator current ripples, while retaining the fast-dynamic response as the conventional DTC. The unbalanced DC-link is an intrinsic issue of the T-type inverter, which may also lead to higher torque ripple. To address this issue, a novel DTC algorithm, which only utilizes the real voltage space vectors and the virtual space vectors (VSVs) that do not contribute to the neutral point current, is proposed to achieve inherent dc-link capacitor voltage balancing without using any DC-link voltage controls or additional DC-link capacitor voltages and/or neutral point current sensors.

Both dynamic performance and efficiency are critical for the interior permanent-magnet (IPM) motor drives for transportation applications. It is critical to determine the optimal reference stator flux linkage to improve the efficiency further of DTC drives and maintain the stability of the drive system, which usually obtained by tuning offline and storing in a look-up table or calculated online using machine models and parameters. In this work, the relationship between the stator flux linkage and the magnitude of stator current is analyzed mathematically. Then, based on this

relationship, a perturb and observe (P&O) method is proposed to determine the optimal flux for the motor which does not need any prior knowledge of the machine parameters and offline tuning. However, due to the fixed amplitude of the injected signal the P&O algorithm suffers from large oscillations at the steady state conditions. To mitigate the drawback of the P&O method, an adaptive high frequency signal injection based extremum seeking control (ESC) algorithm is proposed to determine the optimal reference flux in real-time, leading to a maximum torque per ampere (MTPA) like approach for DTC drives. The stability analysis and key parameters selection for the proposed ESC algorithm are studied. The proposed method can effectively reduce the motor copper loss and at the same time eliminate the time consuming offline tuning effort. Furthermore, since the ESC is a model-free approach, it is robust against motor parameters variations, which is desirable for IPM motors.

ACKNOWLEDGEMENT

Throughout my doctoral journey I had the opportunity to know so many great people who has not only helped me directly in my research but also helped me to bring out the best out of me in every situation and supported me all the way. I am thankful to all those people who have made this dissertation possible and because of them my Ph.D. experience has become one of the fondest that I have.

Ph.D. journey for a student is not an easy path to walk alone. In pursuing this difficult path, first and foremost, I am forever grateful to my advisor Dr. Yue Zhao, for his constant support and encouragement which help me not only technically but also in many personal aspects. I want to thank him for spending endless hours going through my research papers and providing his insightful suggestions which helped me to improve the quality of writing. I also want to thank him for his patience, guidance, positivity, and inspiring attitude.

I am also thankful to my dissertation advisory committee members: Dr. Juan C. Balda, Dr. Jingxian Wu and Dr. Shengfan Zhang for their interests in my research, generous support, and suggestions to improve my research work. I cannot be more pleased to have them in my committee.

I would like to acknowledge my colleagues, my friends and lab mates, who for their creative support, encouragement, and collaboration. First, I would like to thank three of my dearest friends and colleagues, Dr. Waleed Saad S. Alhosaini, Yuheng Wu and Tylor Adamson. Additionally, I would also like to thank my other lab mates and friends. Thank you very much, Eric Allee, Fei Diao, Nan Lin, Xinyuan Du, Zhuxuan Ma, Dr. Shuang Zhao, Dr. Yufei Li, Shamar Christian, Dr. Roberto Fantino, Vinson Jones, Haider Mhiesan, Dr. Sajib Roy, Bakhtiyar Mohammad Nafis, and

Ahmed Rahouma. I would also like to thank from my heart to Dr. Chris Farnell for his support in testing hardware and his valuable suggestions.

Lastly and most importantly, I am deeply indebted to my beloved parents and would be honored to thank cordially my mother Hasina Mahmud and my father Sultan Mahmud. It is you who brought me to this beautiful world and made me who I am today; I am and will always be proud of you. Mi amor (my love) Samia Afroz, my beautiful wife, without you, it would not be possible to finish this dissertation. Thank you for your patience and without your support this Ph.D. journey would not be possible. I would love to thank my cousin brother Tuhin, who loved me and encourage me from my childhood to pursue higher studies. My grandmother Jhorna Hoque, thank you for your love and care.

Financial support from the following institutions/organizations is gratefully acknowledged:

- National Science Foundation (NSF), USA
- University of Arkansas, USA

DEDICATION

This dissertation is dedicated to

my mother “Hasina Mahmud”, my father “Sultan Mahmud” and my lovely wife “Samia Afroz”.

LIST OF CONTENTS

LIST OF TABLES

LIST OF FIGURES

CHAPTER 1

INTRODUCTION

1.1 Background and Motivation

Electric motors, e.g., both the direct current (DC) motors and alternating current (AC) motors, have been widely used in our daily life, such as in the refrigerators, vacuum cleaners, air conditioners, fans, computers, automatic car windows, electric cars, aircrafts and in a very large portion of industrial process from general purpose speed drives, e.g., pumps and conveyors, to high-performance servo controls, e.g., robotics and motion control, making the manufacturers more prolific and the world more sustainable [1-3]. Although last century, the DC motors were popular since their control were simple to implement and had better dynamic performances, however AC motors are gaining tractions over last few decades due to their structural advantages, easy to maintain and comparatively lower cost. Additionally, the advancement of switch mode converters in the power electronics field and the control theory, AC machines such as permanent magnet synchronous motor (PMSM) are becoming more widely used motor. The PMSM holds advantages over other various types of AC machines such as high power density, high reliability and high efficiency [4].

The performance of the PMSM drive system is largely dependent on the control algorithm applied for it. Motor control algorithms can be divided generally into two categories, i.e., the scaler control and the vector control. Due to the non-ideal transient response of the scaler control approach, the vector control is vastly accepted in the industrial applications. Among vector controls, the field-oriented control (FOC) and direct torque control (DTC) are well known in the machine drive field. To eliminate the complex coordinate transformation and the current-voltage regulator which are the major parts of the FOC system, DTC was first introduced by Takahashi,

Noguchi [5] and Depenbrock [6], and gained attention over the following few decades. The DTC has been adopted in various industrial applications, due to its advantages, such as fast dynamic response and robustness to system uncertainties and nonlinearities. However, compared to the FOC, the DTC may suffer from much higher torque ripple and also higher total harmonic distortion (THD) in the motor stator currents [6]. To reduce torque ripple, higher switching frequency is usually required by DTC, which however increases the switching loss and consequently lower the drive efficiency. Adopting silicon carbide (SiC) devices, which can operate much higher switching frequency than their silicon (Si) counterparts without compromising efficiency much, it would be a reasonable solution to achieve higher efficiency, lower torque ripple and less stator current harmonics [7]. Figure 1.1 shows a typical block diagram for the DTC which includes torque and flux hysteresis, switching table, voltage/current calculation, flux and torque calculation and a sector detector.

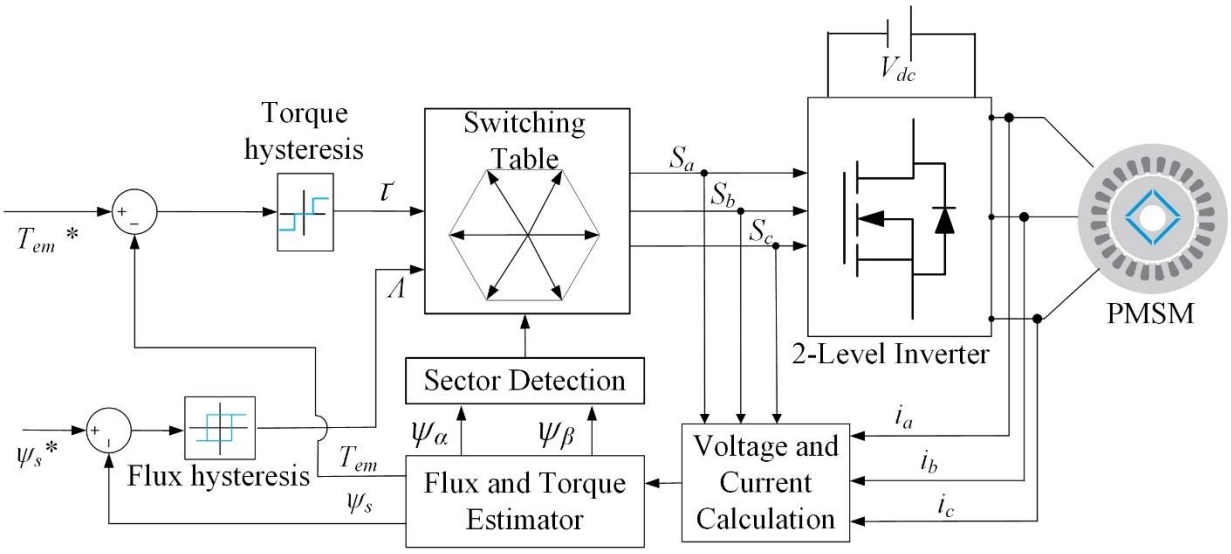

Figure 1.1: A block diagram of conventional switching table based DTC.

Various improved DTC methods have been proposed to address the downsides of the conventional DTC. Improvements have been obtained through the use of enhanced modulation

techniques and more effective DTC algorithms. For example, the duty-cycle based DTCs [8-12] were presented to reduce the torque ripple, where two [8], [10] or more [12] voltage vectors are applied over one control cycle. These methods depend on a simple modulator based driving signal generation to realize constant switching frequency [13], which however leads to much higher switching losses and ultimately low efficiency. From the algorithm standpoint, to decrease the torque and flux ripples while holding the merit such as the fast-dynamic response, the direct torque and flux control (DTFC) [14]-[15], dead-beat control [16], predictive DTC [17]-[18] and the space-vector-modulated (SVM) DTC [19] have been proposed.

Additionally, to reduce the torque ripple apart from the control point of view, the drive performance improvement can also be achieved by hardware innovations, e.g., employing the multilevel inverters (MLIs) instead of the conventional two-level (2-L) inverters, especially for the medium- or high-voltage high power drives. Higher number of voltage levels can be generated by adopting the MLIs, which can potentially reduce *dv/dt*, common mode voltages, torque ripple, and current THD. Among all MLIs [20-22], the most widely adopted one for medium voltage variable speed drives is the three-level (3-L) neutral point clamped (NPC) inverter [23-30]. Comparing to the 2-L inverters, the DTC drives for 3-L NPC inverter systems have much lower torque and flux ripples since they have higher number of available voltage vectors which helps to increase the output voltage levels. However, the DC-link voltage balancing is a primary challenge for the 3-L inverters due to the oscillations of the neutral-point (NP) voltage, which can cause excessive voltage stress on the power devices and DC-link capacitors [31]. In addition, the DC-link capacitors and power semiconductor devices will deteriorate over time due to the lower order harmonics [32] generated from the NP voltage oscillations. A modified SVM-DTC approach was suggested in [33] where the medium voltage vectors are neglected which generally cause the NP

unbalancing, and the measured DC-link capacitor voltages are employed to select appropriate small voltage vectors. References [34] and [35] have shown two different modified control strategies for 3-L DTC drive where DC-link capacitor voltages and/or NP currents are measured to find the optimal voltage vector with zero neutral point current. In the aforementioned DTC drives for 3-L converters, sensors are utilized to measure the NP voltage and/or current which is costly and they need active feedback control which makes the control loop complex. Therefore, it is necessary to develop a novel DTC approach for the 3-L converter-fed PMSM with inherent DC-link capacitor voltage balancing capabilities and enhance the reliability of the overall system.

The maximum torque per ampere (MTPA) strategy is often necessary for modern AC drives that are generally implemented for FOC to improve the efficiency and power density of the system. The MTPA algorithm is used to generate required electromagnetic torque using the smallest stator current, such that the motor copper losses can be minimized. The MTPA for FOC can be comprehended through either offline turning or online optimization. As proposed in [36-38], optimal *d*-axis current reference can be represented as a function of torque and motor parameters through offline characterization or curve fitting or using LUT which needs the machine parameters information, e.g., stator resistance, inductances, etc. and dependent on the machine model. It is obvious that the more precise the measured parameters and the loss information, the more effective those MTPA methods. Therefore, they are sensitive to the parametric variations and need extensive offline data processing that add additional burden to the controller. To address these issues, a MTPA method which uses an online optimization based on machine model is proposed in [39]. A similar MTPA technique is presented in [40] where first the problem were formulated as a nonlinear optimization problem and then solved by using Lagrange multiplier method in real time. This method does not need any time consuming off-line tuning effort; however, this is yet sensitive

to the accuracy of parameters. Some other control strategies are mentioned where a small perturbation is added the *d*-axis current reference [41]-[42] or current control angle [43] to achieve MTPA in real-time. These methods are known as signal injection based approaches. It is possible to identify the MTPA operating points based on the response of the drive system to the perturbations. These signal injection methods do not need any machine parameters for their operation. However, the major drawbacks of the injection based method are that if the small perturbation signals are not selected carefully then it may affect the normal operation by introducing oscillations and slow convergence rate of the method can affect the dynamic performance of the drive system. Recently, virtual signal injection based approach has been gained attention in several papers for FOC [44-46]. These methods do not affect the normal operation of motors since no actual signal is injected. However, these methods may suffer from the slow converging rate and poor dynamic response.

As mentioned earlier in this section, compared to the FOC, the DTC approach owns several advantages, such as fast dynamic response, less numbers of parameters needed in the controller since it does not need complex coordinate transformation and does not require rotor position sensing as well. For a certain application of DTC, the fast dynamic response, robustness, and efficiency of the system can be achieved by achieving the proper flux linkage angle, as claimed in [47]. It has been presented that when the drive operates at constant flux linkage magnitude at all loads, it may result in poor efficiency at light load. Enhancing the efficiency for DTC schemes can be achieved in several ways, e.g., LUT based and online optimization approaches. The LUT based approach is the most commonly used in DTC to determine the references torque and flux [14], [48], and [49]. In these approaches, the reference flux linkage is stored in a LUT based on the reference torque command and the speed. Since it needs tremendous offline data measurement and

tuning effort, the LUT based DTC is time consuming and may be affected by the variation of the machine parameters. To address these issues by realizing MTPA for DTC, a direct calculation method of reference flux linkage is presented in [50] and [51], which relies on the mathematical machine model in the *d-q* reference frame and machine parameters. To eliminate the dependency of machine parameters in the MTPA method, signal injection based methods are proposed like perturb and observe (P&O) in [28], [52] and [36] to detect MTPA points online. In [52], an online reference flux correction method is proposed based on the sequential variation of the actual current to an optimal point by correcting the reference stator flux linkage using a local search algorithm to minimize the current. Another method is proposed in [28], where a P&O searching algorithm is proposed to determine the optimal reference flux. In [36], a random frequency signal is added to the reference flux to avoid the residual torque harmonic at the injected signal frequency. All these abovementioned signal injection based approach for MTPA searching are independent to machine parameters, however, the robustness against the ripple and/or noise in torque and stator current is not comprehensively analyzed. Therefore, the DTC drives need to be thoroughly investigated to further improve the efficiency by developing a robust and stable online MTPA operating point searching algorithm which is totally independent to machine parameters with faster dynamic performance.

1.2 Research Objectives and Challenges

The goal of the research for this dissertation is to study and design advanced DTC methods for the drive system using multi-level converters, e.g., the T-type converter without compromising the dynamic performance comparing to the conventional DTC and minimize the torque and flux ripples. Additionally, the novel DTC will ensure the DC-link capacitor voltage balancing for the T-type converter without utilizing any neutral point voltage/current measurement. To improve the

efficiency of the DTC further by reducing the copper loss, novel flux searching algorithms are presented and validated. The new online flux searching approaches do not need any machine model information, therefore, it is a model free approach. In addition, the proposed approach is studied in detail with stability analysis and boundary conditions.

The main objectives of this this dissertation include,

- Developing a novel DTC for T-type NPC inverter. The new DTC should have inherent DC-link capacitor voltage balancing by ensuring that the neutral point current over one switching cycle is zero. Therefore, the effect of unbalanced DC-link on the torque and flux ripples can be eliminated.
- Developing a new multi-layer voltage vector diagram by introducing virtual voltage vector concept for DTC. However, the dynamic performance of the proposed DTC needs to be similar to the conventional DTC which is desirable. The VSV based DTC will have higher average switching frequency comparing to the conventional DTC which will be helpful to reduce the torque and stator current ripples further.
- Enhancing the efficiency in the DTC drive system by ensuring the MTPA operating condition. Developing multiple optimal flux searching approaches online and comparing their performances are two of the important objectives of the dissertation.
- Developing an electro-thermal characterization procedure to achieve loss data and compare different control algorithm in terms of their loss and efficiency. The loss model can be used as a standard procedure to study the control method and characterize the drive system.

1.3 Dissertation Organization

This dissertation is organized as follows:

- Chapter 2 describes the detailed mathematical model of the PMSM and the two commonly used converter topologies; NPC and T-type NPC converters. The topologies are modeled, and the circuit diagrams are presented with their merits and demerits. Then the DC-link capacitor selection procedure is presented. The brief description of the control approaches for the PMSM are studied and explained along with their control diagrams, i.e., scaler control and vector control which includes FOC and DTC.
- Chapter 3 includes the introduction to the conventional DTC algorithms and stability analysis of the DTC. The ripple analysis which includes torque and flux ripples are studied and shown in mathematical forms.
- Chapter 4 explores the conventional and proposed DTC for the T-type NPC converter and compare their performances. The generation of the proposed virtual voltage vectors is elaborately discussed and their effect on the DC-link capacitor voltage balancing are analyzed.
- Chapter 5 explains the MTPA for IPM motor. Then two optimal flux searching approaches are presented, i.e., P & O and ESC. The control approach is developed with proper boundary condition and stability analysis. For the ESC, the selection criterion of the high frequency signal is also proposed.
- In Chapter 6, an electro-thermal characterization procedure is proposed, and the results are presented to compare the proposed MATLAB/Simulink based loss model and the experimental data.
- Chapter 7 shows the simulation and experimental setups for all of the proposed methods.
- Chapter 8 validates the proposed control methods by performing numerous simulation and experimental studies.

- Chapter 9 provides the conclusions, contributions, and the future research recommendations for the work proposed in this dissertation.

CHAPTER 2

SYSTEM MODELING OF THE TRACTION DRIVES AND PERMANENT MAGNET SYNCHRONOUS MOTOR

2.1 Introduction

A permanent magnet synchronous motor (PMSM) is one kind of synchronous motors which runs at constant speed irrespective of the amount of loading on the motor. This is a distinct advantage of the PMSM for constant speed motor drive applications. Depending on the application and operation mode, there are several control approaches for PMSM, e.g., scaler control and vector control. Scaler control is easy to implement comparing to vector control but has drawbacks with poor dynamic and steady state performances. To design a control algorithm, the first and foremost thing to determine is the machine model in mathematical form to understand its dynamic behaviors. In addition to the motor model, the converters are also important element in the system which helps to run the motor based on the control signal. That's why it is important to understand the converter model as well. In general, for motor drive two-level (2-L) inverter or three-level (3-L) inverters are used. Although the basic functionality of the converters is same, however, the switching sequence can be different for different topologies.

Therefore, in this chapter mathematical model of the PMSM is derived first in different reference frame. Then the 2-L and 3-L converter topologies are analyzed, and their advantages and disadvantages are discussed. Next the control approaches for the PMSM are presented and briefly shown it this chapter. Besides the topologies the DC-link capacitance calculation method is also included.

2.2 Mathematical Model of Permanent Magnet Synchronous Motor

Before developing the mathematical model of the PMSM it is important to understand that any AC machines is time-variant, multivariable, nonlinear, and coupling system. Also, from construction perspective and considering the permanent magnets placement, a PMSM with an approximately sinusoidal back electromotive force (EMF) can be classified salient-pole PMSM, e.g., interior PMSMs, and non-salient-pole PMSMs (IPMSM), e.g., surface-mounted PMSMs (SPMSM). Since the IPMSM has permanent magnet mounted inside the rotor, in high-speed operation the rotor iron can protect the permanent magnets from the centrifugal force. In contrast the SPMSMs have the permanent magnets embedded on the surface of the rotor core which is good in low-speed applications [53-55]. The typical PMSM cross-section is shown in Figure 1.1, where Figure 1(a) represents the cross-section of SPMSM, and Figure 1(b) is the cross-section of the IPMSM. It is to be noted that because of the rotor saliency, the *d*-axis and *q*-axis inductances are different in IPMSM. In general, both types of permanent magnet motor have similar operating principle in terms of using permanent magnet generated toque and reluctance torque for maximum output torque.

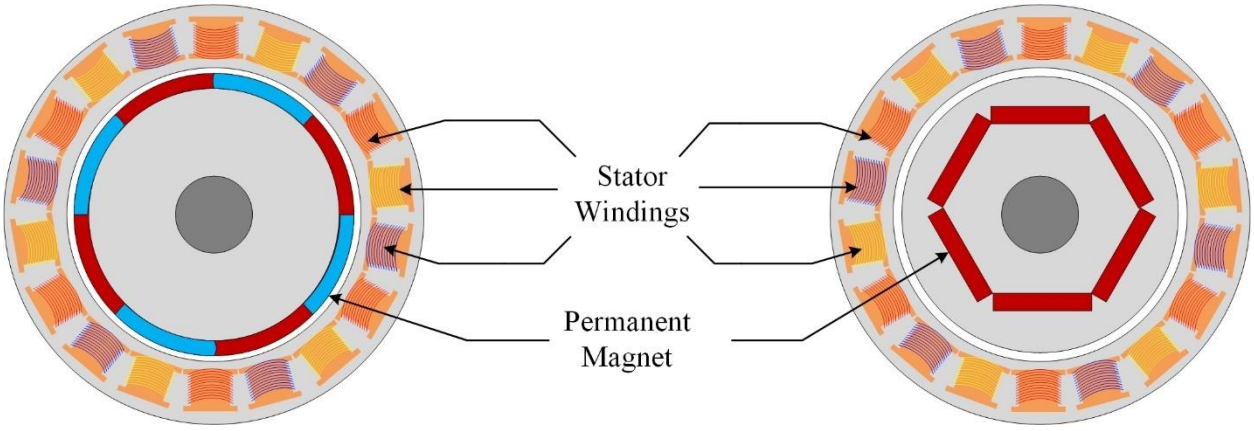

Figure 2.1: (a) cross-section of SPMSM and (B) cross-section of IPMSM.

The dynamics of a three-phase IPMSM can be modeled in synchronously rotating *dq* reference frame as

$$\begin{bmatrix} v_d \\ v_q \end{bmatrix} = \begin{bmatrix} R + sL_d & -\omega_{re} L_q \\ \omega_{re} L_d & R + sL_q \end{bmatrix} \begin{bmatrix} i_d \\ i_q \end{bmatrix} + \begin{bmatrix} 0 \\ \omega_{re} \psi_m \end{bmatrix} \tag{2.1}$$

where s is a derivative operator, v_d and v_q are the *d*- and *q*-axis stator voltages respectively; ω_{re} is the rotor electrical angular speed; L_d and L_q are the *d*- and *q*-axis inductances, respectively; i_d and i_q are the *d*- and *q*-axis stator currents, respectively; ψ_m is the flux linkage produced by the permanent magnets, and *R* is the stator resistance. ψ_d and ψ_q are the *d*- and *q*-axis components of the stator flux linkage vector and can be represented as

$$\begin{bmatrix} \psi_d \\ \psi_q \end{bmatrix} = \begin{bmatrix} \psi_m + L_d i_d \\ L_q i_q \end{bmatrix} \tag{2.2}$$

From equation (2.2), $|\psi_s|$ can be calculated as

$$|\psi_s| = \sqrt{(\psi_d)^2 + (\psi_q)^2} = \sqrt{(\psi_m + L_d i_d)^2 + (L_q i_q)^2} \tag{2.3}$$

The electromagnetic torque, T_{em} generated by an IPMSM can be denoted in the *dq* rotor reference frame as

$$T_{em} = \frac{3}{2} P \left[\psi_m + (L_d - L_q) i_d \right] \cdot i_q \tag{2.4}$$

where *P* is the pole-pairs number. Note that for salient pole PMSM, $L_d \neq L_q$ and for non-salient pole PMSM, $L_d = L_q$. T_{em} can be also calculated in terms of stator flux linkage, $|\psi_s|$ and load angle, δ, which can be shown as

$$T_{em} = \frac{3}{2}\frac{P}{L_d}|\psi_s|\psi_m \sin\delta + \frac{3}{2}\frac{P}{L_d L_q}|\psi_s|^2 \left(L_d - L_q\right)\sin\left(2\delta\right)$$
$$= \frac{3}{2}\frac{P}{L_d}|\psi_s|\left[\psi_m + (L_d - L_q)i_d\right]\sin\delta \tag{2.5}$$

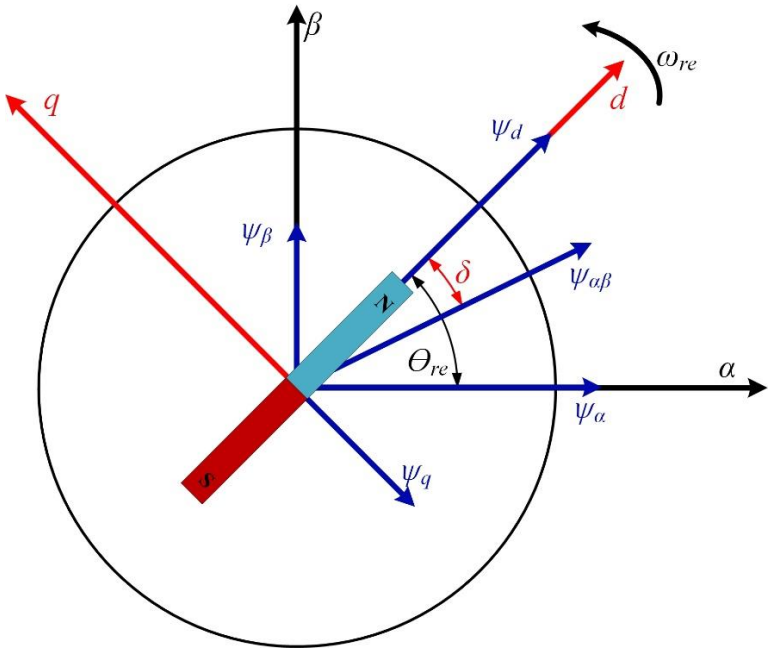

Figure 2.2: Stator flux in *αβ* stationary and synchronous rotating *dq* reference fames.

The motor dynamics explained in *dq* reference frame from (2.1) to (2.5) can be expressed in stationary reference frame *αβ* using inverse park transformation technique as shown below,

$$\begin{bmatrix} v_\alpha \\ v_\beta \end{bmatrix} = \begin{bmatrix} R & \omega_{re}\left(L_d - L_q\right) \\ -\omega_{re}\left(L_d - L_q\right) & R \end{bmatrix}\begin{bmatrix} i_\alpha \\ i_\beta \end{bmatrix} + \begin{bmatrix} s\psi_\alpha \\ s\psi_\beta \end{bmatrix} \tag{2.6}$$

where v_α and v_β are the α- and β-axis stator voltages respectively; i_α and i_β are the α- and β-axis stator currents, respectively. ψ_α and ψ_β are the α- and β-axis components of the stator flux linkage vector. T_{em} can be also calculated in terms of stator flux linkage,

$$T_{em} = \frac{3P}{2}\left(\psi_\alpha i_\beta - \psi_\beta i_\alpha\right) \tag{2.7}$$

2.3 Generic Three-Phase Two-Level Converters

The conventional three-phase two-level (2-L) inverter is most commonly adopted topology among voltage source inverters (VSIs) [56] due to its simplicity in nature and low cost comparing two other multilevel converter topologies. Two-level topology has a smaller number of the power switch comparing to the three phase multilevel topologies, therefore, has less conduction losses. Controls for 2-L inverter is also simple to implement since the 2-L inverter doesn't have neutral point like 3-L topologies. Although the 2-L seems perfect for the most application, there are also some limitations which hinders the adaptation of the 2-L inverter topology. In 2-L inverter the power devices need to handle full DC-link voltage which increase the stress of the devices and eventually affects the lifetime of the devices. This causes the high *dv/dt* and huge current ripples. Having big passive filter is a drawback of the 2-L inverter as well since it has higher THD comparing to the 3-L inverters.

A typical 2-L inverter is shown in the Figure 2.3. There is total six power switches to form a 2-L inverter where each phase is commuted by only two switches. S_{a1} and S_{a2} represent the power device in phase A. C_1 and C_2 represent the DC-link capacitors. Output voltage can be generated based on different switching sequences in six step inverter which gives the output phase voltage waveform as $+V_{dc}/2$ and $-V_{dc}/2$ [57-59].

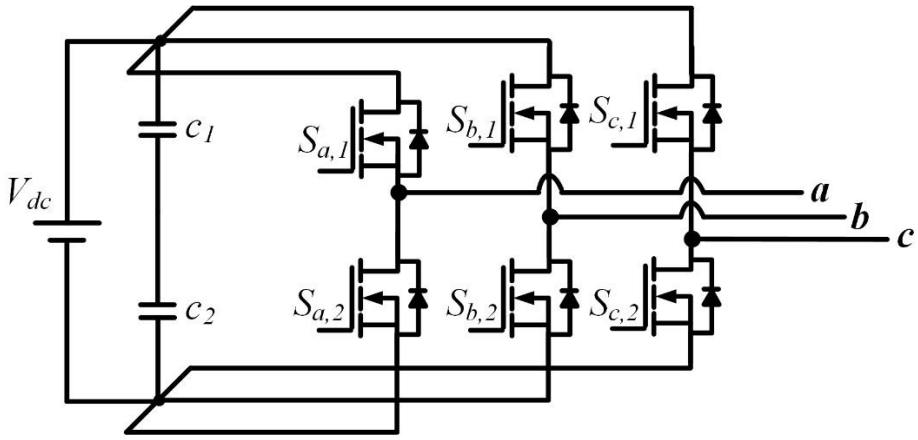

Figure 2.3: Two-level inverter topology.

2.4 Generic Three-Phase Three-Level Converters

The 3-L neutral point clamped (NPC) inverters are the part of the multilevel inverters (MLIs) hierarchy and adopted especially for the medium or high voltage application. The MLIs, e.g., NPC inverter generates higher number of voltage levels at the output which can potentially reduce the *dv*/*dt*, common mode voltage and enhance the output current quality by lowering the THD. Therefore, the output filter size will be reduced significantly [23, 24, 26, 60-62]. Although, NPC has its fair share of advantages over 2-L inverters, due to use of higher number of switching devices the conduction loss can be higher than the conventional 2-L inverters. To overcome this disadvantage of the conventional NPC, a modified NPC has been proposed which is known as T-type NPC. As mentioned earlier NPC suffers from large semiconductor conduction losses since the output current always flows through two switching devices. On the other hand, the T-type NPC utilizes only single outer loop switching device to connect to the upper or lower DC bus voltages which helps to reduce the conduction losses.

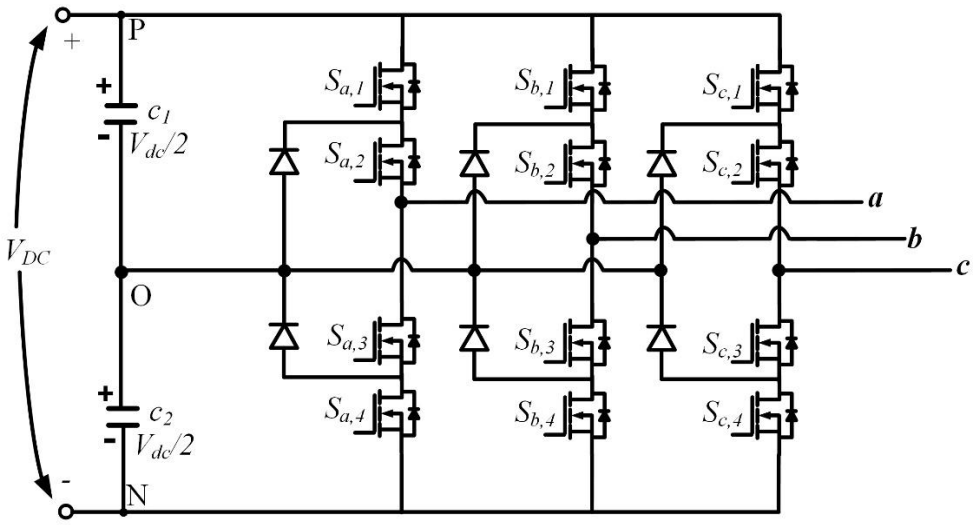

Figure 2.4: Three-level NPC inverter topology.

A typical circuit topology of the NPC inverter is shown in Figure 2.4. Three phases are defined as *a*, *b*, and *c* respectively. Each phase is formed by four semiconductor devices and two clamping diodes. The semiconductor devices are dented as $S_{x,1}$, $S_{x,2}$, $S_{x,3}$, and $S_{x,4}$, where *x* represents the phases, e.g., *x*=*a*, *b*, *c*. In Figure 2.4, the semiconductor devices are shown as $S_{a,1}$, $S_{a,2}$, $S_{a,3}$, and $S_{a,4}$ for phase *a*.

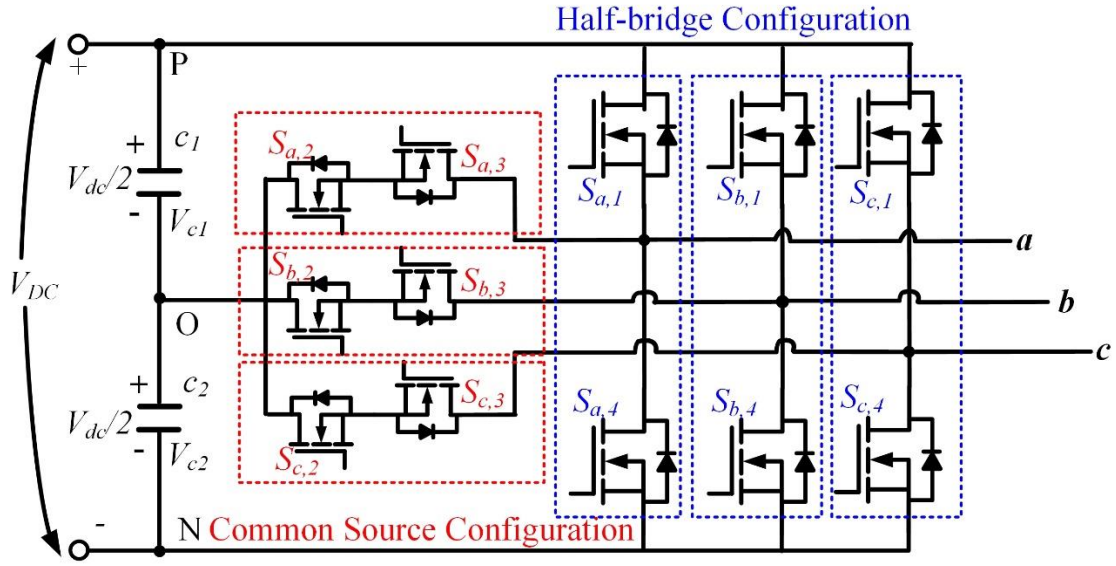

Figure 2.5: Three-level T-type NPC inverter topology.

A T-type NPC is shown in Figure 2.5. In T-type NPC, four semiconductor switches per phase are configures in two different configurations. Two among four are configured as half-bridge configuration and another two are configured as common source configuration. However, the T T-type NPC does not have any clamping diode, therefore, T-type NPC has less conduction loss. Both 3-L NPC and T-type NPC topologies share the same circuit dynamics, although their structures are different. Therefore, rest of the section in this chapter focuses on 3-L converter modeling taking T-type NPC as an example.

A typical 3-L T-type NPC topology is already presented in Figure 2.5, where each phase consists of four switching positions, i.e., $S_{a,1}$, $S_{a,2}$, $S_{a,3}$ and $S_{a,4}$, using phase *a* as an example. The $S_{a,1}$ and $S_{a,4}$ is in the normal half-bridge (HB) configuration, while the $S_{a,2}$ and $S_{a,3}$ are in the common source (CS) configuration. The output voltage vectors generated by the T-type NPC [63] can be expressed as,

$$V = \frac{2}{3}(v_{ao} + k \cdot v_{bo} + k^2 \cdot v_{co}) \tag{2.8}$$

where, v_{ao}, v_{bo} and v_{co} are the output voltages generated by the inverter and k is $e^{j2\pi/3}$. Assuming constant and balanced DC-link capacitor voltages ($V_{c1} = V_{c2}$), the inverter phase terminal voltage, i.e., line-to-neutral voltage, can be expressed as

$$v_{xo} = s_x \frac{v_{dc}}{2} \tag{2.9}$$

where $x = a, b, c$, and $v_{dc} = v_{c1} + v_{c2}$. The s_x is the switching state of the phase x, i.e., P state, $s_x = 1$, where the inverter output terminal is connected to the positive rail of the DC-link; O state, $s_x = 0$, where the inverter output terminal is connected to the neutral point of the DC-link; and N state, $s_x = -1$, where the inverter output terminal is connected to the negative rail of the DC-link.

Table 2.1
Switching States of a 3-L T-type NPC

Switching State s_x	Phase Voltage v_{xO}	Gate Signals $S_{x,1}$	$S_{x,2}$	$S_{x,3}$	$S_{x,4}$
P	$+V_{dc}/2$	1	1	0	0
O	0	0	1	1	0
N	$-V_{dc}/2$	0	0	1	1

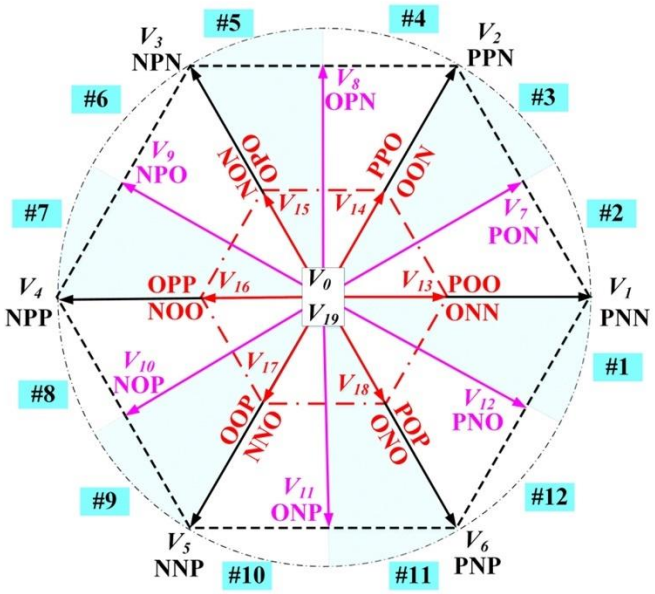

Figure 2.6: The voltage vector diagram for a 3-L T-type inverter.

Fig. 2.6 shows all the space voltage vectors or the real voltage vectors (RVVs, to distinguish from the virtual space vectors defined later) that a 3-L inverter can generate. Although, the T-type NPC and the 3-L NPC have different circuit configuration, however, they share the same voltage vector diagram. Table 2.1 summaries the relationships between the switching states and output terminal voltages for 3-L T-type NPC converter phase leg [64]. The gate signals of $S_{x,1}$ and $S_{x,3}$ is always complementary to each other, so as the $S_{x,2}$ and $S_{x,4}$. Based on Table 2.1, the switching state, formed by s_x of each phase and the extend form of the switching state, formed by $S_{x,1}$ and $S_{x,2}$ of each phase of a RVV, V_i, where i = 0, 1, 2, …, 19, can be expressed as

$$
\begin{aligned}
V_i &= \begin{bmatrix} s_a & s_b & s_c \end{bmatrix} && \text{.....Switching States} \\
&= \begin{bmatrix} s_{a,1} & s_{a,2} & s_{b,1} & s_{b,2} & s_{c,1} & s_{c,2} \end{bmatrix} && \text{.....Extended Form of Switching States}
\end{aligned} \tag{2.10}
$$

For all the RVVs, the elements of the extended form of the switching states are either 0 or 1. Therefore, when one RVV is applied over a control cycle, there are no switching actions. For a 3-L inverter, all of the RVVs can be divided into four categories based on their amplitude [26], i.e., large voltage vectors ($V_1 \sim V_6$), medium voltage vectors ($V_7 \sim V_{12}$), smaller voltage vectors ($V_{13} \sim V_{18}$) and zero voltage vectors (V_0 and V_{19}).

2.5 DC-link Capacitor Selection

The DC-link capacitor helps to keep the DC-link voltage stable which is very crucial for operating an inverter properly. Therefore, it is important to properly calculate the capacitance that is need for a properly functional inverter. However, the DC-link capacitor typically holds a large amount of volume in the full system. Therefore, to increase the power density, it is important to select the capacitor carefully but at the same time optimum operation of the inverter is highly desirable. The minimum allowable DC-link capacitance can be evaluated by [27]

$$
C_{d,min} \geq \frac{\Delta P_{Max} \cdot T_D}{2V_{dc} \cdot \Delta V_{dc}} \tag{2.11}
$$

where, ΔP_{max} is the maximum change in the power or in the other words, maximum power variation of the inverter system, T_d is the number of switching cycles that a controller needs to achieve ΔP_{max} or other words, response time of the voltage control loop which is typically 5-10 times of a switching period, V_{dc} is the DC-link voltage, and ΔV_{dc} is the maximum allowable voltage ripple on the DC-link.

In addition to maintaining the allowable ripple voltage in the system, the DC-link capacitors must be able to provide the required ripple currents of the inverter under any loading condition. The root mean square (RMS) input current to the inverter is given by

$$I_{RMS} = \frac{I_M}{\sqrt{2}} \sqrt{\frac{2\sqrt{3}}{\pi} MI \left(\frac{1}{4} + \cos^2 \varphi \right)} \tag{2.12}$$

where, I_M is the phase current magnitude, MI is the modulation index, and φ is the power factor angle. The dc component of the RMS input current of the inverter is

$$I_{AVG} = \frac{3}{2} I_M MI \cos \varphi \tag{2.13}$$

Now, the capacitor RMS current can be calculated as [65]

$$I_{cap,RMS} = \sqrt{I_{RMS}^2 - I_{AVG}^2} \tag{2.14}$$

2.6 PMSM Control Approaches

PMSM runs at variable speeds with the help of variable frequency drive. In general, PMSM control schemes can be divided into three categories, open loop control or volt-hertz (*V*/*f*) control, field-oriented control (FOC) and direct torque control (DTC). Here, *V*/*f* falls under scaler control, and rest of two which are FOC, and DTC fall under vector control approach for PMSM.

2.6.1 Scaler V/f Control

Induction machine runs in no-synchronous speed due to slip, in contrast PMSM operates at synchronous speed and the speed is directly related to the frequency supplied by the controller. And required voltage level is determined based on *V*/*f* ratio such that the ratio is kept constant. The *V*/*f* control is an open loop control was developed for induction motor but later it was implemented for PMSM as well. For gate signal generation from reference voltages, a voltage modulator is used. Figure 2.7 shows an example of the *V*/*f* control implementation [66].

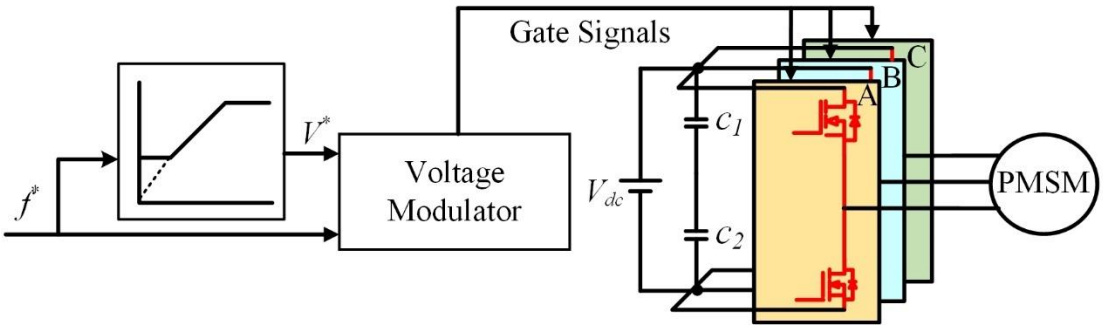

Figure 2.7: Scalar *V/f* control scheme.

There is no feedback path, therefore, it is considered as open loop control approach. The control model is derived from steady-state mathematical model of the PMSM machine and in the control scheme, most of the dynamics are ignored. Hence, the transient behavior is not satisfactory for this kind of motor control. The electromagnetic torque cannot be controlled directly as well. However, it is widely accepted due to its low cost, easily implementable and sensor less motion. Additionally, the steady state performance of the *V/f* control for PMSM is quite acceptable. The *V/f* control has its own field of application, e.g., pumps and fans [67]-[68].

2.6.2 Field Oriented Control (FOC)

The field oriented control (FOC) is a well-established vector control approach for electric AC machines. FOC was first introduced in 1972 by Blaschke [69]. It is also known as advanced control approach since it can achieve both amplitude and phase control of the output AC. With the help of park and inverse park transformation techniques, the current components that are corresponding to the magnetizing flux and torque in AC machines can be decoupled orthogonally so that the magnetizing flux can be controlled individually without affecting dynamic response of the torque and vice versa [70]. In the FOC, flux and torque are not directly proportional to the d- or q- axis current. Therefore, the FOC is also known as indirect torque control. With the adaptation of speed sensor, the FOC motor drive can achieve precise speed control with good torque dynamic

performance. Although the FOC has several advantages over scaler control, however, the FOC is complicated to implement and additional sensor, e.g., position/speed sensor is required. A conventional FOC control schematic is shown in Figure 2.8 with closed look approach.

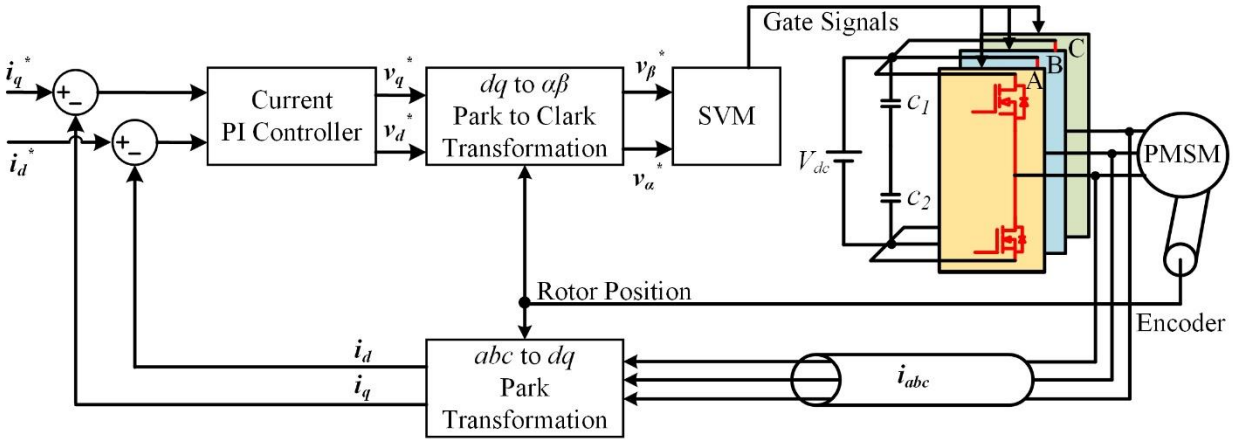

Figure 2.8: Field oriented control (FOC) block diagram.

2.6.3 Direct Torque Control (DTC)

As a promising alternative to the widely used field oriented control (FOC), the direct torque control (DTC) directly controls [5, 6, 71] electromagnetic torque and stator flux linkage without using current control loop, therefore, possessing the merits of fast dynamic response, simple implementation, and high robustness against internal and external disturbances. The DTC approach was firstly proposed by Takahashi and Noguchi in 1986 [5] for induction motors (IM), targeting low power applications. DTC strategy is very different from the FOC, for instance, it does not need current regulators and the complicated coordinate transformation, e.g., park, clark, etc., such that the position sensors can be eliminate [72]-[73]. Although the DTC was first proposed for the induction machines (IM), unlike induction motors, PMSM doesn't have any slip, hence the same DTC architecture for cannot be applied to DTC for PMSM [74]. The angle between the stator flux and the rotor flux linkage also known as the load angle is closely related to the electromagnetic

torque. Therefore, the torque of the PMSM can be easily controlled by controlling the torque angle. The control block diagram for DTC is shown in Figure 2.9.

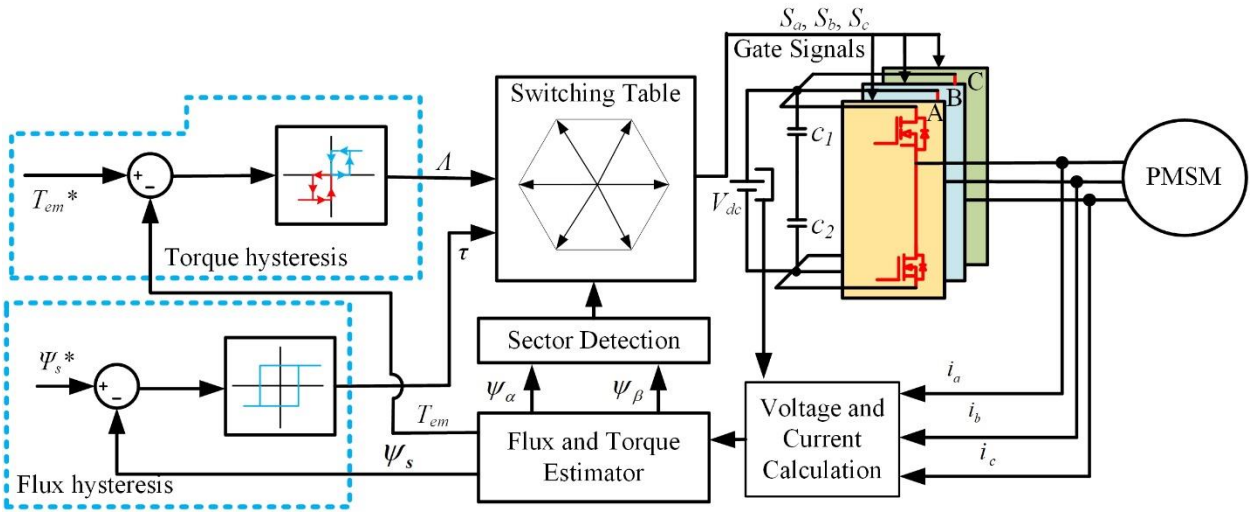

Figure 2.9: Direct torque control algorithm.

It is a noticeable advantage of DTC that all the control tasks are performed in the stationary reference frame, therefore, it is inherently sensor less. Hence, DTC is an attractive solution for many industrial applications. However, it suffers from several major disadvantages such as torque and flux ripples which results higher ripples in the stator currents. Also it has bad performances in low speed operations [75]. In this dissertation, the DTC algorithm was selected as a core research topic and designed an advanced DTC with multi-objective optimization approach.

2.7 Conclusions

This chapter includes the mathematical modeling to the PMSM and the circuit configuration the 2-L and 3-L converters. Brief comparison between the 2-L and 3-L topologies are also discussed. The 3-L converter details are presented elaborately since this topology is adopted in this research mostly. The switching states and voltage vector diagram are also shown in this chapter for the 3-L converter. Then the control algorithms for PMSM are presented and brief comparison

between them are mentioned. In this dissertation, advanced DTC is proposed to overcome the inherent disadvantages of the conventional DTC, e.g., torque ripples, current ripples.

CHAPTER 3

DTC APPROACHE FOR PMSM

3.1 Introduction

The basic operation principle of the DTC is to apply appropriate voltage vector directly to the motor through the inverter based on the electromagnetic torque errors and stator flux linkage. In DTC approach the hysteresis controllers are used to regulate the stator flux linkage and electromagnetic torque with the non-zero voltage vectors [74].

This chapter discusses a details analysis and review of the conventional DTC schemes for PMSM. First, the working principle of the conventional DTC is provided Then the stability criteria, ripple analysis are presented, respectively. Finally, a conclusion is drawn based on the analysis done in this chapter.

3.2 Conventional DTC Approach

Three most popular control algorithms for AC machines are described in the previous chapter in section 2.6. The scalar and FOC schemes are the control schemes where the PWM modulator is necessary for connecting the controller to the hardware. In this method, the AC reference signals are generated by the control algorithms and then PWM signals are generated to operate the inverter. In contrast, the voltage vectors, which are basically the switching states of the inverter are calculated based on the machine's status, without the help of the current regulator or PWM modulator. Hench, the conventional DTC technique is noticeable from general PWM technique and easy to implement. The Figure 3.1 presents a conventional DTC algorithm in block diagram for PMSM. A conventional DTC scheme has three major parts [76], a) electromagnetic torque and stator flux linkage estimation, b) hysteresis comparators, and c) a switching table. The

electromagnetic torque and stator flux are used directly to measure the error between the torque command and flux command, respectively. Depending on the flux tracking error, the stator flux hysteresis controller selects active voltage vectors to restricts the flux trajectory within the pre-determined hysteresis band. Additionally, the torque hysteresis controller selects both active and null vectors based on torque tracking error to ensure the output torque tracks its command. In each control cycle, the voltage vector, which is defined by S_a, S_b and S_c, is selected using the switching table in the DTC.

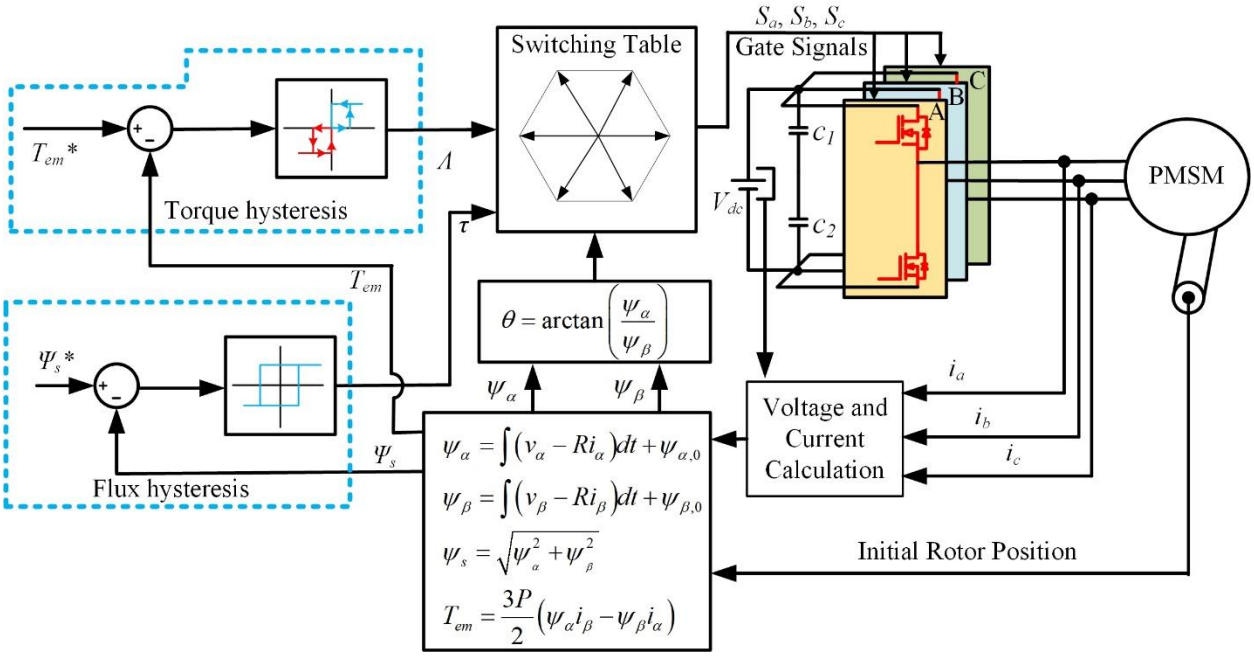

Figure 3.1: Direct torque control algorithm block diagram with flux and torque estimator.

The power converter that is used for the conventional DTC is the 2-L three-phase converter. These power converter or inverters can output a total number of eight voltage space vectors. Among eight, two are zero voltage vector when the output of the inverter is zero and rest of the voltage vectors are active vectors. The voltage vector space diagram shown in Figure 3.2 is in $\alpha\beta$ stationary reference frame and divided into six sectors and each sector is 60 degrees. The

magnitude of the stator flux, i.e., $|\psi_s|$, the corresponding sector number can be calculated from properly designed flux estimator in $\alpha\beta$ stationary reference frame. Then according to the sector number calculated and the output of the hysteresis comparator, a proper voltage vector is selected from the switching table. Since, the voltage vector selection is based on the torque and flux hysteresis band the dynamic performance of the DTC is better than the FOC. The voltage space vector diagram for a three phase 2-L inverter is shown in Figure 3.2. As an example of the voltage vector selection, from the Figure 3.2, assuming the rotor of the motor is rotating counterclockwise, and the stator flux vector, ψ_s lies in the sector 1. Then, to maintain a circular or hexagon movement of stator flux, four voltage space vectors are available, named V_2(110), V_3(010), V_5(001) and V_6(101). The increasing/decreasing of torque and stator flux can be obtained by selecting the proper voltage vector, i.e., 1) if V_2(110) is applied, both $|\psi_s|$ and torque are increased; 2) if V_3(010) is applied, the $|\psi_s|$ is decreased, while torque is increased; 3) if V_5(001) is applied, both the $|\psi_s|$ and torque are decreased; and 4) if V_6(101) is applied, the $|\psi_s|$ is increased, while torque is decreased.

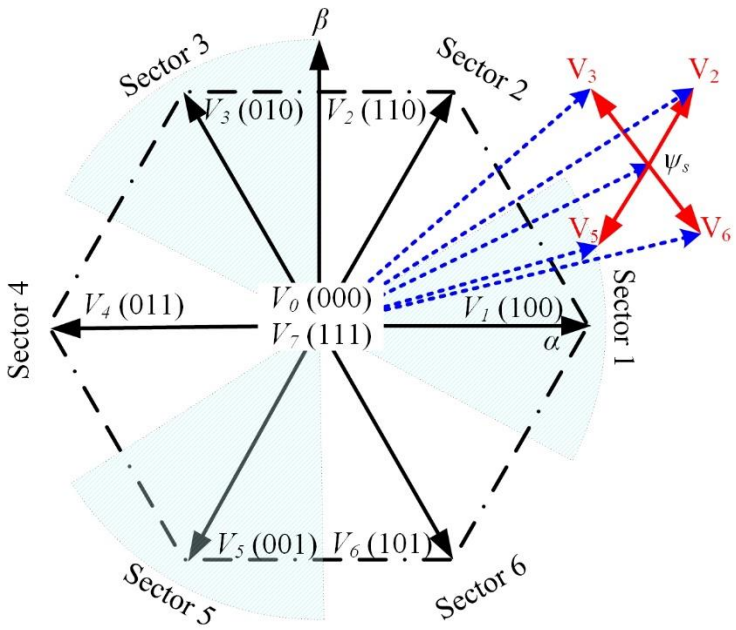

Figure 3.2: Direct torque control algorithm block diagram with flux and torque estimator.

Table 3.1
Switching Table for Conventional DTC

		Sector Number					
ψ_s	T_{em}	1	2	3	4	5	6
+1	+1	V_2	V_3	V_4	V_5	V_6	V_1
	–1	V_6	V_1	V_2	V_3	V_4	V_5
-1	+1	V_3	V_4	V_5	V_6	V_1	V_2
	–1	V_5	V_6	V_1	V_2	V_3	V_4

According to the previous discussion, the switching table can be generated based on the torque and flux hysteresis controller and the sector number which is shown in Table 3.1 [71]. The switching table is constructed in such a way that the torque tracks the command quickly and accurately and the stator flux is controlled circularly.

3.3 Stability of the DTC

In general, it is assumed that the electromagnetic torque and the load angle, δ of the PMSM is positively correlated. However, this assumption needs to be verified to implement the DTC on PMSM [77]. In other words, $\frac{dT_{em}}{d\delta} > 0$ criteria should be satisfied to ensure the stability of the DTC for PMSM [74] and [78]. The torque equation can be rewritten as,

$$T_{em} = \frac{3}{2} P \frac{\psi_m |\psi_s|}{L_d} \sin\delta + \frac{3}{4} P \left(\frac{1}{L_q} - \frac{1}{L_d} \right) |\psi_s|^2 \sin(2\delta) \tag{3.1}$$

Equation (3.1) indicates that the electromagnetic torque is a function of load angle. To ensure the increase and decrease of the torque T_{em} by increasing and decreasing δ respectively, in the other words to determine the stability criteria, it is important to find monotonic increasing region for (3.1) [79], i.e., $\frac{dT_{em}}{d\delta} > 0$, where $\frac{dT_{em}}{d\delta}$ can be achieved by

$$\frac{dT_{em}}{d\delta} = \frac{3}{2}P\frac{\psi_m|\psi_s|}{L_d}\cos\delta + \frac{3}{2}P\left(\frac{1}{L_q} - \frac{1}{L_d}\right)|\psi_s|^2\cos(2\delta) \tag{3.2}$$

To ensure $\frac{dT_{em}}{d\delta} > 0$, following condition needs to be satisfied,

$$\cos(\delta) < \frac{\psi_m + \sqrt{\psi_m^2 + 8\chi^2\psi_s^2}}{4\chi\psi_s} \tag{3.3}$$

where $\chi = \frac{L_q - L_d}{L_d}$. For this dissertation salient pole IPM motor is considered, and the machine parameters are presented in Appendix A-1. For a salient pole IPM motor, since $L_q > L_d$, χ is always positive and (3.3) can be further written as,

$$-\frac{\pi}{2} < \delta < -\cos^{-1}\left(\frac{\psi_m + \sqrt{\psi_m^2 + 8\chi^2\psi_s^2}}{4\chi\psi_s}\right) \quad \text{and} \quad \cos^{-1}\left(\frac{\psi_m + \sqrt{\psi_m^2 + 8\chi^2\psi_s^2}}{4\chi\psi_s}\right) < \delta < \frac{\pi}{2} \tag{3.4}$$

Since the monotonic increasing region is expected to cover the whole range of load angle from $-\frac{\pi}{2}$ to $\frac{\pi}{2}$ [79], so

$$\frac{\psi_m + \sqrt{\psi_m^2 + 8\chi^2\psi_s^2}}{4\chi\psi_s} > 1 \tag{3.5}$$

which further leads to

$$\psi_s < \frac{\psi_m}{\chi} = \frac{L_d}{L_q - L_d}\psi_m \tag{3.6}$$

which is the boundary condition that must be considered when designing the DTC. This boundary condition is the stability criteria for the DTC on PMSM which must be satisfied to operate the motor without failing. It is possible to represent the relationship between the electromagnetic torque and the stator flux graphically using the machine parameters and the torque equation of the PMSM in Figure3.3.

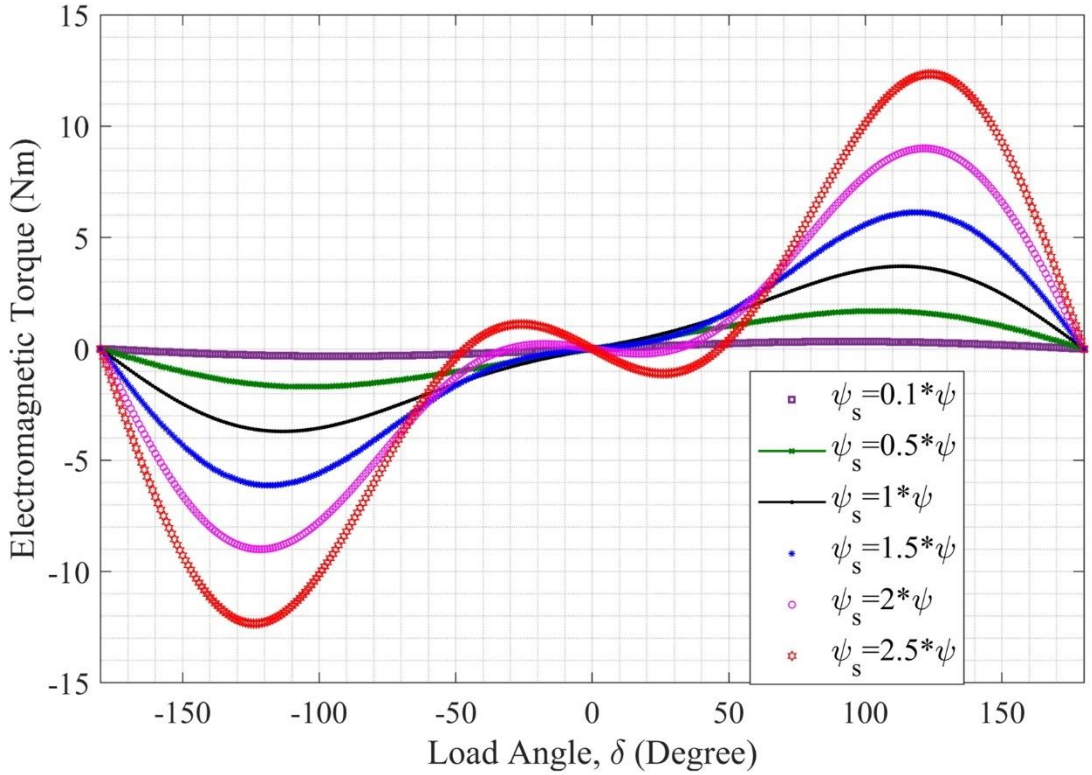

Figure 3.3: The relationship between the electromagnetic torque, T_{em} and the load angle, δ of the PMSM.

3.4 Ripple Analysis of the DTC Approach

The conventional DTC suffers from electromagnetic torque and stator flux ripples. In this section, the torque and flux ripples for PMSM drive are analyzed mathematically in terms of flux space vector and load angle. The torque and flux ripples are analyzed in discrete form in this section.

Form the Figure 3.4, $\psi_s[k]$ is the stator flux magnitude at the k^{th} step in α-β stationary reference frame. $\theta_\omega = \omega_e[k]T_s$, where $\omega_e[k]$ is the rotor speed at k^{th} time. γ is the angle between α reference frame and the applied voltage vector. Now, $\psi_s[k+1]$ can be defined as,

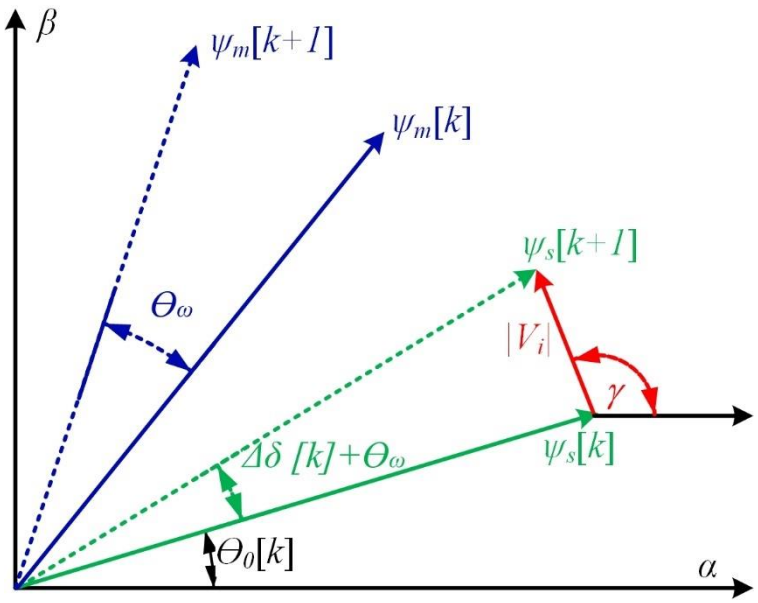

Figure 3.4: Voltage vector effects on the torque and stator flux variations.

$$\begin{bmatrix} |\psi_s[k+1]|_\alpha \\ |\psi_s[k+1]|_\beta \end{bmatrix} = \begin{bmatrix} |\psi_s[k]|_\alpha \\ |\psi_s[k]|_\beta \end{bmatrix} + \begin{bmatrix} |V_i|_\alpha \\ |V_i|_\beta \end{bmatrix} T_s \tag{3.7}$$

where, $V_{i\alpha}$, $V_{i\beta}$ are the applied voltage vector in $\alpha\beta$ stationary reference frame and T_s is the sampling time. From (3.7),

$$\begin{aligned} &|\psi_s[k+1]|_\alpha = |\psi_s[k]|\cos\theta_0[k] + T_s|V_i|\cos\gamma \\ &\Rightarrow |\psi_s[k+1]|_\alpha^2 = |\psi_s[k]|^2\cos^2\theta_0[k] + 2|\psi_s[k]|T_s|V_i|\cos\theta_0[k]\cos\gamma + T_s^2|V_i|^2\cos^2\gamma \end{aligned} \tag{3.8}$$

$$\begin{aligned} &|\psi_s[k+1]|_\beta = |\psi_s[k]|\sin\theta_0[k] + T_s|V_i|\sin\gamma \\ &\Rightarrow |\psi_s[k+1]|_\beta^2 = |\psi_s[k]|^2\sin^2\theta_0[k] + 2|\psi_s[k]|T_s|V_i|\sin\theta_0[k]\sin\gamma + T_s^2|V_i|^2\sin^2\gamma \end{aligned} \tag{3.9}$$

Adding (3.7) and (3.8),

$$\left|\psi_s[k+1]\right|^2 = \left|\psi_s[k]\right|^2 + 2\left|\psi_s[k]\right|T_s\left|V_i\right|\left[\cos\theta_0[k]\cos\gamma + \sin\theta_0[k]\sin\gamma\right] + T_s^2\left|V_i\right|^2$$

$$\Rightarrow \left|\psi_s[k+1]\right| - \left|\psi_s[k]\right| = \frac{2\left|\psi_s[k]\right|T_s\left|V_i\right|\cos\left(\theta_0[k]-\gamma\right) + T_s^2\left|V_i\right|^2}{\left|\psi_s[k+1]\right| + \left|\psi_s[k]\right|} \tag{3.9}$$

$$\Rightarrow \left|\psi_s[k+1]\right| - \left|\psi_s[k]\right| = \frac{2T_s\left|V_i\right|\left[\left|\psi_s[k]\right|\cos\left(\theta_0[k]-\gamma\right) + T_s\left|V_i\right|\right]}{\left|\psi_s[k+1]\right| + \left|\psi_s[k]\right|}$$

Flux change can be represented as,

$$\left|\psi_s[k+1]\right| - \left|\psi_s[k]\right| = \Delta\left|\psi_s[k]\right| \tag{3.10}$$

Therefore,

$$\Delta\left|\psi_s[k]\right| = \frac{2T_s\left|V_i\right|\left[\left|\psi_s[k]\right|\cos\left(\theta_0[k]-\gamma\right) + T_s\left|V_i\right|\right]}{\left|\psi_s[k+1]\right| + \left|\psi_s[k]\right|} \tag{3.11}$$

From (3.11), it is visible that $\Delta\left|\psi_s[k]\right|$ is a function of load angle and applied voltage vectors. In order to achieve the tracking from the flux to its reference, the change of the flux should have opposite sign with the flux tracking error. The $\Delta\left|\psi_s[k]\right|$ cab be expressed as,

$$\Delta\left|\psi_s[k]\right| = g\left(\gamma, V_i\right) \tag{3.12}$$

Now, the active flux can be written as,

$$\left|\psi_d^a\right| = \psi_m + \left(L_d - L_q\right)i_d \tag{3.13}$$

Torque equation is presented in chapter 2 Equation (2.5). Substitute (3.13) into (2.5),

$$T_{em} = \frac{3}{2}\frac{P}{L_d}\left|\psi_s\right|\left|\psi_d^a\right|\sin\delta \tag{3.14}$$

Taking derivative of (3.14) with respect to time,

$$\frac{dT_{em}}{dt}=\frac{3}{2}\frac{P}{L_d}\left|\psi_d^a\right|\sin\delta\times\frac{d\left|\psi_s\right|}{dt}+\frac{3}{2}\frac{P}{L_d}\left|\psi_s\right|\sin\delta\times\frac{d\left|\psi_d^a\right|}{dt}+\frac{3}{2}\frac{P}{L_d}\left|\psi_s\right|\left|\psi_d^a\right|\cos\delta\times\frac{d\delta}{dt} \tag{3.15}$$

At k^{th} step, (3.15) can be represented in discrete time as,

$$\begin{aligned}\Delta T_{em}[k]=&\frac{3}{2}\frac{P}{L_d}\left|\psi_d^a[k]\right|\sin\delta[k]\times\Delta\left|\psi_s[k]\right|+\frac{3}{2}\frac{P}{L_d}\left|\psi_s[k]\right|\sin\delta[k]\times\Delta\left|\psi_d^a[k]\right|\\&+\frac{3}{2}\frac{P}{L_d}\left|\psi_s[k]\right|\left|\psi_d^a[k]\right|\cos\delta[k]\times\Delta\delta[k]\end{aligned} \tag{3.16}$$

From Equation (3.16) it is clear that the stator flux magnitude and the loading condition affect the flux weights and the load angle directly impact the electromagnetic torque ripples. Now, the rate of change of torque can be defined as,

$$T_{em}[k+1]-T_{em}[k]=\Delta T_{em}[k] \tag{3.17}$$

The torque $T_{em}[k]$ has the form of,

$$T_{em}[k]=\frac{3}{2}\frac{P}{L_q}\left|\psi_s[k]\right|\left|\psi_d^a[k]\right|\sin\delta[k] \tag{3.18}$$

Dividing (3.16) by (3.18),

$$\frac{\Delta T_{em}[k]}{T_{em}[k]}=\frac{\Delta\left|\psi_s[k]\right|}{\left|\psi_s[k]\right|}+\frac{\Delta\left|\psi_d^a[k]\right|}{\left|\psi_d^a[k]\right|}+\frac{\Delta\delta[k]}{\tan\delta[k]} \tag{3.19}$$

Substitute (3.10) and (3.17) into (3.19), the load angle increment in discrete form can be written as,

$$\Delta\delta[k]=\tan\delta[k]\times\left(\frac{T_{em}[k+1]}{T_{em}[k]}-\frac{\left|\psi_s[k+1]\right|}{\left|\psi_s[k]\right|}-\frac{\left|\psi_d^a[k+1]\right|}{\left|\psi_d^a[k]\right|}\right) \tag{3.20}$$

where, $\Delta\left|\psi_d^a[k]\right|$ is calculated as. In (3.16), $\Delta\left|\psi_s[k]\right|$ can be calculated from (3.11). As $\Delta\left|\psi_s[k]\right|$ is a function of $\delta[k]$ and V_i, therefore, $\Delta T_{em}[k]$ can be expressed as,

$$\Delta T_{em}[k] = f\left(\delta[k], |V_i|\right) \tag{3.21}$$

It is clear from the above analysis that the torque and stator flux linkage changes are approximately proportional to the sampling time, T_s. In the conventional DTC each voltage vector is applied for the entire switching cycle, which is the main reason behind the torque and flux ripples. In summary if the switching frequency is lower than the sampling time is larger. This is why it is recommended to use higher switching frequency to reduce torque and flux ripples in DTC based PMSM.

3.5 Conclusions

This chapter discusses the conventional direct torque control technique for the PMSM and stability criteria for the DTC. A boundary condition is formulated for the PMSM motor running using DTC approach to operate properly. The relationship between the electromagnetic torque, T_{em} and the load angle, δ of the PMSM is also presented in this section. Then the electromagnetic torque and stator flux ripples are analyzed in discrete form. The torque ripples and the flux ripples are proportional switching periods. Therefore, the DTC with lower switching period has higher ripples. Therefore, in this dissertation, advanced DTC is proposed to reduce the ripples in the conventional DTC.

CHAPTER 4

ADVANCED DIRECT TORQUE CONTROL FOR THREE-LEVEL T-TYPE NPC CONVERTER WITH INTRINSIC DC-LINK VOLTAGE BALANCING

4.1 Introduction

In this section, an enhanced novel DTC, using a redefined voltage space vector diagram, is proposed. An all SiC 3-L T-type NPC converter is adopted to validate the effectiveness of the proposed advanced DTC method for an interior permanent magnet (IPM) synchronous motor. Due to the oscillations of the neutral-point (NP) voltage, the DC-link voltage balancing is a primary challenge for the 3-L inverters. The voltage space vectors used in the proposed DTC only include the real space vectors and virtual space vectors (VSV) that do not affect the NP voltage, such that an inherent DC-link voltage balancing can be achieved without using additional DC-link voltage/current sensors or active feedback controls. In addition, the use of the additional VSVs and a multi-level hysteresis torque control in the proposed DTC algorithm can effectively reduce the torque and flux ripples while enhancing the dynamic response which is the major advantage of the DTC. Comprehensive simulations and experiments are conducted and presented later to validate the effectiveness of the proposed control scheme.

4.2 Conventional and Proposed Direct Torque Control for Three-Level T-Type Converter

In this section, the conventional and proposed DTC for 3-L T-type inverter is presented. Also, the effect of the real voltage vectors (RVVs) on the neutral point current and the torque and current ripples are analyzed. To address the challenges in the conventional DTC for 3-L inverter an enhanced DTC with the virtual voltage vectors is proposed and the performances are validated with novel voltage vector diagram.

4.2.1 Conventional Direct Torque Control Algorithm for 3-L Inverter

An all SiC 3-L T-type topology is presented in Figure 4.1, which is used for the DTC implementation. The S_{a1} and S_{a4} are in the normal SiC half-bridge (HB) configuration, while the S_{a2} and S_{a3} are in the SiC common source (CS) configuration.

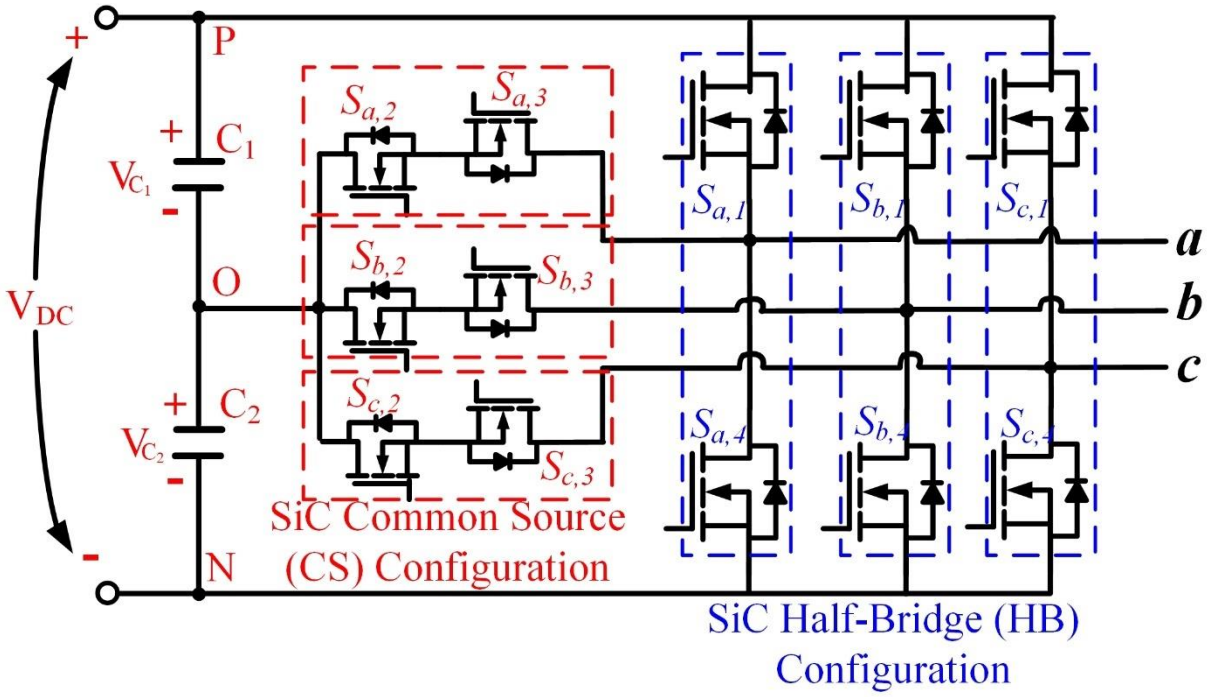

Figure 4.1: Schematic of an all SiC T-type inverter.

The voltage space vector diagram is presented in Figure 2.6. Also, the output voltage generated from 3-L inverter is shown in chapter 3 in detail. The control block diagram for conventional DTC with 3-L T-type inverter-fed IPMSM is shown in the Figure 4.2 where the 4-level torque hysteresis controller and 2-level flux hysteresis controller is shown. In conventional DTC for 3-L inverter, the DC-link capacitor voltages or the neutral point current is measured, and this information is used to validate the voltage vector selection, therefore, the DC-link capacitor voltages are balanced. According to (2.3) and (2.4), torque and flux observers can be properly designed. In

every control iteration in DTC, the estimated torque and flux are compared with the reference torque and flux. The errors between the estimations and their references are fed to the torque and flux hysteresis loop to select the appropriate voltage vector from the switching table. Table 4.1 is the switching table of a conventional DTC for 3-L converter [34]. The 4-level (±2, ±1) torque hysteresis [80] and two-level (±1) flux hysteresis controllers, as shown in Figure 4.2 and Figure 4.3, respectively, are used for the conventional DTC for the 3-L inverter.

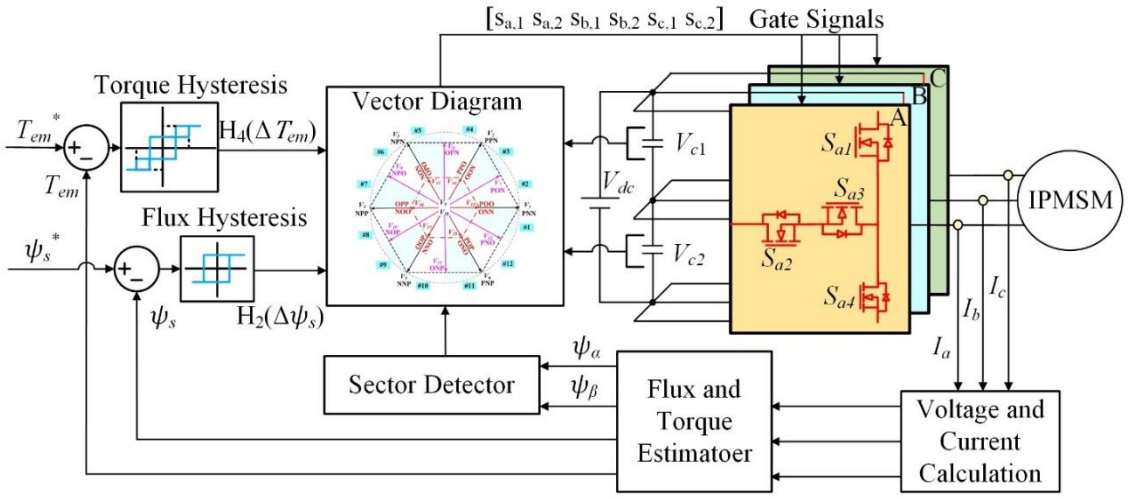

Figure 4.2: A block diagram of the conventional DTC for 3-L T-type inverter.

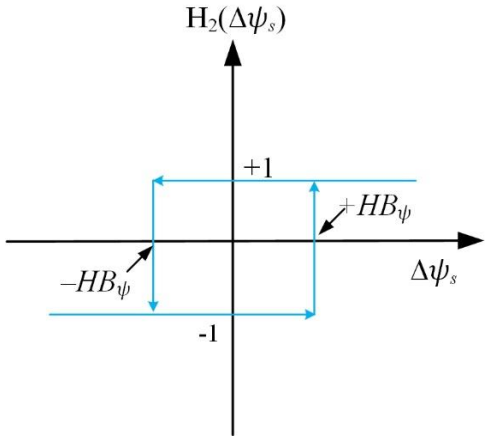

Figure 4.3: Flux hysteresis comparator.

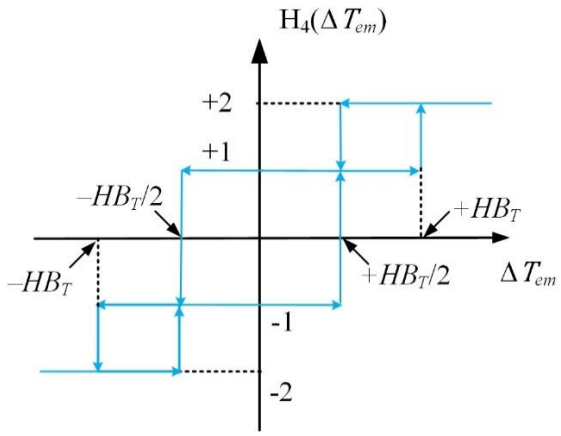

Figure 4.4: Conventional four level torque hysteresis comparator.

Table 4.1
The Switching Table of the Conventional DTC for 3-L Inverter

$H_2(\Delta\psi_s)$	$H_4(\Delta T_{em})$	Sector Numbers											
		1	2	3	4	5	6	7	8	9	10	11	12
+1	+2	V_2	V_8	V_3	V_9	V_4	V_{10}	V_5	V_{11}	V_6	V_{12}	V_1	V_7
	+1	V_{14}	V_{14}	V_{15}	V_{15}	V_{16}	V_{16}	V_{17}	V_{17}	V_{18}	V_{18}	V_{13}	V_{13}
	–1	V_{18}	V_{18}	V_{13}	V_{13}	V_{14}	V_{14}	V_{15}	V_{15}	V_{16}	V_{16}	V_{17}	V_{17}
	–2	V_8	V_6	V_9	V_1	V_{10}	V_2	V_{11}	V_3	V_{12}	V_4	V_7	V_5
–1	+2	V_{11}	V_3	V_{12}	V_4	V_7	V_5	V_8	V_6	V_9	V_1	V_{10}	V_2
	+1	V_{15}	V_{15}	V_{16}	V_{16}	V_{17}	V_{17}	V_{18}	V_{18}	V_{13}	V_{13}	V_{14}	V_{14}
	–1	V_{17}	V_{17}	V_{18}	V_{18}	V_{13}	V_{13}	V_{14}	V_{14}	V_{15}	V_{15}	V_{16}	V_{16}
	–2	V_5	V_{11}	V_6	V_{12}	V_1	V_7	V_2	V_8	V_3	V_9	V_4	V_{10}

As shown in Fig. 4.4, the stator flux is located in sector #1 and reference torque tracking error, i.e., ΔT_{em}, is in the outer hysteresis band, i.e., $H_4(\Delta T_{em}) = +2$ or -2, there are four available voltage vectors since the voltage vector numbers are finite unlike the space vector pulse width modulation technique, i.e., two large vectors V_2 and V_5 and two middle vectors V_8 and V_{11}. The increment and decrement of the torque and stator flux can be ensured by selecting the proper voltage vector, i.e., 1) if V_2 is applied, both $|\psi_s|$ and torque angle, δ, are increased; 2) if V_8 is applied, $|\psi_s|$ is decreased, while δ is increased; 3) if V_5 is applied, both $|\psi_s|$ and δ are decreased; and 4) if V_{11} is applied, $|\psi_s|$ is increased, while δ is decreased. Similarly, if the stator flux is located in sector #1 while the ΔT_{em}

is in the inner hysteresis band, i.e., $H_4(\Delta T_{em})$ = +1 or –1, Fig. 4.5 shows the effect of all 4 available voltage vectors. In Figure 4.4 and Figure 4.5, Ψ_r is denoated as the rotor flux.

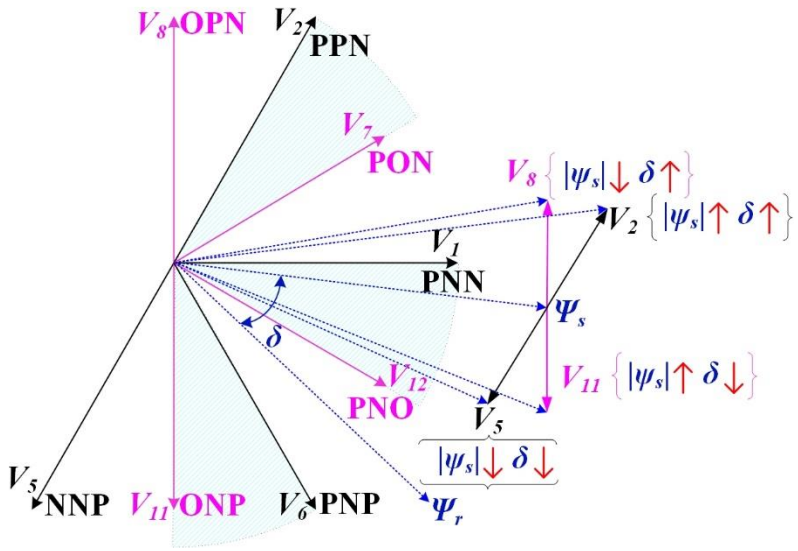

Figure 4.5: The voltage vector selection when ΔT_{em} is in outer hysteresis band.

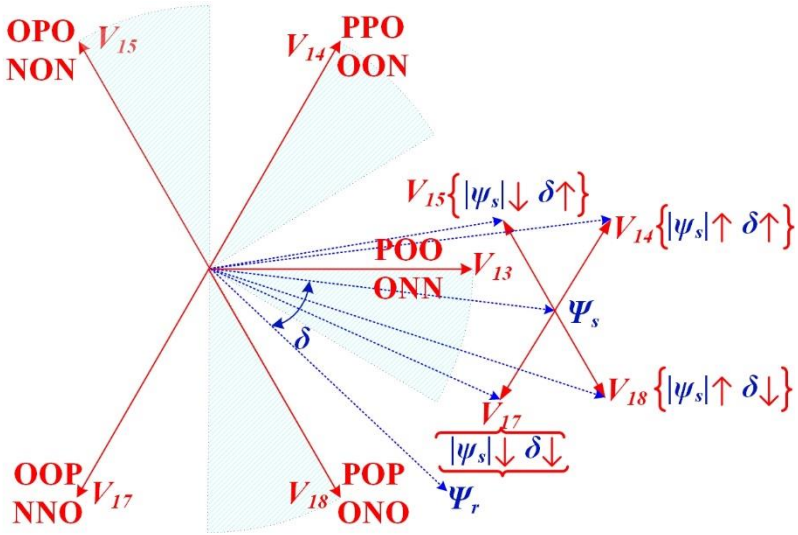

Figure 4.6: The voltage vector selection when ΔT_{em} is in inner hysteresis band.

Neutral point (NP) voltage oscillation is an inherent issue for all 3-L NPC inverters using conventional DTC, which can lead to distorted output voltages and increased voltage stresses on the power devices [80] and [81]. Uneven charging or discharging of the capacitors C_1 and C_2 occur

whenever any of the phase terminals of the 3-L inverter is connected to the NP, i.e., node O in Fig. 1. In the 3-L T-type inverter, both medium and small voltage vectors contribute to the NP current, i_n. In practical applications, the average NP current over a switching cycle can be kept as zero to keep the dc link capacitor voltage balanced. Generally, the small voltage vector can be utilized to minimize the voltage unbalance at the neutral point since each of them has their identical pair voltage vector with opposite neutral point current [33]. For example, from Fig. 4.5. assuming that the estimated flux vector is in sector#1 and small voltage vector V_{14} is selected; then based on the polarity of the neutral point voltage and current, either voltage vector 'PPO' ($i_n = i_c$) or 'OON' ($i_n = -i_c$) can be applied. Thus, the neutral point voltage can be balanced by choosing the voltage vector carefully, based on the measured polarities of the neutral point voltage and current. Therefore, the conventional 3-L converter needs sensor to measure V_{c1}, V_{c2} and i_n, which increases the cost of the overall system.

4.2.1.1 Effect of the Real Voltage Vectors on the Neutral Point Voltages

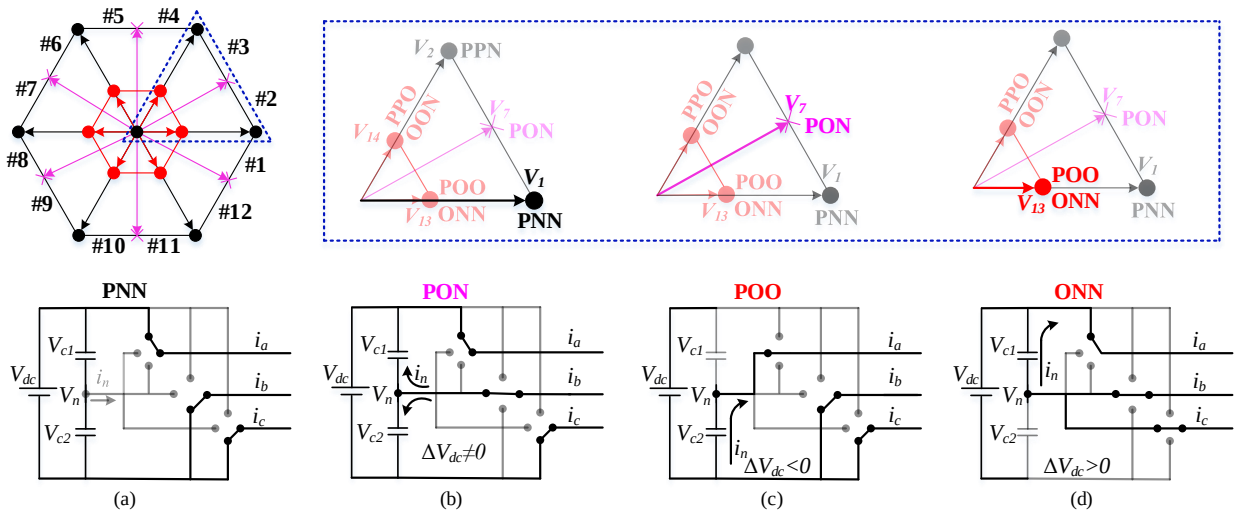

Figure 4.7: Circuit diagram for vectors and their influence on NP voltage.

For a 3-L T-type NPC converter, the DC-link usually consists of two identical capacitors sharing the entire DC-link bus voltage. In the P state, the voltage of the phase terminal with respect to the DC-link neutral point, i.e., V_P, equals to the voltage across the top capacitor. During N state, the voltage of the phase terminal with respect to the DC-link neutral point, i.e., V_N, equals to the voltage across the bottom capacitor, but with an opposite sign. For a 3-L converter, the $|V_P|$ and $|V_N|$ should be identical if the voltages across the two DC-link capacitors are the same, i.e., the top and bottom capacitors sharing the dc bus voltage equally. Otherwise, the output voltage waveform will be distorted with increased harmonic components and increased voltage stresses on the power devices [80] and [82]. Therefore, the DC-link voltage balancing is necessary to reduce the harmonic and maintain the essential function of the converter.

There are four types of voltage vectors for a T-type NPC converter, with each of them has different influence on the NP voltage, i.e., the voltage of the NP with respect to the ground. To analyze the influence of different vectors, as shown in Figure 4.6, Sectors 2 and 3 are used as an example for illustration. In Figure 4.7, the equivalent circuits for the large vector V_1 (PNN), medium vector V_7 (PON) and small voltage vector V_{13} (POO and ONN) are presented [36]. When V_1 is applied, as shown in Figure 4.7 (a), both top and bottom capacitors are connected in the circuit, while the NP is not connected to the load. Therefore, the two capacitors are either charged or discharged by the same current with opposite polarity. Consequently, V_1 does not lead to DC-link voltage unbalancing. When V_7 is applied, as shown in Figure 4.7 (b), both the top and bottom capacitors are connected in the circuit as well. However, the NP is also connected to the load, which leads to a non-zero NP current. Therefore, the currents flow through the two DC-link capacitors are different, which can cause DC-link voltage unbalancing. The two possible switching states for the small vector V_{13} is shown in Figure 4.7 (c) and (d). These two switching states, i.e.,

POO and ONN, connect different DC-link capacitors to the load through the NP. When $i_a > 0$, switching state ONN reduces V_{c2} and leads to a positive ΔV_{dc}, i.e., $\Delta V_{dc} = V_{c2} - V_{c1}$, while POO reduces V_{c1} and leads to a negative ΔV_{dc}. When $i_a < 0$, the result is the opposite. As a conclusion, the medium voltage vectors affect the NP voltage; the two switching states of a small vector have opposite influence on the NP voltage. If the voltage vectors are not selected carefully, the DC-link voltage unbalance can occur and as a result this unbalanced DC-link will affect the torque and current ripples.

4.2.1.2 Effect of Unbalanced DC Link on Torque Ripple and Stator Current Ripple

In a conventional DTC for 3-L converter, in general only one voltage space vector is applied throughout an entire sampling period. According to previous discussion, if one of the small or medium voltage vectors is applied, the unbalanced DC-link voltage will occur, which can lead to increased ripples in the stator currents. The stator current ripples can cause the torque ripples which a major issue of the DTC as well [83]. Due to the complexity to derive an explicit model of toque ripple due to dc link unbalance in a multilevel DTC drive for an IPM motor, in this work, a numerical analysis was guided to visualize the relationship between the torque ripples and stator current ripples due to the DC-link capacitor voltages unbalancing. The key parameters of the IPM motor are presented in in appendix as Table A-1.

Figure 4.8 represents that effect of the ΔV_{dc} on the torque ripple. In the figure the torque ripple and ΔV_{dc} are shown in percentage (%). The study has been conducted in different loading conditions such as full load torque, 50% and 25% of the full torque. It is clear from the Figure 4.8 that when the DC-link capacitor voltages are unequal the torque ripple would be higher. It is also worth to mention that the torque ripple reduces at higher speed. Figure 4.9 shows the effect of ΔV_{dc}

on the stator current THD. It is possible to conclude from the figure that when the DC-link capacitor voltages are not balanced evenly or if there is any presence of bias/offset between two DC-link capacitor voltages, the stator current THD would be higher.

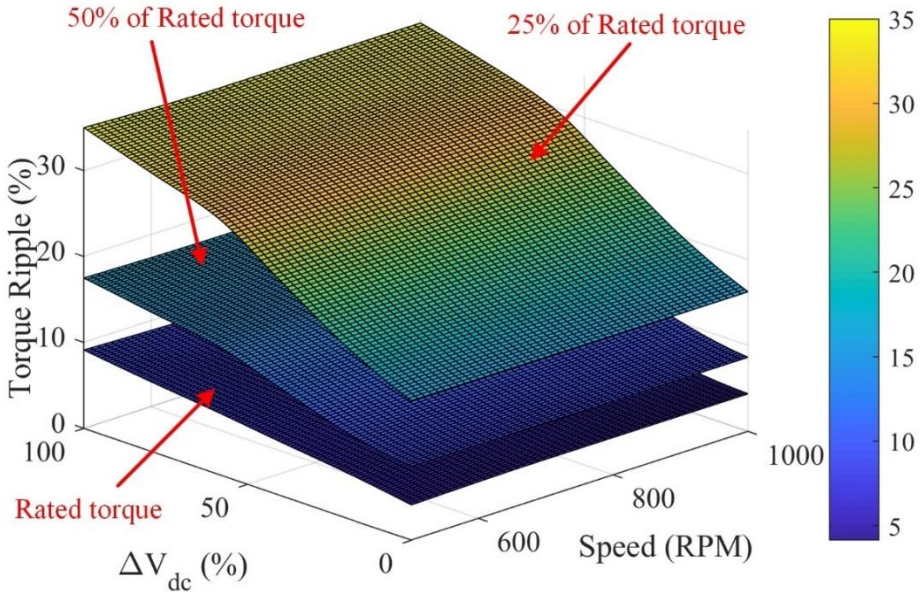

Figure 4.8: Relationship among torque ripple (%), ΔV_{dc} and speed (RPM).

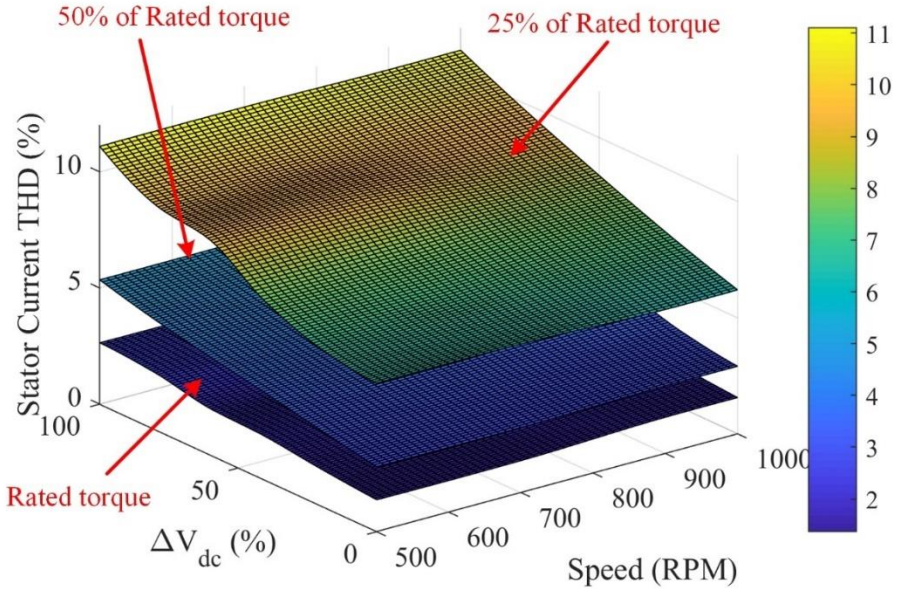

Figure 4.9: Relationship among stator current THD (%), ΔV_{dc}, and speed (RPM).

4.2.2 Proposed Direct Torque Control for 3-L Inverter

The DC-link unbalancing issue in the conventional DTC for a 3-L converter can be mitigated by sensing the two capacitors' voltages and/or the NP current to determine the proper voltage vector, which however can increase the system cost and the controller complexity. Now, for a 3-L NPC converter, NP current, i_n is the main reason behind the DC-link balancing or unbalancing. Ideally, the average neutral point current, i_n, should be kept zero within a switching cycle, T_s to keep the capacitor voltages balanced [81]. In order to achieve the zero average neutral point current, the virtual voltage space vectors concept can be adopted, which is first introduced in [84]. In this dissertation, the VSV concept is integrated with the DTC scheme, and VSVs are generated by using the combinations of real voltage vectors (RVVs). The objective of proposed DTC is to achieve an inherent DC-link voltage balancing without using the additional dc link voltage and current sensors. In the proposed DTC method for IPM motor, only the voltage vectors, including original large voltage vector and the VSVs, that do not affect the NP voltage are used. In addition, due to the use of additional VSVs in the DTC, the ripples in the stator current and torque can be reduced significantly.

4.2.2.1 Proposed Space Vectors Generation and Space Vector Diagram

Effect of the real voltage vectors on the neutral point voltages are discussed in Section 4.2.1.1. According to the analysis, among all the RVVs, the large voltage vectors (V_1 ~ V_6) do not affect the NP voltage in other words no neutral point current flows, while both medium vectors (V_7 ~ V_{12}) and small vectors (V_{13} ~ V_{18}) can lead to the oscillation of the NP voltage. This conclusion is illustrated in Figure 4.10 (a), where it is also seen two regular hexagons formed by different voltage vectors, i.e., (1) large voltage vectors (V_1 ~ V_6) form the outer hexagon and the medium vectors

(V_7 ~ V_{12}) and (2) small vectors (V_{13} ~ V_{18}) form the inner hexagon. In Figure 4.10, the voltage vectors end with red dots are the RVVs which is also the large voltage vectors that do not affect the NP voltage and NP current, while the voltage vectors end with yellow stars are the RVVs which are medium and small voltage vectors, affecting the NP voltage and NP current.

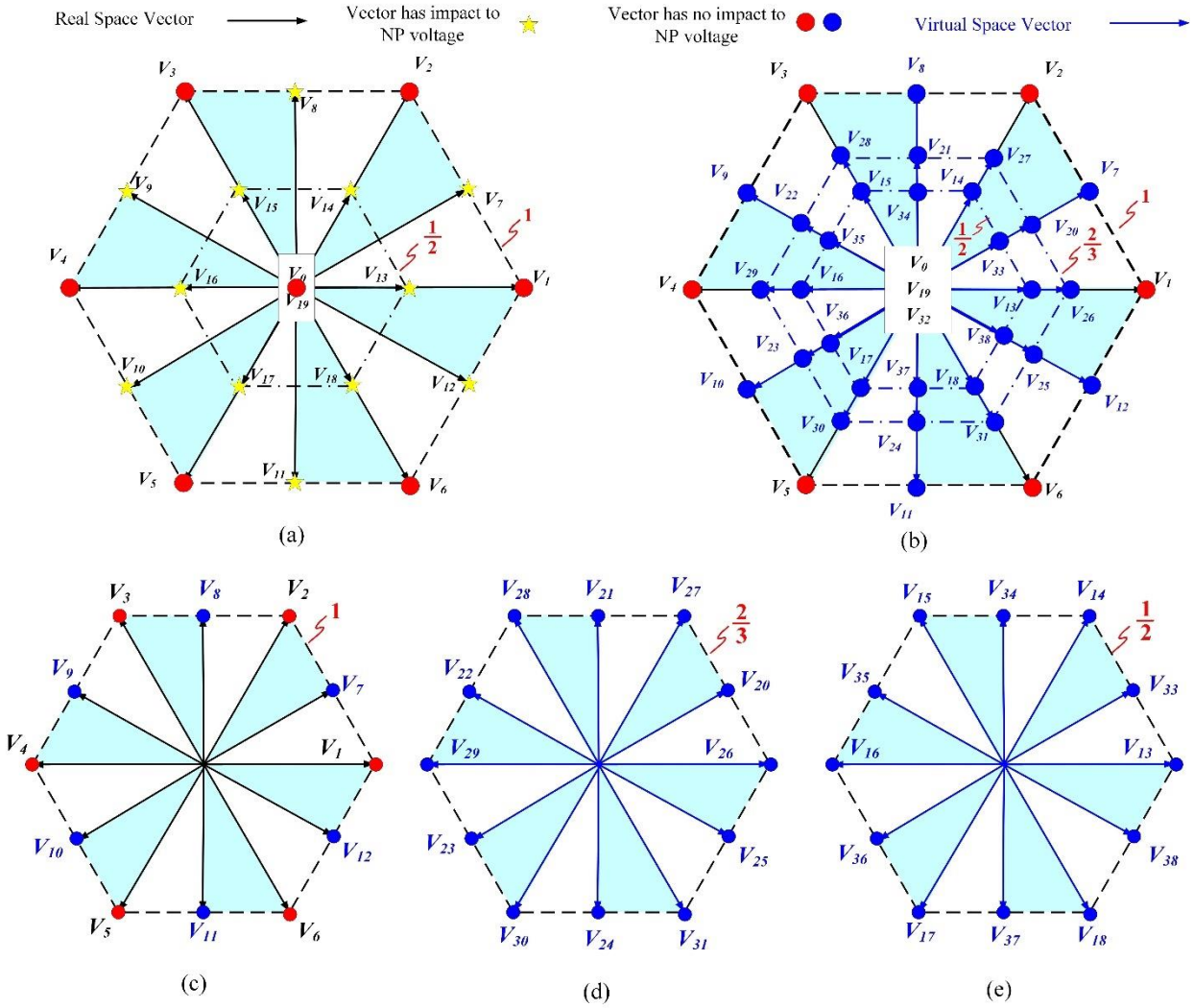

Figure 4.10: The proposed space vector diagram.

Figure 4.10 (b) is the proposed voltage space vector diagram. On the outer hexagon, the original medium RVV (V_7 ~ V_{12}) are all replaced by the VSVs, while the large RVVs remain the same. The VSVs replacing the original RVVs are still using the same vector numbers but

differentiated by a different color in Figure 4.10 (b). On the inner hexagon, the original small RVV (V_{13} ~ V_{18}) are all substituted by the VSVs. In addition, similar to the medium voltage vectors with their tips on the middle of the sides of the outer hexagon, six additional VSVs (V_{33} ~ V_{38}) were added, and their tips are on the middle of the sides of the inner hexagon. Likewise, to reduce the torque and flux ripple, a middle hexagon is added, which is formed by 12 new VSVs, i.e., V_{20} ~ V_{31}. The tips of VSVs V_{20} ~ V_{25} located on the middle of the sides of the middle hexagon, while the tips of VSVs V_{26} ~ V_{31} located on the vertices of the middle hexagon. The details of each hexagon are illustrated in Figure 4.10 (c)-(e).

All the 36 new non-zero voltage vectors in Figure 4.10 (b) are synthesized as follows,

1. The large voltage vectors, i.e., V_1 to V_6, are preserved same as the original since they do not affect the NP current.
2. The VSVs V_7 to V_{12} are synthesized by applying each of the two nearest large voltage vectors for $T_s/2$. Using V_7 as an example

$$\begin{aligned} V_i &= \frac{V_1[0]+V_2[0]}{2} = \frac{[P\ N\ N]+[P\ P\ N]}{2} \\ &= \left[\frac{1+1}{2}\ \frac{1+1}{2}\ \frac{0+1}{2}\ \frac{0+1}{2}\ \frac{0+0}{2}\ \frac{0+0}{2}\right] \\ &= [1\,1\ 0.5\ 0.5\ 0\ 0] \end{aligned} \tag{4.1}$$

For the new V_7, each of the V_1 with switching state PNN and V_2 with switching state PPN is applied for half of the sampling period, i.e., $T_s/2$. This new voltage vector is equivalent to middle RVV but does not contribute any NP current. In addition, it is obvious to observe from (4.1) that the elements in the extended form of the switching state for the VSV may be fractional number, which is different from RVV, where all the elements are either 1 or 0.

3. For the VSVs V_{13} to V_{18}, using V_{13} as an example,

$$\begin{aligned} V_{13} &= \frac{1}{2}\left(V_{13}[i_a]+V_{13}[-i_a]\right)=\frac{[P \quad O \quad O]+[O \quad N \quad N]}{2} \\ &=\left[\frac{1+0}{2} \quad \frac{1+1}{2} \quad \frac{0+0}{2} \quad \frac{1+0}{2} \quad \frac{0+0}{2} \quad \frac{1+0}{2}\right]=[0.5 \quad 1 \quad 0 \quad 0.5 \quad 0 \quad 0.5] \end{aligned} \tag{4.2}$$

where $V_{13}[i_a]$ is the original small RVV with switching state POO, which leads to an NP current i_a; $V_{13}[-i_a]$ has switching state ONN, which leads to an NP current $-i_a$. According to (4.2), if each vector is applied for half of the sampling period which is denoted as $T_s/2$, the average NP current over a sampling period T_s should be zero, such that when this synthesized VSV is applied, the NP voltage would not be affected.

4. The VSVs, V_{20} to V_{25}, are generated by the nearest two small RVVs and the middle RVV, so that the NP current is zero. For instance, V_{20} is synthesized as,

$$\begin{aligned} V_{20} &= \frac{1}{3}V_{13}[i_a]+\frac{1}{3}V_{14}[i_c]+\frac{1}{3}V_7[i_b] \\ &=\frac{[O \quad N \quad N]+[P \quad P \quad O]+[P \quad O \quad N]}{3} \\ &=\left[\frac{0+1+1}{3} \quad \frac{1+1+1}{3} \quad \frac{0+1+0}{3} \quad \frac{0+1+1}{3} \right. \\ &\left. \frac{0+0+0}{3} \quad \frac{0+1+0}{3}\right] \\ &=[0.6667 \quad 1 \quad 0.3333 \quad 0.6667 \quad 0 \quad 0.3333] \end{aligned} \tag{4.3}$$

5. The VSVs, V_{26} to V_{31} are synthesized by tacking 2/3 of their corresponding large voltage vectors and 1/3 of the zero-voltage vectors. For instance, V_{26} is calculated by,

$$
\begin{aligned}
V_{26} &= \frac{2}{3}V_1[0] + \frac{1}{3}V_{19}[0] = \frac{2}{3}[P \quad N \quad N] + \frac{1}{3}[N \quad N \quad N] \\
&= \left[\frac{(2\times 1)+0}{3} \quad \frac{(2\times 1)+0}{3} \quad \frac{(2\times 0)+0}{3} \quad \frac{(2\times 0)+0}{3} \right. \\
&\quad \left. \frac{(2\times 0)+0}{3} \quad \frac{(2\times 0)+0}{3} \right] \\
&= [0.6667 \quad 0.6667 \quad 0 \quad 0 \quad 0 \quad 0]
\end{aligned}
\tag{4.4}
$$

In (4.4), V_1 and V_{19} are used, which don't affect NP current, to generate V_{26}. Therefore, V_{26} does not affect have any effect on the NP current.

6. The VSVs, V_{33} to V_{38} are generated using the two nearest small VSVs. As an example, V_{33} is calculated as,

$$
\begin{aligned}
V_{33} &= \frac{1}{2}\left(V_{13}[0] + V_{14}[0]\right) = \left[\frac{0.5+0.5}{2} \quad \frac{1+1}{2} \quad \frac{0+0.5}{2} \quad \frac{0.5+1}{2} \quad \frac{0+0}{2} \quad \frac{0.5+0.5}{2} \right] \\
&= [0.5 \quad 1 \quad 0.25 \quad 0.75 \quad 0 \quad 0.5]
\end{aligned}
\tag{4.5}
$$

4.2.2.2 Proposed Multilevel Torque Hysteresis Controller

A multilevel torque hysteresis band is needed for the proposed novel DTC since the proposed voltage vector diagram has three layers of voltage hexagons, hence a six-level torque hysteresis controller as shown in Figure 4.11 is proposed and applied to the proposed advanced DTC. The $\pm HB_T$ represents the outer torque hysteresis band, while the $\pm\alpha \cdot HB_T$ and $\pm\beta \cdot HB_T$ are the inner and middle torque hysteresis bands, respectively. The values for the α and β coefficients are tuned offline to trade the dynamic response against the steady state torque tracking error. When the torque tracking error falls within the inner band, i.e., the output of the torque hysteresis $H_6(\Delta T_{em})$ = ±1, the voltage vector to be applied in the next control cycle is chosen from the vectors on the inner voltage hexagon, i.e., V_{13} ~ V_{18} and V_{33} ~ V_{38}, which has the lowest impact to the torque.

When the torque tracking error falls within the middle band, i.e., $H_6(\Delta T_{em}) = \pm 2$, the voltage vector to be applied in the next control cycle is chosen from the vectors on the middle voltage hexagon, i.e., $V_{20} \sim V_{25}$ and $V_{26} \sim V_{31}$, which has higher impact to the torque than the small voltage vectors due to the higher voltage magnitude. For other conditions, the outer voltage hexagon voltage vectors are applied. The proposed switching sequences or the voltage vectors depending on the torque and flux hysteresis loop is shown in Table 4.2.

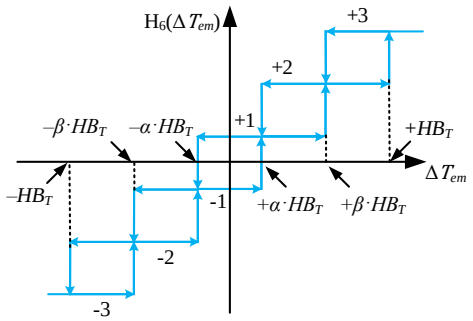

Figure 4.11: Modified 6-L torque comparator.

Table 4.2
The Switching Table of the Proposed DTC for 3-L Inverter

$H(\Delta\psi_s)$	$H_6(\Delta T_{em})$	Sector											
		1	2	3	4	5	6	7	8	9	10	11	12
+1	+3	V_2	V_8	V_3	V_9	V_4	V_{10}	V_5	V_{11}	V_6	V_{12}	V_1	V_7
	+2	V_{27}	V_{21}	V_{28}	V_{22}	V_{29}	V_{23}	V_{30}	V_{24}	V_{31}	V_{25}	V_{26}	V_{20}
	+1	V_{14}	V_{34}	V_{15}	V_{35}	V_{16}	V_{36}	V_{17}	V_{37}	V_{18}	V_{38}	V_{13}	V_{33}
	–1	V_{18}	V_{38}	V_{13}	V_{33}	V_{14}	V_{34}	V_{15}	V_{35}	V_{16}	V_{36}	V_{17}	V_{37}
	–2	V_{31}	V_{25}	V_{26}	V_{20}	V_{27}	V_{21}	V_{28}	V_{22}	V_{29}	V_{23}	V_{30}	V_{24}
	-3	V_{11}	V_6	V_{12}	V_1	V_7	V_2	V_8	V_3	V_9	V_4	V_{10}	V_5
–1	+3	V_8	V_3	V_9	V_4	V_{10}	V_5	V_{11}	V_6	V_{12}	V_1	V_7	V_2
	+2	V_{28}	V_{22}	V_{29}	V_{23}	V_{30}	V_{24}	V_{31}	V_{25}	V_{26}	V_{20}	V_{27}	V_{21}
	+1	V_{15}	V_{35}	V_{16}	V_{36}	V_{17}	V_{37}	V_{18}	V_{38}	V_{13}	V_{33}	V_{14}	V_{34}
	–1	V_{17}	V_{37}	V_{18}	V_{38}	V_{13}	V_{33}	V_{14}	V_{34}	V_{15}	V_{35}	V_{16}	V_{36}
	–2	V_{30}	V_{24}	V_{31}	V_{25}	V_{26}	V_{20}	V_{27}	V_{21}	V_{28}	V_{22}	V_{29}	V_{23}
	-3	V_5	V_{11}	V_6	V_{12}	V_1	V_7	V_2	V_8	V_3	V_9	V_4	V_{10}

4.2.2.3 Generate Gate Signals for the VSVs Using a Modulator

An external modulator [85]-[86] is used to generate the gate signals for the VSVs to be used in the proposed DTC controller. This modulator compares the elements in the extend form of the switching states of voltage vectors, which are similar to the duty ratios, selected by the DTC algorithm to a carrier waveform having a fixed switching frequency. As an example, Figure 4.12 shows gate signal generation for the VSV V_{25}, whose extended form of switching state is [$s_{a,1}$ $s_{a,2}$ $s_{b,1}$ $s_{b,2}$ $s_{c,1}$ $s_{c,2}$] = [2/3 1 0 1/3 1/3 2/3].

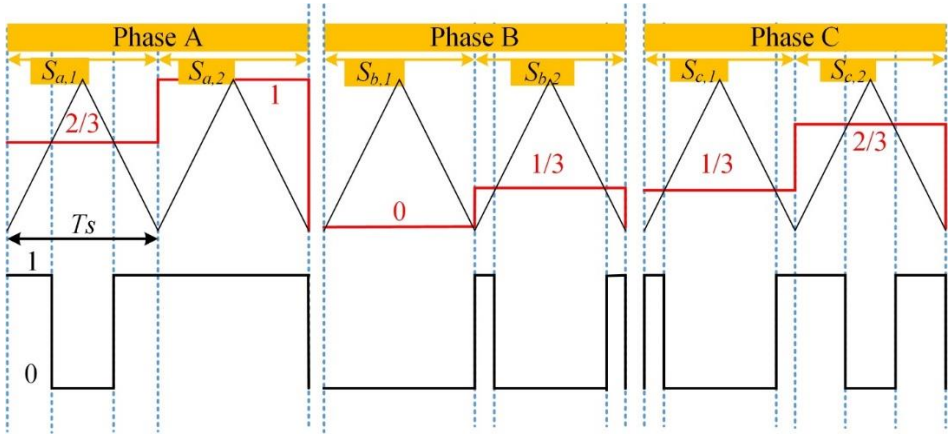

Figure 4.12: Gate signal generation of voltage vector V_{25}.

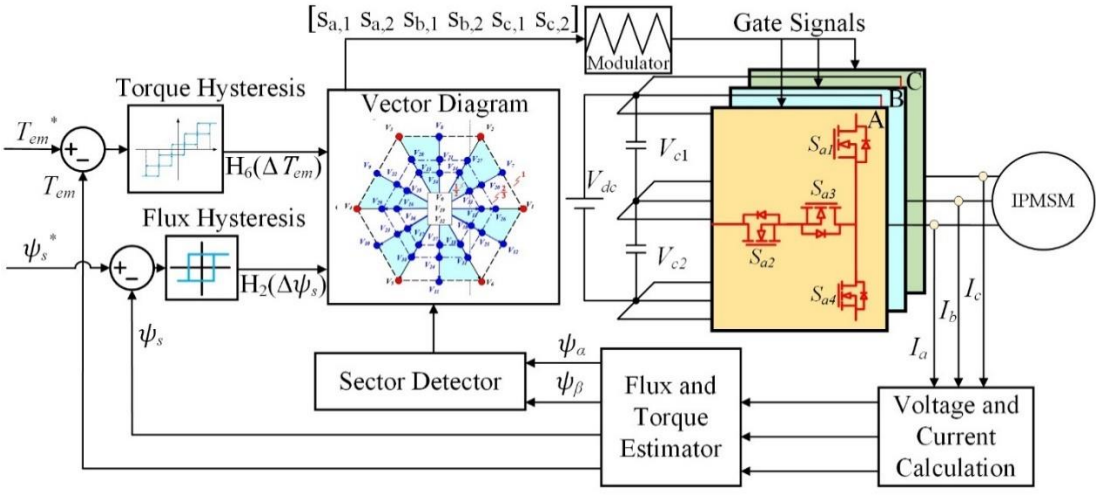

Figure 4.13: Overall block diagram of the proposed DTC.

4.2.2.4 Overview of the Proposed DTC

The block diagram of the proposed DTC approach is presented in the Figure 4.13, which still includes the hysteresis controllers for the stator flux linkage and the electromagnetic torque and their corresponding estimators. The flux hysteresis controller is the conventional 2-L hysteresis with the output as $H_2(\Delta\psi_s)$, as shown in Figure 4.2, while the torque hysteresis controller is the proposed 6-L hystersis, where the output is denoted as $H_6(\Delta T_{em})$ and shown in Figure 4.11. The $H_2(\Delta\psi_s)$ and $H_6(\Delta T_{em})$ are used to identify the optimal and proper voltage space vector to be applied in the next control cycle from the Table 4.2, which is the siwtching table for the proposed DTC. Once the optimal voltage space vector is selected, its extended form of switching state is sent to an external modulator which is shown in Figure 4.12 to generate all the gate signals for a T-type inverter. Due to the use of one or more voltage vectors over a control iteration, the equivalent switching frequency is higher than the conventional DTC, which helps reduce the current and torque ripples. Compared to the SVM-DTC, since the proposed DTC still uses the discrete voltage vectors, which preserve the major merits such as the fast-dynamic performance.

4.3 Conclusions

In this chapter, an enhanced DTC scheme was proposed for 3-L T-type converter with inherent dc link voltage balancing capability. As mentioned earlier in this chapter that the neutral point current flow is the reason behind the DC-link capacitor charging and discharging. Now if over one switching cycle the average of the neutral point current is not zero then the DC-link capacitor voltages are not balanced. This affects the other important variants in the system such as torque and stator current ripples. To eliminate the DC-link unbalancing issue and to reduce the torque ripples and stator current ripples, the novel DTC with virtual voltage vectors is propositioned. Due

to the use of the additional VSVs, compared with the conventional DTC, the proposed DTC can effectively have higher average switching frequency which also helps to reduce the torque and stator current ripples. The dynamic performance is similar to the conventional DTC since the proposed novel DTC used discrete number of voltage vectors.

CHAPTER 5

SIGNAL INJECTION BASED OPTIMAL REFERENCE FLUX SEARCHING APPROACHES FOR DIRECT TORQUE CONTROL

5.1 Introduction

As mentioned in the previous chapter, the DTC has two reference commands, i.e., torque and flux command. By definition the torque needs to be commanded externally for DTC algorithm. However, to improve the efficiency of the DTC it is important to make sue the DTC is running in optimum flux command which is also known as the maximum torque per ampere (MTPA) condition. The MTPA approach is not only needed for the efficiency improvement but it also improves the power density of modern AC drives. The fundamental objective of the MTPA algorithm is to generate required electromagnetic torque using the smallest stator current possible for a particular operating condition, such that the motor copper losses can be significantly reduced.

The maximum torque per ampere (MTPA) strategy is often necessary for an FOC based IPM drive system to improve the efficiency and power density [87]. The basic idea to get MTPA point for FOC is to nullify the stator flux component along *d*-axis [88]. This can be achieved by making *d*- axis stator current component to zero. For FOC method, different MTPA approaches can be found in several papers. In [89], a sinusoidal perturbation signal is used to detect the MTPA point for field oriented control. In [90], MTPA is achieved by calculating reference *d*- and *q*- axis current for a constant torque region. MTPA operation also can be obtained by implementing synchronous reference frame by controlling the reference flux amplitude according to [91]. In [92], MTPA is implemented using signal injection method like [90], [93], [94], [45] and [44] with modification by implementing extremum seeking control for synchronous permanent magnet motors. The

synchronous reference frame based approach for vector control has some disadvantage due to machine parameters uncertainty and nonlinearity [36]. There is a virtual signal injection method [95], [96] to track MTPA points, robust to flux observer error and motor parameters variation in MTPA points. Though this control scheme does not cause any iron loss as it is based on virtual signal injection, however it is a method with slow converging rate and poor dynamic response. On the other hand, not much of work has been done for MTPA in direct torque control in IPM motors. DTC has several advantages in terms of control. DTC does not need any current loop and does not need any rotor positions. The optimal flux searching approach can also be implemented in DTC of IPM motors. Generally, existing optimal ψ_s^* selection methods can be classified into two categories, i.e., the look-up table (LUT) based approach and the direct calculation method [90], [52] and [49]. In the first category, time consuming offline tuning is required to find out the optimal flux reference for each operating point and then these optimal references will be stored in a LUT to be utilized in the controller. Most of the MTPA approach use LUT based reference flux searching approach because of the complexity between the torque and stator flux linkage relation in direct calculation method [52]. The direct calculation method also relies on the machine model, which usually assumes that the motor parameters are constant, which however is not always valid, since IPM, motor parameters are affected by the stator currents, magnetic saturation, cross coupling effect and temperature. Therefore, both methods have obvious disadvantages, e.g., needs tremendous tuning effort and/or vulnerable to the variations of machine parameters. To reduce the dependency on motor parameters for MTPA approach, a flux searching approach has been proposed for DTC in [52]. The approach does not have any dependency of machine parameters; however, its accuracy is affected by voltage and current harmonics and torque variations. In [36], a signal injection based MTPA point tracking algorithm is proposed which is based on extremum

seeking control (ESC) [97] and [98]. The MTPA tracking method used in [36], is based on a random signal injection with variable frequency instead of using fixed frequency to avoid the residual torque harmonic at the injected signal frequency. Due to random signal injection and variable frequency, additional copper/iron losses will occur. Moreover, the MTPA control quality would degrade because of the errors in flux observer.

In this chapter, first a brief analysis, mathematical and graphical representation are discussed. Then the signal injection based Perturb and Observe (P&O) method is proposed. To eliminate the drawbacks of the P&O further, an extremum seeking control algorithm is proposed for optimal flux searching for DTC.

5.2 Maximum Torque Per Ampere (MTPA) for IPM Motor

It is important to understand the relationship between the optimal flux reference and the MTPA operating points before proposing a better flux searching algorithm than the current state of the art. The dynamics of the machine model is already presented in Chapter 2. From (2.3) and (2.4), both the magnitude of the stator current, i.e., $|I_s|$, and $|\psi_s|$ can be expressed as a function of i_d, i.e., $f(i_d)$ and $g(i_d)$, respectively.

$$|I_s| = \sqrt{i_d^2 + \frac{4}{9}\frac{T_{em,0}^2}{P^2\left[\psi_m + \left(L_d - L_q\right)i_d\right]^2}} = f\left(i_d\right) \tag{5.1}$$

$$|\psi_s| = \sqrt{\left(\psi_m + L_d i_d\right)^2 + \frac{4}{9}\frac{L_q^2 T_{em,0}^2}{P^2\left[\psi_m + \left(L_d - L_q\right)i_d\right]^2}} = g\left(i_d\right) \tag{5.2}$$

Combining the two equations (2.4) and (5.1) to eliminate i_d will result in a relationship between $|I_s|$ and $|\psi_s|$, which however cannot be expressed explicitly due to its highly nonlinear behavior.

Therefore, in this chapter a numerical analysis is performed to study the relationship between $|I_s|$ and $|\psi_s|$. Figure 5.1 shows the nonlinear relationship between the $|I_s|$ and $|\psi_s|$, considering an IPM motor with major parameters shown in Table A-1 in appendix section. For all possible, i_d, e.g., $i_d \in [-10, 10]$ A. At each specific command torque, the figure of $|I_s|$ vs. $|\psi_s|$ is a convex and a unique optimal ψ_s^* exists which leads to the minimum $|I_s|$, e.g., the red circles shown in Figure 5.1. If this optimal ψ_s^* point can be identified online, the corresponding torque $T_{em,0}$ can be achieved with the minimum stator current, $|I_s|$. This concept is identical to the basic idea of MTPA, which however describes the relationship between $|I_s|$ and T_{em}. The relationship between i_d and i_q for MTPA trajectory [90] and [28] can be expressed as

$$i_d = \frac{\psi_m}{2\left(L_q - L_d\right)} - \sqrt{\frac{\psi_m^2}{4\left(L_q - L_d\right)^2} + i_q^2} \tag{5.3}$$

Using (5.2) and (5.3), it is possible to plot the profile of $|I_s|$ vs. $|\psi_s|$ under MTPA condition, which is represented by the black vertical segment in Figure 5.1. It worth to be noted that this MTPA trajectory crosses every optimal reference flux, ψ_s*, which indicates that these optimal reference flux, ψ_s* are equivalent to the MTPA operating points. Therefore, if the IPM DTC drive operates at these optimal ψ_s*, the MTPA operation condition can be achieved successfully.

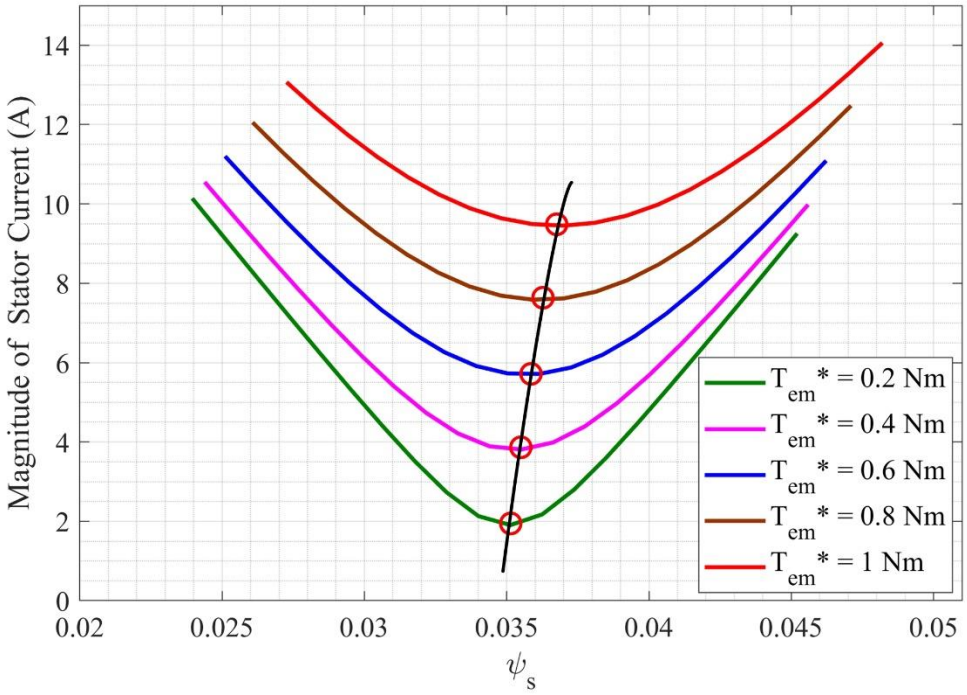

Figure 5.1: The profiles of $|I_s|$ vs. $|\psi_s|$ at different torque operating points.

5.3 Perturb and Observe Method for Two-Level Inverter-fed DTC

In this section, a perturbation and observation (P&O) control, which is also known as the hill-climb search method [99] is proposed to find the optimal reference stator flux linkage, ψ_s^* online. Any prior knowledge of the drive system is not needed for the proposed method, and it is totally independent of the machine parameters. Therefore, any offline tuning procedure is unnecessary, and this method will be robust against parametric variations of the IPM motor. The proposed P&O method has been widely used in maximum power point tracking (MPPT) for renewable energy conversions [9].

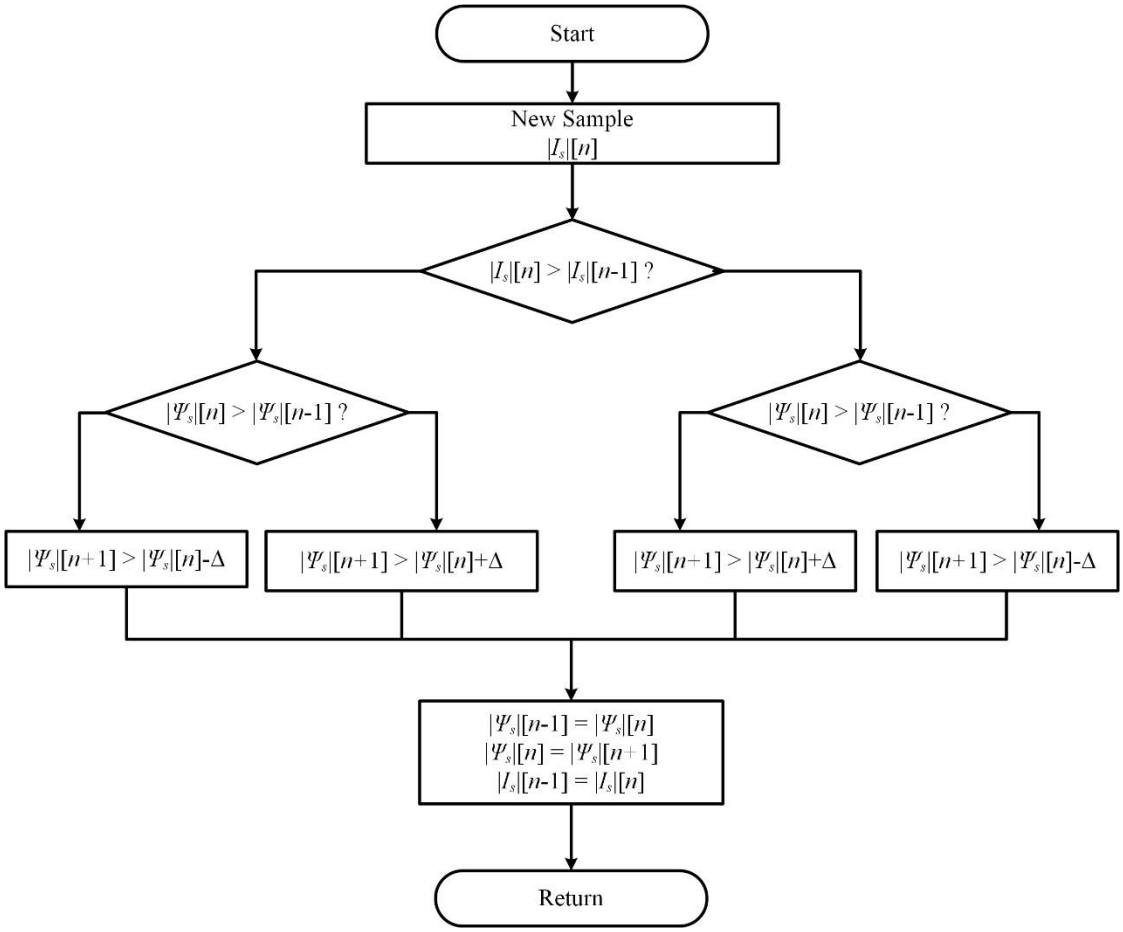

Figure 5.2: The flow chart of the proposed optimal ψ_s^* searching algorithm.

A flow chart of the proposed online optimal ψ_s^* searching algorithm [28] is presented in Figure 5.2. During the search process, the reference ψ_s^* is continuously adjusted by a constant increment or decrement of Δ in each step, i.e., the period of the search algorithm, which is different from the sampling period of the main DTC algorithm. The magnitude of the injected Δ will lead to a variation of the magnitude of the stator current, I_s. As shown in Figure 5.2, when the stator flux reference is smaller than its optimal value which is left hand side of the minimum point of the curve shown in Figure 5.1, the increase of $|\psi_s|$ will lead to the decrease of $|I_s|$; when the stator flux reference is larger than its optimal value which is the right side of the minimum point of the curve shown in Figure 5.1, the increase of $|\psi_s|$ will lead to the increase of $|I_s|$. Therefore, by evaluating

the difference between two consecutive current samples $I_s[n]$ and $I_s[n–1]$, i.e., $|I_s|[n] – |I_s|[n–1]$, and $|\psi_s|[n] – |\psi_s|[n–1]$, the proposed approach's flow chart shown in Figure 5.2 will be able to identify the reference stator flux to be used for the next step online.

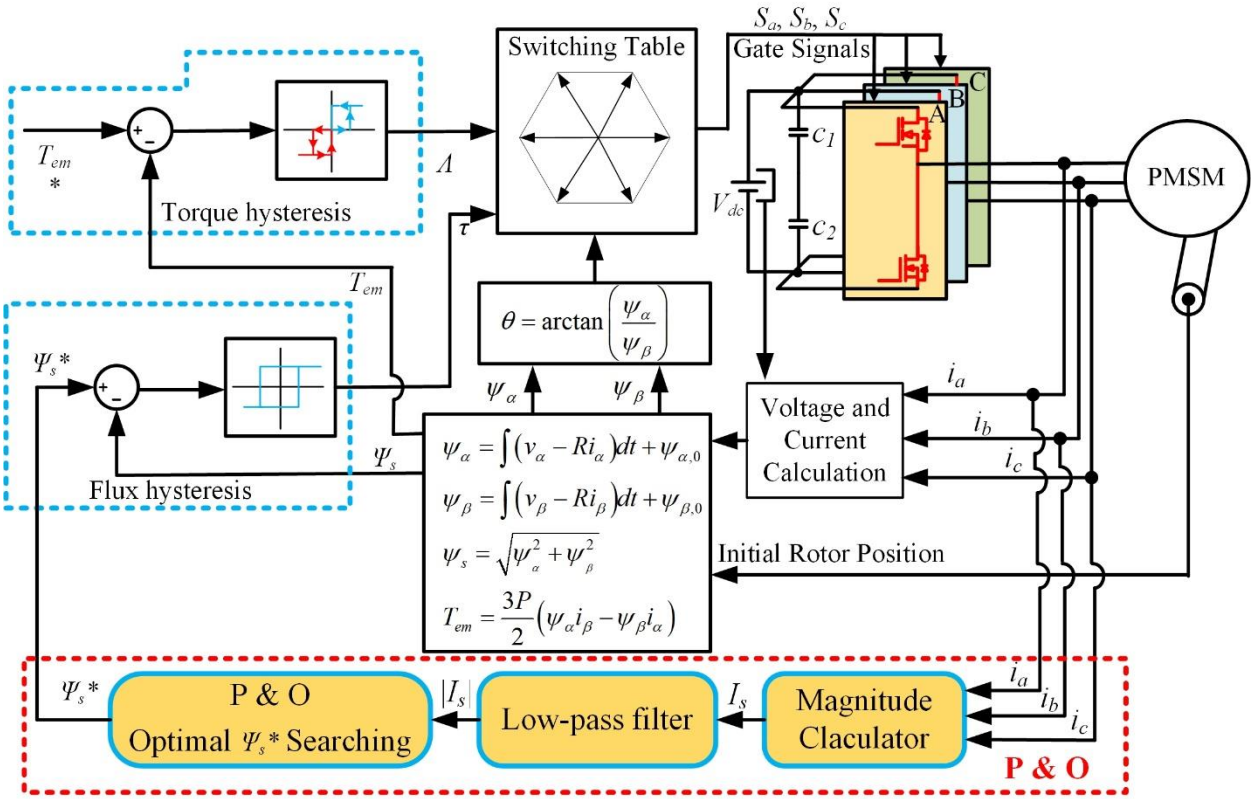

Figure 5.3An overall block diagram of the DTC drive with the proposed online optimal ψ_s^* searching algorithm.

The overall block diagram of the DTC integrated with proposed optimal ψ_s^* searching algorithm is illustrated in Figure 5.3. In addition to the online optimal ψ_s^* searching algorithm, a magnitude calculator, which is designed to determine the $|I_s|$, and a moving average based low pass filter (LPF) are required.

5.4 Extremum Seeking Control Algorithm (ESC)

In this section, to discourse the issues with existing signal injection-based flux searching approaches, an ESC algorithm is proposed to find the optimal stator flux reference in real-time

more efficiently and quickly. The ESC is a non-model based real-time optimization approach [97] from adaptive control algorithm family, which mostly deals with the system, where the reference to output map cannot be expressed unequivocally but an extremum does exist. The ESC approach was firstly presented in early 1920s in Leblance's work to find the resonance peak of an electromechanical system [100]. The nonlinear nature of this kind of adaptive controller was shown in [90], [101]. It is an alternative approach to the offline techniques and other signal injection-based techniques that depends on the predetermined information and/or machine model parameters. The basic idea of ESC for DTC is to inject a high frequency sinusoidal signal with a small magnitude in the flux control loop and the system response can be extracted from the stator current which has the information of the effect of signal injection in flux control loop and that can be exploited to identify the optimal flux reference. There are various implementation methods for the ESC, however maintaining system stability is difficult. In this chapter, the proposed novel ESC algorithm can ensure the effectiveness of optimal reference flux search while maintaining stability.

5.4.1 Extremum Seeking Control Algorithm for Advanced DTC

In DTC algorithm, the torque reference either can be a directly commanded value or obtained from the output of a speed regulator. The ψ_s^*, which is the reference of the stator flux at a certain operating condition, i.e., a specific combination of motor speed, torque, and DC bus voltage, can be obtained using optimization strategies which are similar to the MTPA for FOC. However, the existing optimal ψ_s^* selection methods, i.e., LUT-based and the direct calculation methods, have obvious disadvantages, e.g., require tremendous tuning effort and/or vulnerable to the variations of machine parameters. Therefore, a novel extremum seeking control algorithm is proposed for direct torque control approach.

5.4.2 Boundary condition for Extremum Seeking Control Algorithm

From (2.2) from chapter 2, *d, q* axis stator currents, i_d and i_q respectively can be rewritten as,

$$i_d = \frac{\psi_d - \psi_m}{L_d} \text{ and } i_q = \frac{\psi_q}{L_q} \tag{5.4}$$

Substituting (5.4) into (2.4), the equation for the electromagnetic torque can further written as,

$$T_{em} = \frac{3}{2} P \left[\frac{\psi_m}{L_d} \psi_q + (\frac{1}{L_q} - \frac{1}{L_d}) \psi_d \psi_q \right] \tag{5.5}$$

In (5.5), *d* and *q* axis flux linkage can be articulated in the polar form as, $\psi_d = \psi_s \cdot \cos\delta$ and $\psi_q = \psi_s \cdot \sin\delta$, where δ is the load angle, which is the angle between the stator and rotor flux linkages. Now, the torque equation (5.5) becomes,

$$T_{em} = \frac{3}{2} P \frac{\psi_m \psi_s}{L_d} \sin\delta + \frac{3}{4} P \left(\frac{1}{L_q} - \frac{1}{L_d} \right) \psi_s^2 \sin(2\delta) \tag{5.6}$$

Equation (5.6) specifies that the electromagnetic torque is a function of load angle. To ensure the increase and decrease of the torque T_{em} by increasing and decreasing δ respectively, it is important to find monotonic increasing region for (5.6) [79], i.e., $\frac{dT_{em}}{d\delta} > 0$, where $\frac{dT_{em}}{d\delta}$ can be derived as

$$\frac{dT_{em}}{d\delta} = \frac{3}{2} P \frac{\psi_m \psi_s}{L_d} \cos\delta + \frac{3}{2} P \left(\frac{1}{L_q} - \frac{1}{L_d} \right) \psi_s^2 \cos(2\delta) \tag{5.7}$$

To ensure $\frac{dT_{em}}{d\delta} > 0$, following condition needs to be met,

$$\cos(\delta) < \frac{\psi_m + \sqrt{\psi_m^2 + 8\chi^2 \psi_s^2}}{4\chi\psi_s} \tag{5.8}$$

where $\chi = \frac{L_q - L_d}{L_d}$. For a salient pole IPM motor, since $L_q > L_d$, χ is always positive and (5.8) can be further presented as,

$$\begin{cases} -\frac{\pi}{2} < \delta < -\cos^{-1}\left(\frac{\psi_m + \sqrt{\psi_m^2 + 8\chi^2\psi_s^2}}{4\chi\psi_s}\right) \\ \cos^{-1}\left(\frac{\psi_m + \sqrt{\psi_m^2 + 8\chi^2\psi_s^2}}{4\chi\psi_s}\right) < \delta < \frac{\pi}{2} \end{cases} \tag{5.9}$$

Since the monotonic increasing region is expected to cover the whole range of load angle from $-\frac{\pi}{2}$ to $\frac{\pi}{2}$ [79], therefore,

$$\frac{\psi_m + \sqrt{\psi_m^2 + 8\chi^2\psi_s^2}}{4\chi\psi_s} > 1 \tag{5.10}$$

which further leads to

$$\psi_s < \frac{\psi_m}{\chi} = \frac{L_d}{L_q - L_d}\psi_m \tag{5.11}$$

which is the boundary condition that must be considered when the reference stator flux is chosen for DTC.

5.4.3 The Proposed ESC and the Related Signal Processing

The ESC is a non-model based real-time optimization approach for dynamic problems where only limited knowledge of a system is available, such as a system has a nonlinear equilibrium map, which has local minimum or maximum. Several books on ESC were published in 1950s-1960s [90]. The nonlinear nature of this kind of adaptive controller was shown in [101].

A novel ESC algorithm is proposed for the IPM motor to find the optimal reference flux, i.e., ψ_{op}^*, in real-time in this section. This flux searching approach does not require prior knowledge of the motor drive system which is a great advantage for a searching algorithm. In the searching process, a high frequency pulsating signal, i.e., $\psi_{s,h}^* = A\sin(\omega_c t)$, where A is the amplitude and ω_c is pulsating frequency, is injected and superposed onto the original stator flux reference $\psi_{s,0}^*$. According to Figure 5.4, when $\psi_{s,h}^*$ signal is injected, high frequency response can be found in the stator current, which can be denoted as

$$I_s \approx \bar{I}_s + \tilde{I}_s = \bar{I}_s + A \cdot \frac{dI_s}{d\psi_s} \cdot \sin(\omega_c t) \tag{5.12}$$

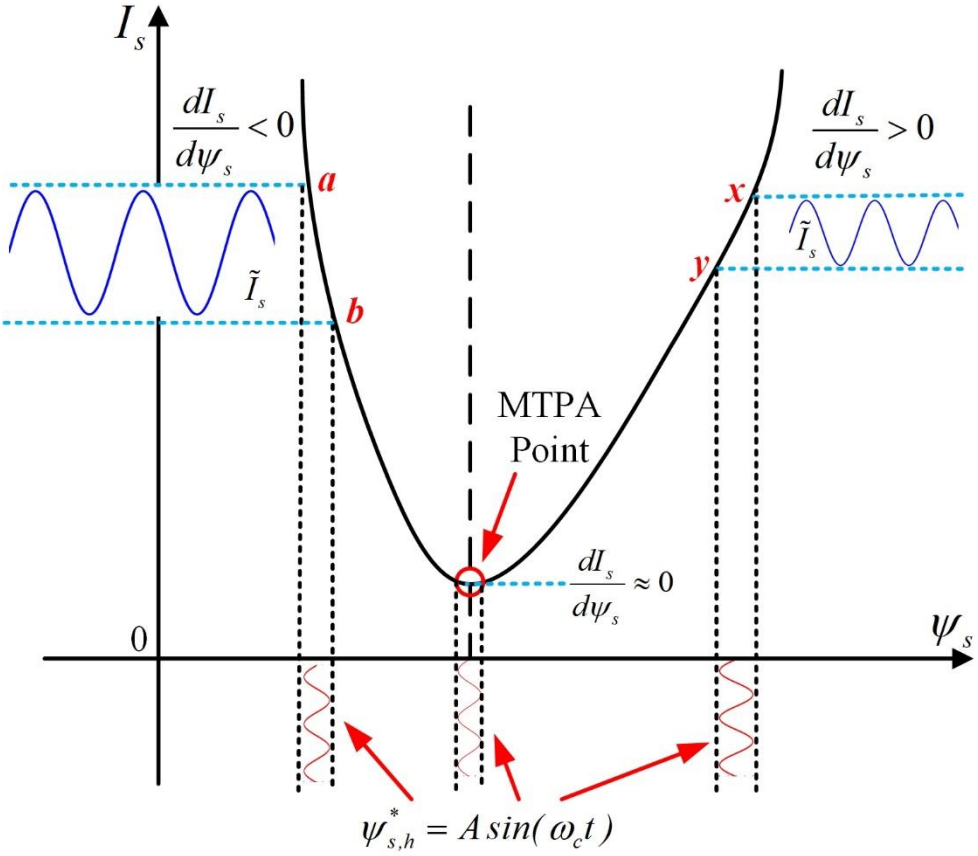

Figure 5.4: An illustration for the response of the stator current to injected high frequency stator flux.

where $\bar{I}_s$ stands for the steady state response to $\psi_{s,0}^*$ and $\tilde{I}_s$ is the high frequency response to $\psi_{s,h}^*$. As exhibited in Figure 5.4, the stator current may have different responses to the injected high frequency signal, $\psi_{s,h}^*$, which depends on the operating point of the IPM motor. When IPM operates on the left hand side of the MTPA operating point, $dI_s/d\psi_s$ is negative, while when IPM operates on the right hand side of the MTPA operating point, $dI_s/d\psi_s$ is positive. If IPM operates exactly at MTPA operating point, theoretically $dI_s/d\psi_s$ is 0. Therefore, with the injected high frequency signal, $\psi_{s,h}^*$, based on the information of $dI_s/d\psi_s$, which can be extracted from I_s, ESC can be designed to enforce the IPM to operate at the MTPA operating points.

The block diagram of the proposed novel ESC is presented in Figure 5.5. The magnitude of stator current can be calculated based on the measured phase currents i_a, i_b and i_c. Then, using an HPF, the high frequency response term $\tilde{I}_s$ in (5.12), which contains the information of $dI_s/d\psi_s$, can be extracted. To extract the information of $dI_s/d\psi_s$, a demodulator is designed using $\psi_{s,h}^*$ since, $dI_s/d\psi_s$ in $\tilde{I}_s$ is modulated by the injected high frequency sinusoidal signal and represented as,

$$\tilde{I}_s \cdot \psi_{s,h}^* = A^2 \cdot \frac{dI_s}{d\psi_s} \cdot \sin^2(\omega_c t) = \frac{A^2}{2}\frac{dI_s}{d\psi_s} - \frac{A^2}{2}\frac{dI_s}{d\psi_s}\sin(2\omega_c t) \tag{5.13}$$

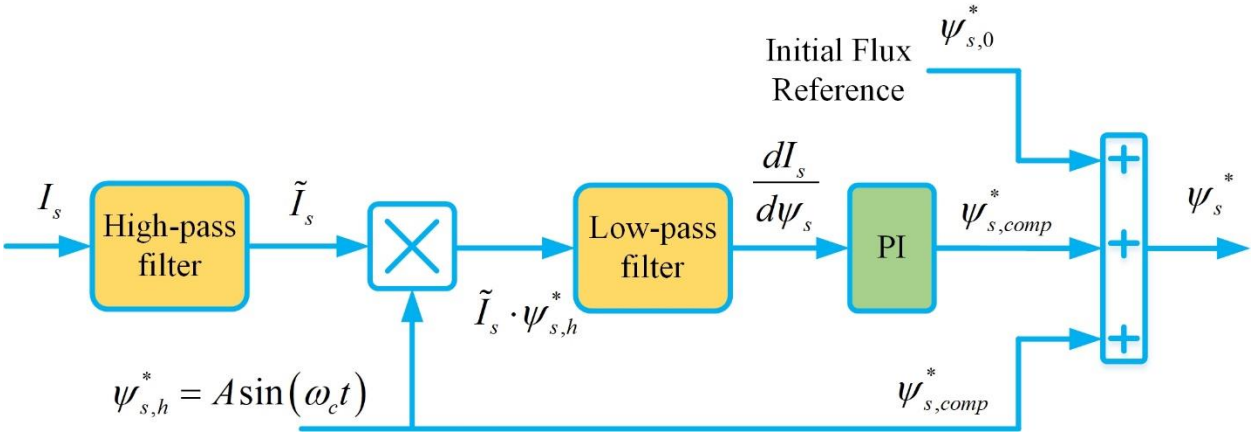

Figure 5.5: The block diagram of the proposed ESC algorithm.

As expressed in (5.13), $\tilde{I}_s \cdot \psi^*_{s,h}$ contains of a dc term, which is proportional to $dI_s/d\psi_s$, and a high frequency term. Then using a low-pass filter, the information of $dI_s/d\psi_s$ can be extracted. To ensure the optimal operating, in this work, a proportional integral (PI) controller is designed to administer $dI_s/d\psi_s$ to be zero.

$$\psi^*_{s,comp} = \left(k_p + \frac{k_i}{s} \right) \cdot \frac{dI_s}{d\psi_s} \tag{5.14}$$

where, k_p and k_i are the PI gains. The output of the PI stage, i.e., $\psi^*_{s,comp}$ is used as a compensation term as part of the stator flux reference, i.e.,

$$\psi^*_s = \psi^*_{s,0} + \psi^*_{s,comp} + \psi^*_{s,h} \tag{5.15}$$

5.4.4 Stability Analysis of ESC based Optimal Reference Flux Searching

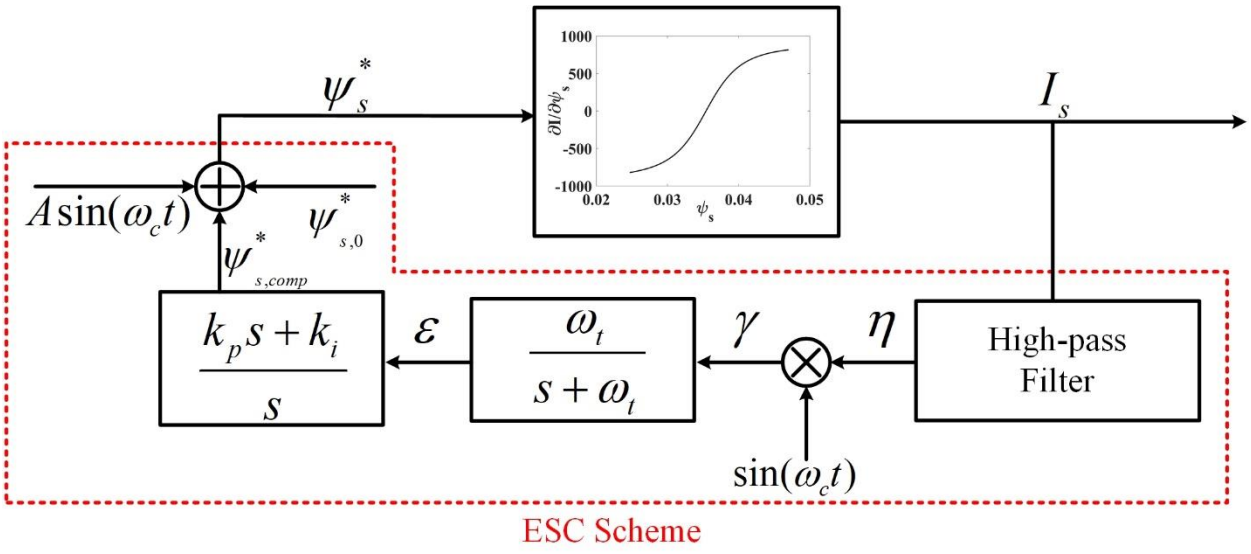

Figure 5.6: Equivalent DTC controlled PMSM with ESC.

Since the proposed ESC determines the optimal reference flux for the DTC of the PMSM, the stability analysis of the proposed ESC is critical for the appropriate system operation. The stability analysis for the ESC and/or other similar approach for reference flux searching is usually

performed in the existing literature. However, from the system perspective, an IPM motor is controlled by DTC, and the proposed ESC generate the reference flux for the DTC, leading to a coupled ESC-DTC-IPM system. Therefore, the stability analysis for ESC algorithm itself is not adequate. In this section, a stability analysis is performed for close-loop ESC-DTC-IPM system.

Figure 5.6 shows the equivalent block diagram of a DTC controlled IPM system structure, where the reference flux ψ_s^* in the DTC is generated by the proposed ESC scheme. As the dynamic response of the DTC controlled IPM system is much faster than that of the ESC scheme, the flux, torque, and stator current can be considered as constant quantities when designing the ESC. Therefore, the equivalent plant controlled by ESC could be regarded as a static map [102], [103] from flux ψ_s to the amplitude of the stator current $|I_s|$, i.e., $|I_s| = K(\psi_s)$, and the typical map is given in Figure 5.1. The objective of the ESC scheme is to find the optimal reference flux leading to the minimized stator current. As the map from the flux to the amplitude of the stator current is nonlinear, a small signal model is used here to analyze the stability of the system, which could be expressed as

$$\Delta I_s = \left.\frac{\partial I_s}{\partial \psi_s}\right|_{I_s=\bar{I}_s,\ \psi_s=\bar{\psi}_s} \cdot \Delta\psi_s \tag{5.16-a}$$

$$G_\psi\left(\bar{I}_s, \bar{\psi}_s\right) = \left.\frac{\partial I_s}{\partial \psi_s}\right|_{I_s=\bar{I}_s,\ \psi_s=\bar{\psi}_s} = 3P\sqrt{\frac{m}{2l}} \cdot \frac{g-l}{h-m} = G_\psi\left(\bar{I}_d\right) \tag{5.16-b}$$

where $\bar{I}_s$ and $\bar{\psi}_s$ are the values for I_s and ψ_s at a given equilibrium point, respectively; ΔI_s and $\Delta\psi_s$ are the variations of I_s and ψ_s, respectively. $G_\psi\left(\bar{I}_s, \bar{\psi}_s\right)$ represents the small signal gain, which is a constant and determined by $\bar{I}_s$ and $\bar{\psi}_s$ at the equilibrium point. According to (5.1) and (5.2),

since both I_s and ψ_s can be written as a function of i_d, $G_\psi\left(\bar{I}_s,\bar{\psi}_s\right)$ can be converted to a function of i_d, as shown in (5.16-b), where $\bar{I}_d$ is the value of i_d at the equilibrium point. The expressions of *g*, *l*, *h*, and *m* are presented in the Appendix A-1. As a numerical example, Figure 5.7 shows the small signal model from ψ_s to I_s, i.e., $G_\psi\left(\bar{I}_s,\bar{\psi}_s\right)$, under different torque and flux combinations. When $G_\psi = 0$, it represents the condition for the optimal reference flux and the trajectory of the corresponding optimal reference flux is shown in Figure 5.7 indicated by the red line.

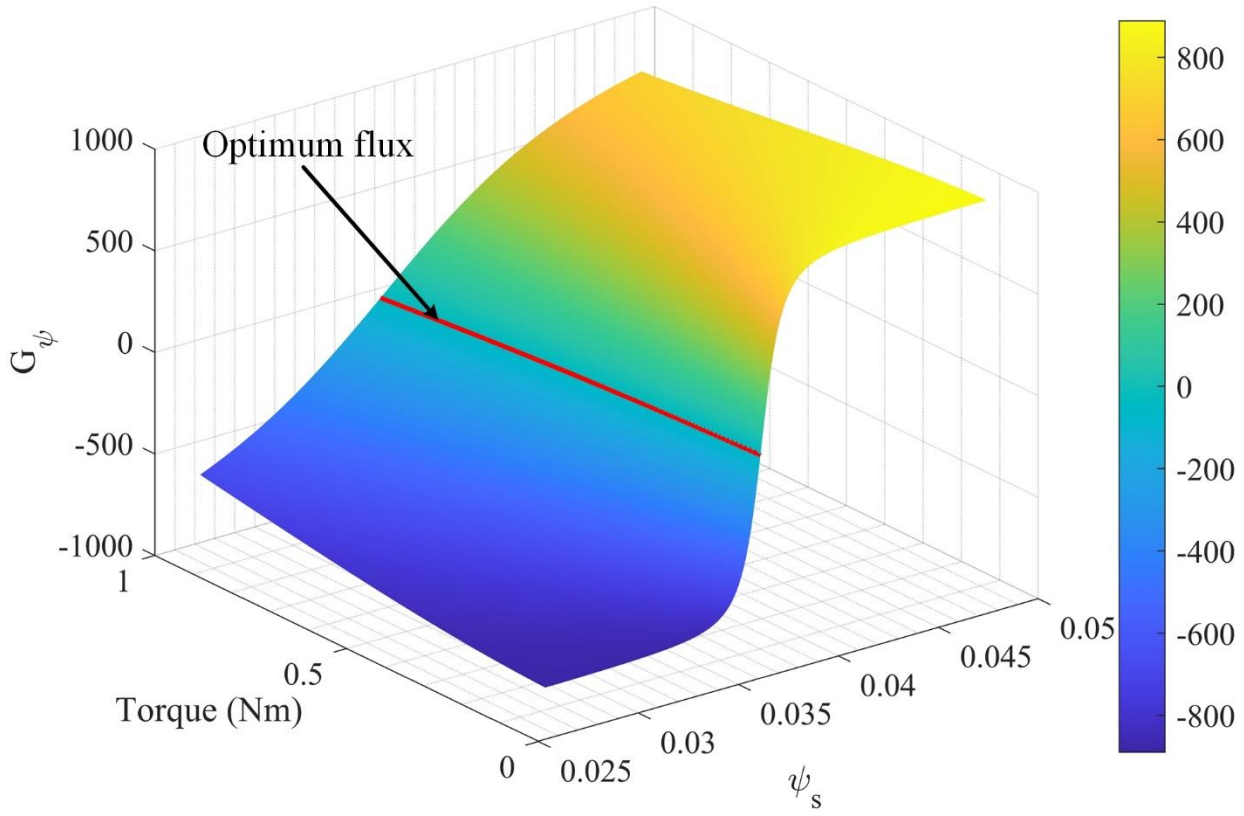

Figure 5.7: A numerical example of the small-signal model of the nonlinear map $|I_s| = f(\psi_s)$.

According to (5.16-a), the injected small signal $A\sin(\omega_c t)$ will be amplified by G_ψ times at a given stator flux $\bar{\psi}_s$. This amplified high frequency signal can be obtained by using a high pass filter (HPF) as

$$\eta = A \cdot G_\psi \cdot \sin\left(\omega_c t + \phi\right) \tag{5.17}$$

where ϕ is the phase shift is contributed by the HPF at the frequency ω_c. To recover G_ψ from η, a demodulation process is used, and the high frequency signal is demodulated to

$$\begin{aligned} \gamma &= A \cdot G_\psi \cdot \sin\left(\omega_c t + \phi\right)\sin\left(\omega_c t\right) \\ &= \frac{1}{2} A \cdot G_\psi \cdot \cos\phi - \frac{1}{2} A \cdot G_\psi \cdot \cos\left(2\omega_c t + \phi\right) \end{aligned} \tag{5.18}$$

With an appropriately designed low-pass filter $\alpha/(s+\alpha)$, the low frequency component in γ, which can be written as ε, will be amplified by the PI controller $(k_p s+k_i)/s$, where $k_i = \alpha k_p$. Assuming ψ_{op}^* is the optimal reference flux, the flux tracking error, defined as $\psi_e = \psi_{op}^* - \psi_{s,0}^* - \psi_{comp}^*$, satisfies,

$$\frac{d\psi_e}{dt} = -\frac{d\psi_{comp}^*}{dt} = -\left(k_p \frac{d\varepsilon}{dt} + k_i \varepsilon\right) = -\frac{1}{2}\alpha k_p A \cdot G_\psi \cdot \cos\phi \tag{5.19}$$

It should be noted that the small signal model G_ψ satisfies

$$\begin{cases} G_\psi > 0, & \psi_s > \psi_{op}^* \\ G_\psi = 0, & \psi_s = \psi_{op}^* \\ G_\psi < 0, & \psi_s < \psi_{op}^* \end{cases} \tag{5.20}$$

Define an energy function as $V = \frac{1}{2}\psi_e^2$ [104], the derivative of the energy function can be written as,

$$\frac{dV}{dt} = \psi_e \frac{d\psi_e}{dt} = -\left(\psi_{op}^* - \psi_{s,0}^* - \psi_{comp}^*\right)\frac{1}{2} k_i \cdot G_\psi \cdot \cos\phi \tag{5.21}$$

It should be noticed that the $\partial I_s / \partial \psi_s$ has the opposite sign with ψ_e. Based on the Lyapunov theory, the system is stable if $dV/dt < 0$, which means that the PI controller should satisfy $k_i > 0$ if $\phi > 90°$, or $k_i < 0$ if $0 < \phi < 90°$. It should be also noticed that the dynamic response of the HPF is ignored in the previous analysis; however, it will also affect the system stability. A properly designed HPF $G_h(s)$ should satisfy $\|G_h\|_\infty \leq 1$, which means the gain of the HPF filter is less or equal to 1 in over the entire frequency spectrum. Then the overall system can be represented using Figure 5.8. Based on the small-gain theorem [104], the system is stable if $\left\| G_\psi k_i \frac{G_h}{s} \right\|_\infty < 1$. Therefore, the upper limit of $|k_i|$ should be $\left\| G_\psi \frac{G_h}{s} \right\|_\infty^{-1}$.

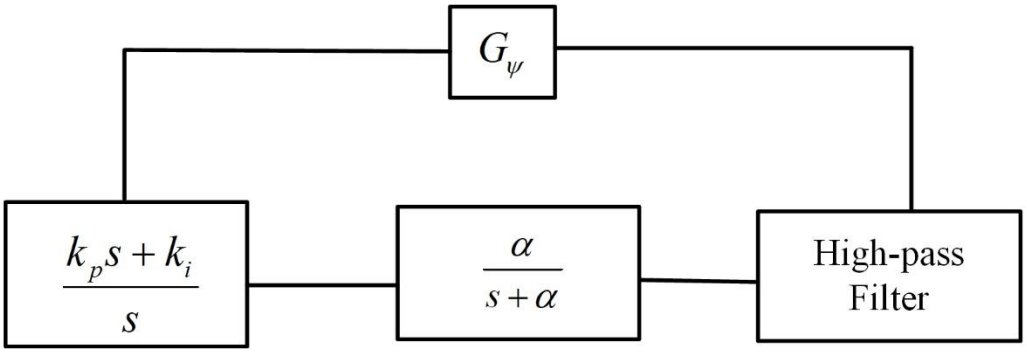

Figure 5.8: An overall block diagram of the coupled close-loop ESC and the DTC-controlled IPM motor.

5.5 The Selection of the High Frequency Signal for ESC

The amplitude of the high frequency signal has a noteworthy impact on the settling time of the ESC algorithm, which is related to the convergence rate of the algorithm, and stator currents THD, which is related to the torque ripple. To evaluate the effect of $\Delta\psi_s$ on the settling time and current THD, various $\Delta\psi_s$ from 1% to 5% of stator flux are used. The maximum value for THD, i.e., 41.92% and settling time, i.e., 0.035 s are considered as the base value for PU value calculation.

Figure 5.9, shows the relationship between the normalized settling time of ESC, i.e., ζ, shown in PU values vs. the amplitude of the injected signal, while Figure 5.10, shows the normalized current THD shown in PU value vs. the amplitude of the injected signal. It is clear that THD value is proportional to the amplitude of the injected signal whereas settling time of the ESC is inversely proportional to the amplitude of the injected signal. Therefore, it is possible to select an optimal amplitude for the injected signal based on the information given in Figure 5.9 and Figure 5.10. For instance, if $\Delta\psi_s$ is 4% of the ψ_s, the settling time to reach the steady state would be only 0.012 s but the current THD would be 32%. If $\Delta\psi_s$ is 0.5% of the ψ_s, settling time would be 0.035 s that is longer than before, however the THD would be only 7.92%. It is a tradeoff between the THD and settling time.

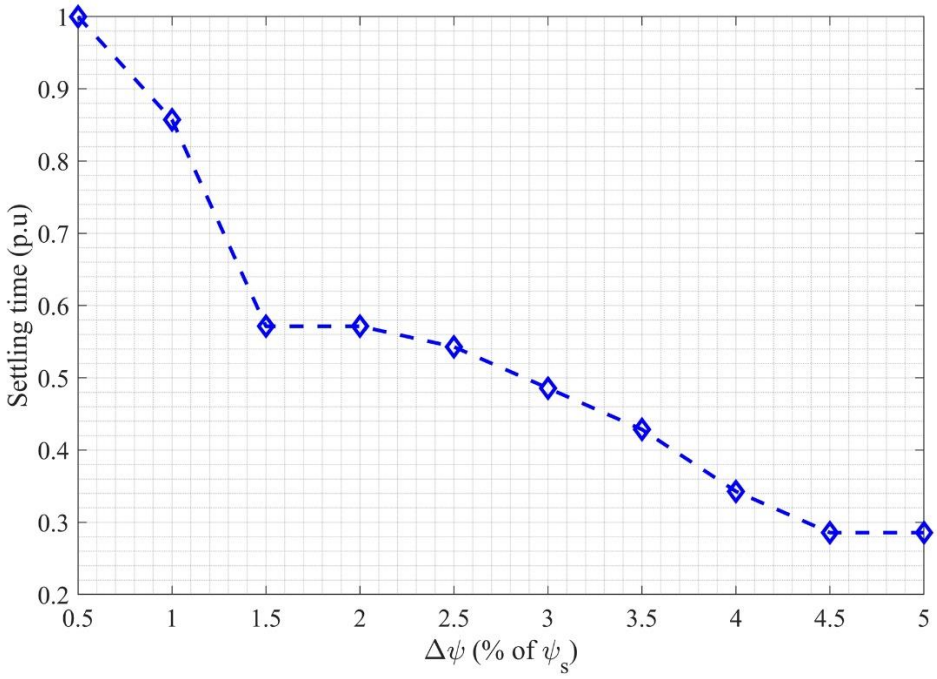

Figure 5.9: Settling time of the ESC algorithm vs. amplitude of the injected pulsating signal.

In this section, to find the optimal value of $\Delta\psi_s$, a cost function which is denoted as Z is proposed

$$Z = \lambda \times THD_{PU} + \mu \times \zeta_{PU} \tag{5.22}$$

where λ and μ are the weight factors. Z should be minimized by selecting the proper $\Delta\psi_s$. The data points for ζ (PU) and THD (PU) from Figure 5.9 and Figure 5.10 are considered and Z is computed based on (5.22). In this paper, both λ and μ are set to be 0.5, which means equal weights for the settling time and THD. The resulting optimal amplitude of the injected signal should be around 1% of the stator flux. Figure 5.11 shows the effect of the $\Delta\psi_s$, which is the amplitude of the injected HFS for the extremum seeking control algorithm. ESC is validated by simulating with different $\Delta\psi_s$ and showed in Figure 5.11.

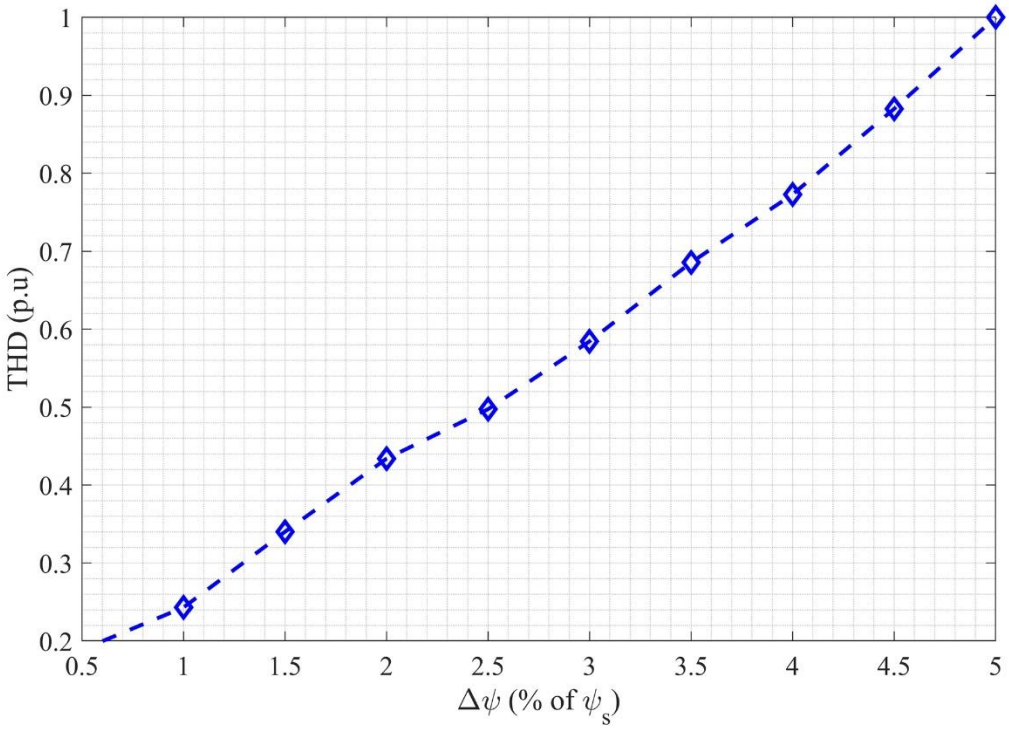

Figure 5.10: Stator currents THD vs. amplitude of the injected pulsating signal.

Based on the previous analysis, the design procedure of the ESC could be summarized as,

1. Selection of the injected high frequency signal $A\sin(\omega_c t)$, A should be small but having high enough signal to noise ratio;

2. Designing the HPF according to the frequency of the injected signal;
3. Designing the LPF and the cutoff frequency should be much lower than the frequency of the injected signal;
4. Determining the PI gains: k_i should satisfy $|k_i| < \left\| G_\psi \frac{G_h}{s} \right\|_\infty^{-1}$ and $k_p = \frac{k_i}{\alpha}$.

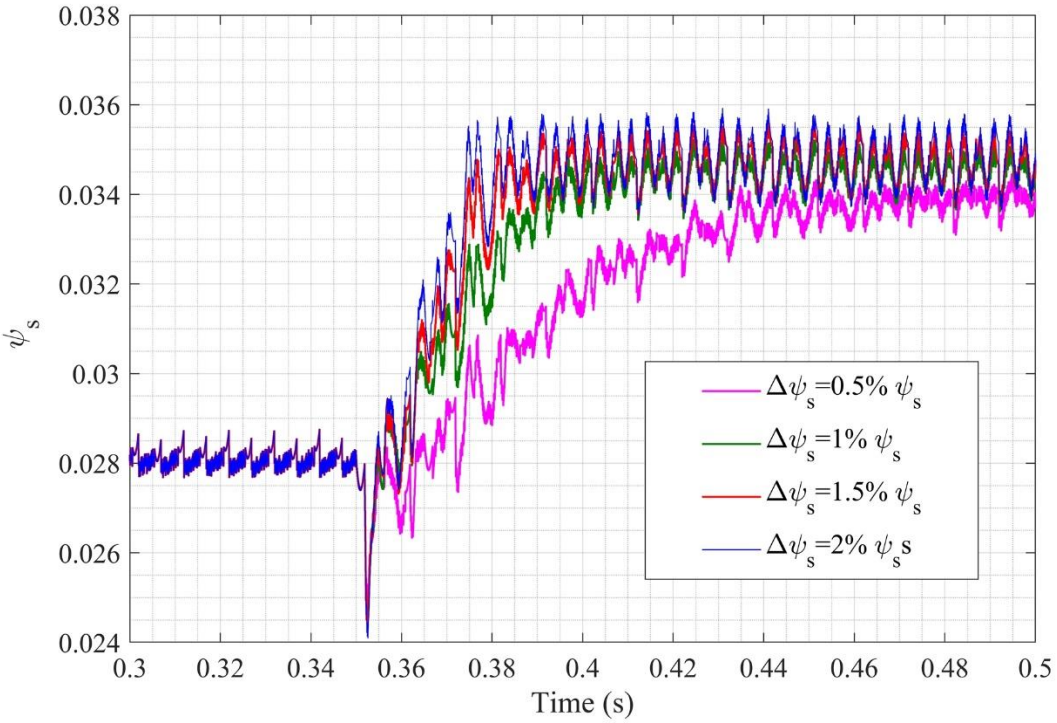

Figure 5.11: The effect of the minimum $\Delta\psi_s$.

5.6 Conclusions

The P & O [28] and the ESC [30] both signal injection based optimal reference flux searching approach are analyzed and discussed in this chapter. In the P&O, a fixed step size is adopted to find the optimal operating point. However, the fixed step size will lead to oscillation in the steady state if a large step size has been used, or slow transient response if a small step size is adopted. In contrast, an effective extremum seeking control algorithm is then introduced to determine the

optimal reference flux linkage online, leading to a MTPA-like approach for DTC of IPM motors. Stability analysis has been conducted to provide a guidance in the parameters design. The proposed method can significantly reduce the time consuming tuning effort and is robust to motor parameters variations. The searching step size of ESC is adaptive as the PI controller will automatically adjust the step size based on the searching error between ψ_{op}^{*} and ψ_{s}. In other words, the PI controller will generate a large step size when the searching error is large to fast the dynamic response and reduce the step size in the steady state to reduce the torque and flux ripples.

CHAPTER 6

ELECTRO-THERMAL CHARECTERIZATION PROCEDURE AND LOSS MODELING FOR SiC BASED INVERTER

6.1 Introduction

Due to the demand of high power density and increased switching frequency with low switching loss, the SiC device has superiority to the conventional Si power devices [105], [106] and [107]. In power converter application, the metal-oxide semiconductor field-effect transistor (MOSFET) and Schottky diode are the best options from the SiC power device family in the current state of the art. Depending on the applications, e.g., automotive, space where the volume and the space of the converter is crucial, higher switching frequency (>20 kHz) can help to reduce the size of the passive components such as filters (inductors and capacitors) [108]. Nevertheless, the switching loss will be higher with the implementation of the higher switching frequency. Therefore, analyze the selection of the proper switching frequency is essential for a particular operating condition.

Now, the switching loss minimization can be done in several ways such as reducing switching frequency which contradict the purpose of SiC adaptation. Another way to reduce the switching loss to reduce the gate resistances [25], [109], [110] and [111]. Conversely, this will lead to electromagnetic interface (EMI) and higher dv/dt, di/dt in the SiC power devices comparing to the Si devices [112]. The higher dv/dt at turn-on of the device can form crosstalk caused by the Miller capacitance [113]. The higher di/dt at turn-off of the device can form the voltage overshoot caused by the stray inductances. Therefore, the transient behavior needs to be optimized carefully to optimize the switching loss and make sue the EMI is within the acceptable limit. The conduction losses of the SiC devices is easy to understand. The drain-source resistance ($R_{ds\text{-}on}$) which is

dependent on the temperature and the drain source current (I_{ds}) can be used to calculate the conduction loss of the device. Additionally, the diode in the SiC device will also contribute to the conduction power loss which needs to be consider developing a detail loss model [114].

There are two popular los modeling methods for SiC power MOSFETS which are based on physical modeling and behavioral modeling [115]. In the physical model-based approach, the loss model is based on simulating the thermal behavior by solving the physical equation. This method is accurate, but the parameter has physical meanings, however, it is complex model, and the parameters are difficult to achieve. The other model mentioned as the behavioral model is based on mathematical fitting where generally the complex physical mechanisms of the device are not considered. Therefore, the behavioral model is flawed by inaccuracy [116], [117] and [118].

In Chapter 4 and Chapter 5, the novel control algorithm was proposed to enhance the efficiency and reduce the loss in the motor drive. However, to validate the claim, in this chapter an electro-thermal characterization procedure is developed and analyzed for SiC based inverter. A detail loss model is developed in this chapter considering both physical and behavioral model.

6.2 Proposed Electro-thermal Characterization Procedure

In this section a detail loss model is discussed based on the electro-thermal characterization procedure where first the datasheet-based procedure of the MOSFET device is shown and then the experiment-based model is proposed. For both cases, a XM3 a half-bridge power module, CAB450M12XM3 from Cree Wolfpseed is considered.

Figure 6.1 shows the half-bridge module, and the major parameters are shown in the appendix, Table A-2. The dimensions of the power module are 80 mm × 53 mm × 19 mm. It is a low inductance power module which is mentioned in the datasheet as 6.7 nH [119]. Therefore, can be applied to motor drive and traction drives [120].

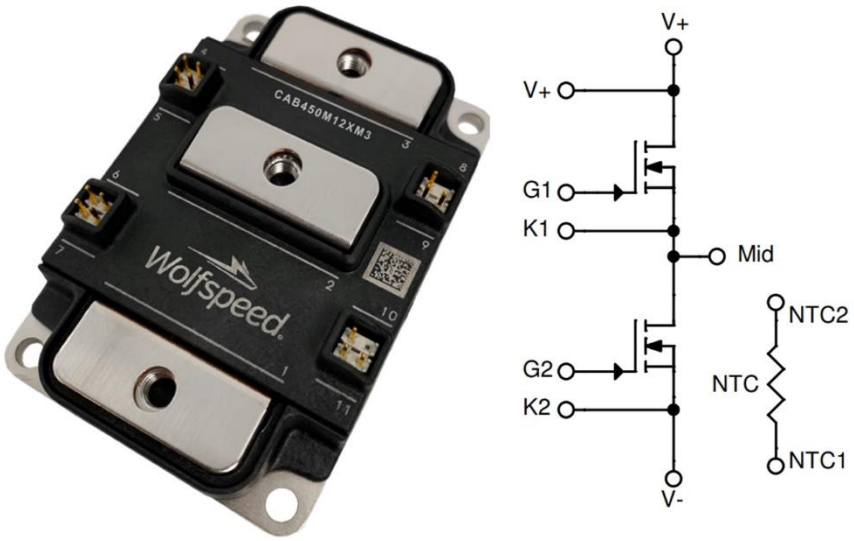

Figure 6.1: XM3 SiC MOSFET power module with half-bridge configuration.

6.2.1 Loss Model Generation from Curve-fitting

Semiconductor power losses can be classified into two categories such as static loss and dynamic loss. The static loss is defined as the conduction loss and the dynamic loss consists of turn -on and turn-off loss. Among them SiC MOSFET switching, and conduction loss has major contribution is power loss comparing the diode loss.

In this section, the curve fitting based loss model has been proposed where the thermal effect is also considered. Figure 6.2 shows the flow chart of the model where there are two major parts, power loss modeling and thermal modeling. Both are connected in a closed loop so that the model can demonstrate the realistic behavior of the actual system. The closed loop electro-thermal model starts with the dataset from the simulation which are V_{ds}, I_{ds}, junction temperature, T_j and the gate signal. From there the MOSFET and diode conduction loss is calculated based on the curve fitting mathematical equation and fed this information to the thermal model of the system. The thermal characteristic of the system is based on the power loss. Therefore, when the T_j is in steady state

then the power loss value should be taken into consideration since it takes couple of fundamental cycle for the T_j to go to steady state condition.

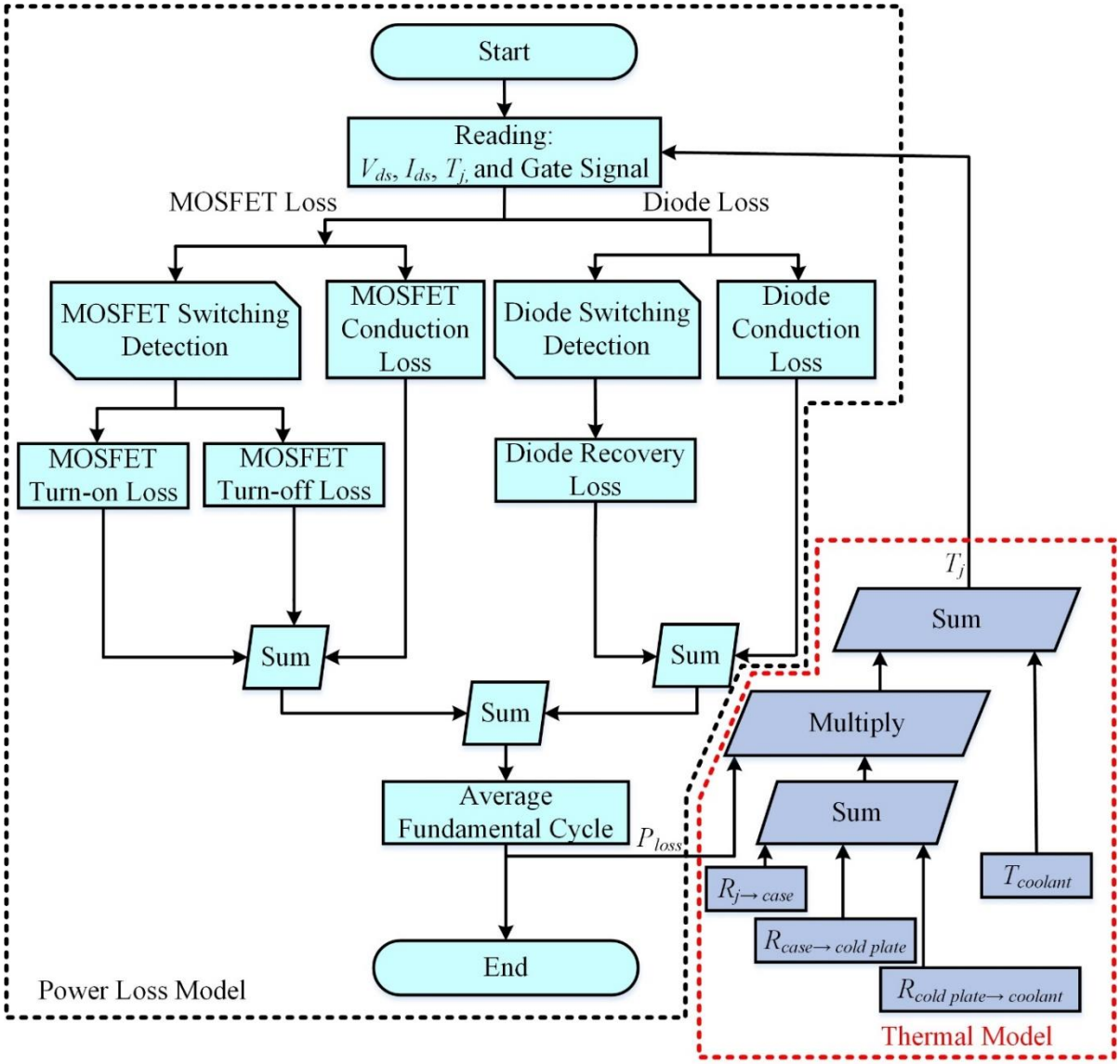

Figure 6.2: XM3 SiC MOSFET datasheet based electro-thermal model.

Figure 6.3 shows the loss model block diagram. The MOSFET and diode losses are the function of I_{ds}, T_j, switching frequency (f_{sw}), dead time (T_{dead}) and the external gate resistance (R_{gext}). The thermal mode is also a part of the loss model which includes coolant temp, $T_{coolant}$,

junction to case resistance, $R_{j\rightarrow case}$, case to cold plate temperature, $R_{case\rightarrow cold\ plate}$, and cold plate to liquid temperature, $R_{cold\ plate\rightarrow coolant}$.

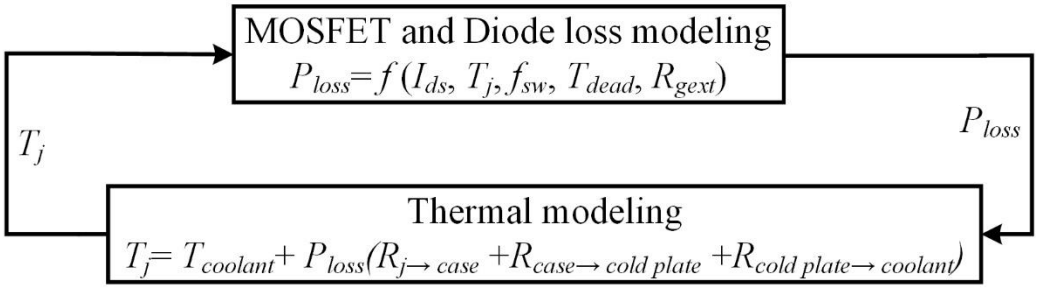

Figure 6.3: Loss model block diagram.

6.2.1.1 MOSFET Switching Loss

MOSFET switching loss calculation starts with the calculating the turn-on loss from the XM3 datasheet [120]. The curve fitting tool from the MATLAB/Simulink is used to regenerate the plot from the actual figure. The turn-on loss using the I_{ds} is calculated from (6.1). Figure 6.4 shows the comparison between the datasheet vs. curve-fitting results for E_{on} from I_{ds} for 800V DC bus.

$$E_{on}(mJ) = 0.01967 I_{ds}^{1.086} + 1.268 \tag{6.1}$$

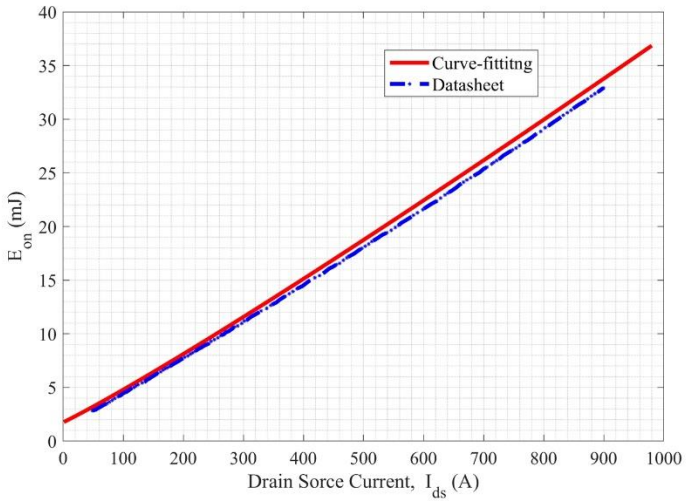

Figure 6.4: E_{on} vs. I_{ds} plot comparison between the curve-fitting and datasheet.

The turn-on energy of the switching device is also depending on the junction temperature. Because of the high non-linearity of the curve the E_{on} vs. T_j is divide into two parts and represented in per unit (p.u) form. Therefore, when the T_j is less than 85°C, the E_{on} equation can be denoted as,

$$E_{on}(p.u) = 1.249 \times 10^{-5} T_j^2 - 0.001493 T_j + 1.032 \tag{6.2}$$

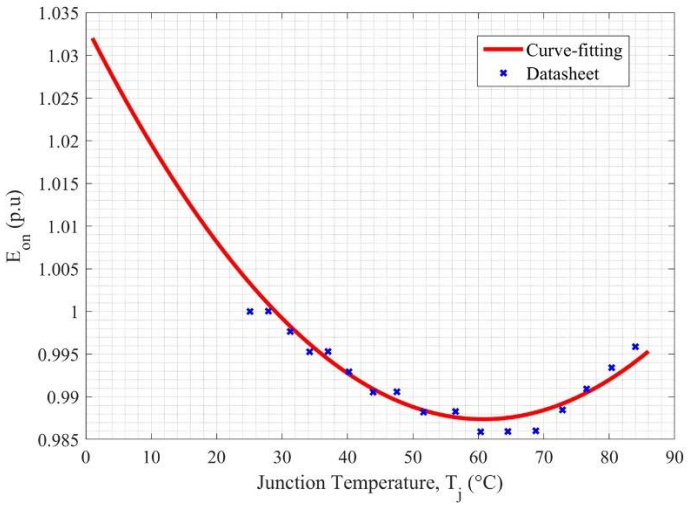

Figure 6.5: E_{on} (p.u) vs. T_j plot comparison between the curve-fitting and datasheet when T_j<85°C.

Figure 6.5 shows the comparison between the datasheet vs. curve-fitting results for E_{on} from T_j when the T_j<85ºC. Now, when the T_j is greater than 85°C, the E_{on} equation can be achieved from curve -fitting as shown in (6.3). Figure 6.6 shows the comparison between the datasheet vs. curve-fitting results for E_{on} from T_j when the T_j>85ºC.

$$E_{on}(p.u) = 1.952 \times 10^{-5} T_j^{1.833} + 1.833 \tag{6.3}$$

The turn-on energy is also dependent on the external gate resistance of the power device which is also considered in this loss model. The E_{on} vs. R_{gext} is also measured in p.u in this method since the values provided in datasheet is not for the operating condition considered here.

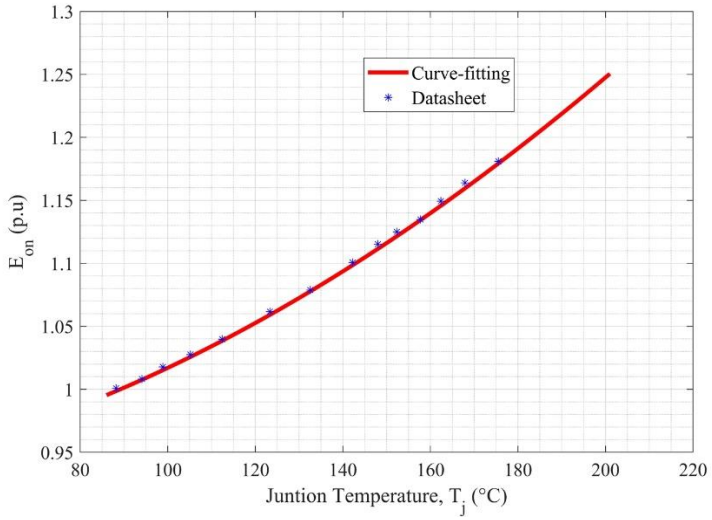

Figure 6.6: E_{on} (p.u) vs. T_j plot comparison between the curve-fitting and datasheet where T_j>85°C.

The R_{gext} vs. E_{on} relation is shown in the Equation (6.4) and compared with the datasheet value is shown in the Figure 6.7.

$$E_{on}(p.u) = 0.2762R_{gext} + 0.9915 \tag{6.4}$$

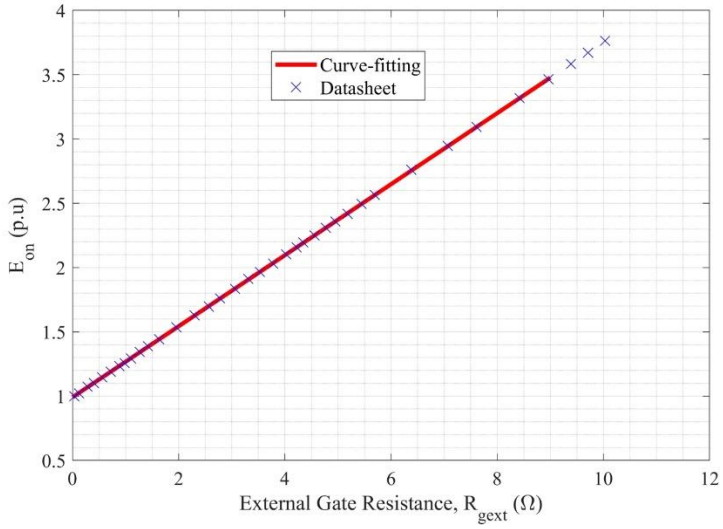

Figure 6.7: E_{on} (p.u) vs. R_{gext} plot comparison between the curve-fitting and datasheet.

The total turn-on energy can be shown as Figure 6.8 below,

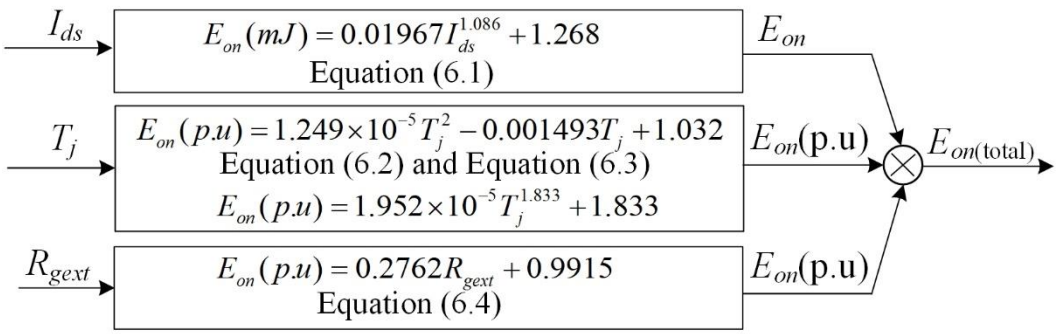

Figure 6.8: Total E_{on} block diagram.

The turn-off energy E_{off} calculation is similar to the E_{on} calculation. The E_{off} is also a function of I_{ds}, T_j and R_{gext}. The turn-ff loss using the I_{ds} is calculated from (6.5). Figure 6.9 shows the comparison between the datasheet vs. curve-fitting results for E_{off} from I_{ds} for 800V DC bus.

$$E_{off}(mJ) = 1.65\times10^{-5} I_{ds}^2 + 0.02708 I_{ds} - 1.245 \tag{6.5}$$

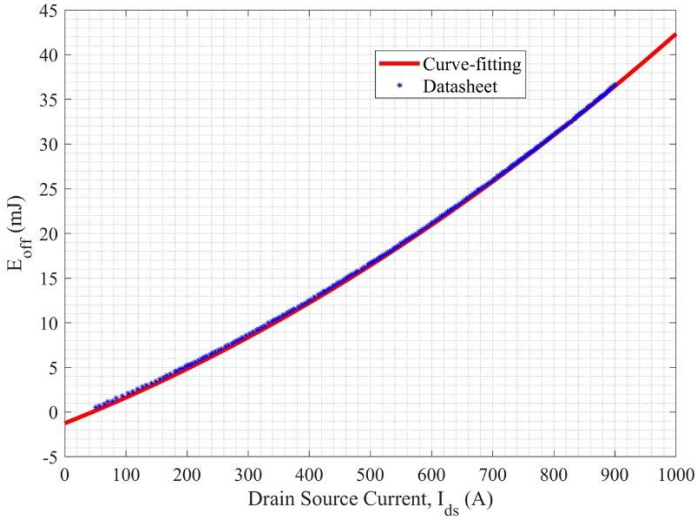

Figure 6.9: E_{off} vs. I_{ds} plot comparison between the curve-fitting and datasheet.

The relationship between E_{off} and the T_j is shown in Equation (6.6) in p.u form. And the Figure 6.10 shows the comparison between the E_{off} and T_j in graphical form.

$$E_{off}(p.u) = 10.0003095 T_j^{1.273} + 0.9796 \tag{6.6}$$

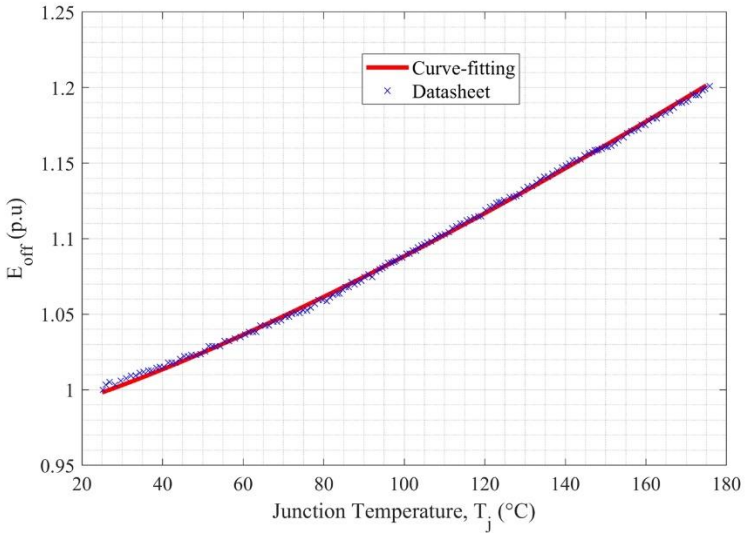

Figure 6.10: E_{off} (p.u) vs. T_j plot comparison between the curve-fitting and datasheet.

The relationship between E_{off} and the R_{gext} is shown in Equation (6.7) in p.u form. And the Figure 6.11 shows the comparison between the E_{off} and R_{gext} in graphical form.

$$E_{off}\,(p.u) = 0.2608R_{gext} + 0.9919 \tag{6.7}$$

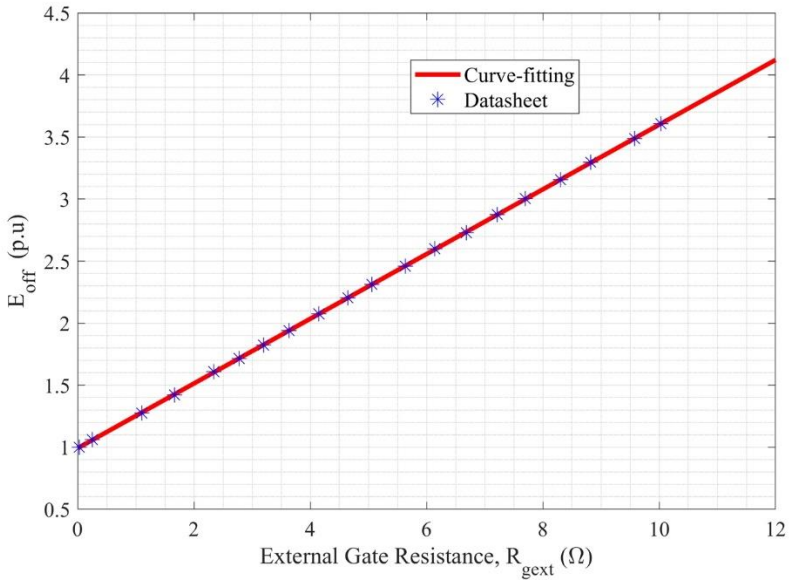

Figure 6.11: E_{off} (p.u) vs. R_{gext} plot comparison between the curve-fitting and datasheet.

The total turn-off energy can be expressed as a block diagram as shown in Figure 6.12 below,

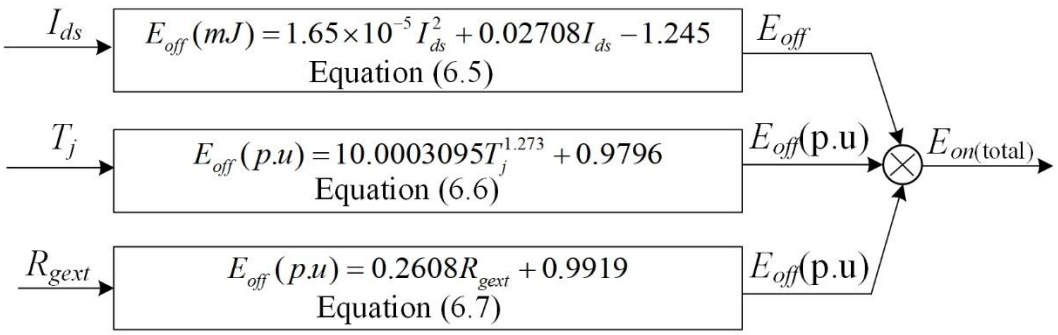

Figure 6.12: Total E_{off} block diagram.

After calculating the total E_{on} and E_{off} for MOSFET, it is multiplied by the switching period by detecting switching transition in the simulation. Thus, the switching loss for the MOSFET can be achieved from the simulation.

6.2.1.2 MOSFET Conduction Loss

The MOSFET conduction loss is calculated using the curve-fitting equations. The drain source on state resistance $R_{ds\text{-}on}$ is calculated for different T_j and for different drain to source current, I_{ds}. Then the calculated p.u value for $R_{ds\text{-}on}$ is multiplied with the typical $R_{ds\text{-}on}$ value of the XM3 half-bridge module. The typica value of the $R_{ds\text{-}on}$ is selected for the calculation and loss modeling is 4 mΩ.

First, $R_{ds\text{-}on}$ can be expressed using curve-fitting for different T_j as Equation (6.8) and comparison between curve-fitting of the $R_{ds\text{-}on}$ and the datasheet values is shown in Figure 6.13. From the Figure 6.13, it is clear that the extracted values from the datasheet and the values from the curve-fitting Equation (6.8) are very close to each other. Therefore, the loss model made from these curve-fitting equations would be accurate.

$$R_{ds-on}(p.u) = -5.894\times10^{-10} T_j^4 + 1.258\times10^{-10} T_j^3 + 2.665\times10^{-10} T_j^2 - 0.0008914 T_j + 1 \quad (6.8)$$

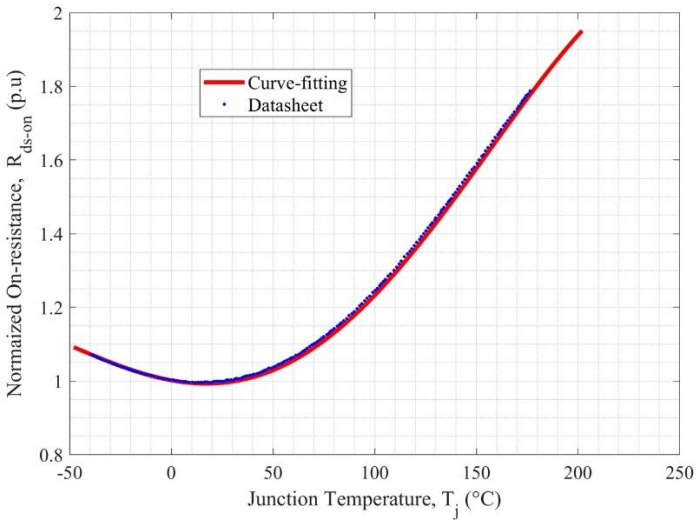

Figure 6.13: $R_{ds\text{-}on}$ (p.u) vs. T_j plot comparison between the curve-fitting and datasheet.

Now the $R_{ds\text{-}on}$ (p.u) at 25ºC is calculated by varying the I_{ds} and is shown in Equation 6.9. The Figure 6.14 shows the curve fitting equation matched with the datasheet values.

$$R_{ds-on}(p.u) = 3.277 \times 10^{-5} I_{ds}^{1.204} + 0.9454 \tag{6.9}$$

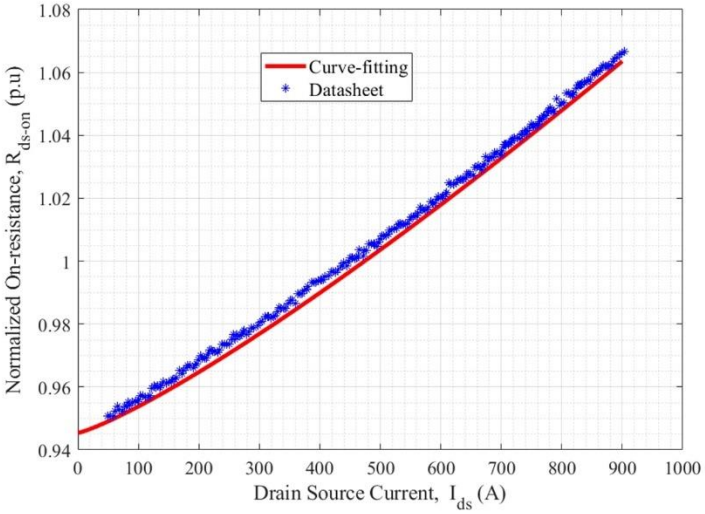

Figure 6.14: $R_{ds\text{-}on}$ (p.u) vs. I_{ds} plot comparison between the curve-fitting and datasheet.

The block diagram of the $R_{ds\text{-}on}$ can be shown in Figure 6.15 where, the typical $R_{ds\text{-}on}$ value is multiplied with the two other $R_{ds\text{-}on}$ (p.u) value from curve-fitting. Then the total conduction loss is calculated by squaring the I_{ds} and multiplied with the total $R_{ds\text{-}on}$.

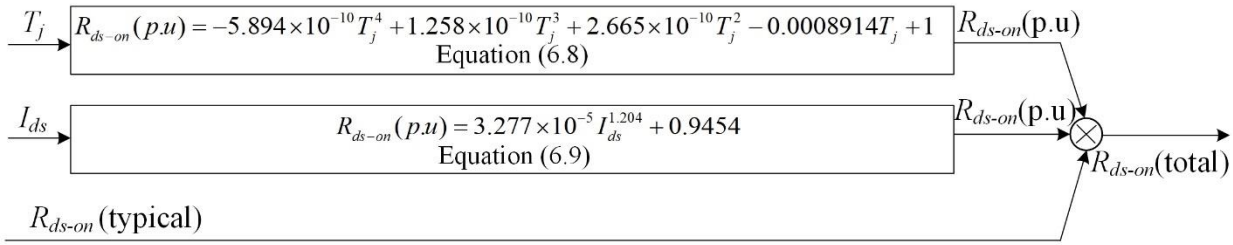

Figure 6.15: Total $R_{ds\text{-}on}$ block diagram.

6.2.1.3 Diode Switching Loss

The Diode switching loss also has contribution to the total power loss of the system. In this section the diode switching loss calculation is shown using the curve-fitting and also compared with the datasheet curves. At first the diode reverse recovery energy, E_{rr} is calculated for different T_j at 800V from the Equation 6.10 and then compared this with the datasheet in Figure 6.16.

$$E_{rr} = -2.078\times10^{-9}T_j^4 + 7.28\times10^{-7}T_j^3 - 2.381\times10^{-10}T_j^2 + 0.005253T_j + 0.1254 \qquad (6.10)$$

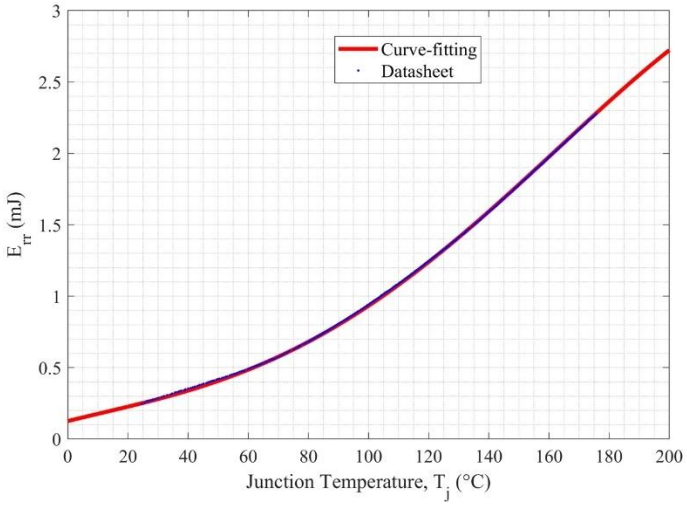

Figure 6.16: Diode reverse recovery energy, E_{rr} vs. T_j.

The E_{rr} is also a function of external gate resistance. Therefore, the E_{rr} (p.u) is calculated based on the R_{gext} value and show in Equation (6.11). The Figure 6.17 shows the E_{rr} (p.u) vs. R_{gext}. Then the

total diode reverse recovery loss, E_{rr} (total) is calculated as shown in the block diagram below in Figure 6.18.

$$E_{rr}(p.u) = -0.0007371R_{gext}^3 + 0.02261R_{gext}^2 - 0.244R_{gext} + 1.238 \quad (6.11)$$

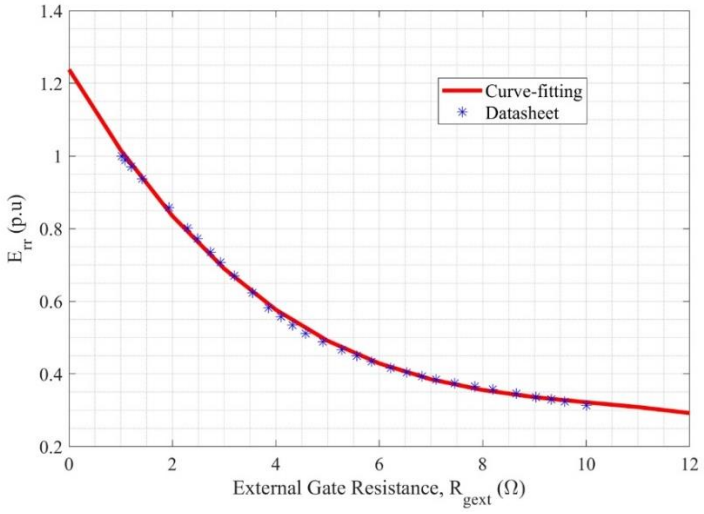

Figure 6.17: Diode reverse recovery energy, E_{rr} (p.u) vs. R_{gext}.

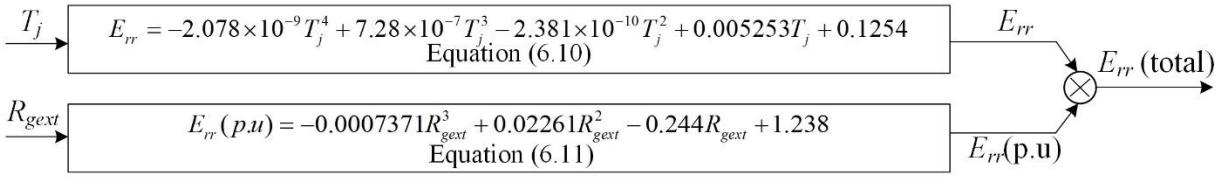

Figure 6.18: Total E_{rr} block diagram.

6.2.1.4 Diode Conduction Loss

The diode conduction loss occurs in between switching transition of two active switching MOSFET which is known as the dead time. In this section the calculation of the diode conduction loss is shown for different junction temperature.

The Equation (6.12) shows the curve-fitting equation for calculating the source drain voltage, V_{sd} across the diode. These voltages are used to calculate the diode conduction loss during dead time as shown in Figure 6.19.

$$
\begin{aligned}
V_{sd} &= 0.1842 I_{ds}^{0.4172} + 2.432 @ 25^{\circ} C \\
V_{sd} &= 0.171 I_{ds}^{0.4098} + 2.281 @ 100^{\circ} C \\
V_{sd} &= 0.1632 I_{ds}^{0.4122} + 2.24 @ 125^{\circ} C \\
V_{sd} &= 0.1559 I_{ds}^{0.4154} + 2.201 @ 150^{\circ} C \\
V_{sd} &= 0.1375 I_{ds}^{0.4287} + 2.198 @ 175^{\circ} C
\end{aligned}
\tag{6.12}
$$

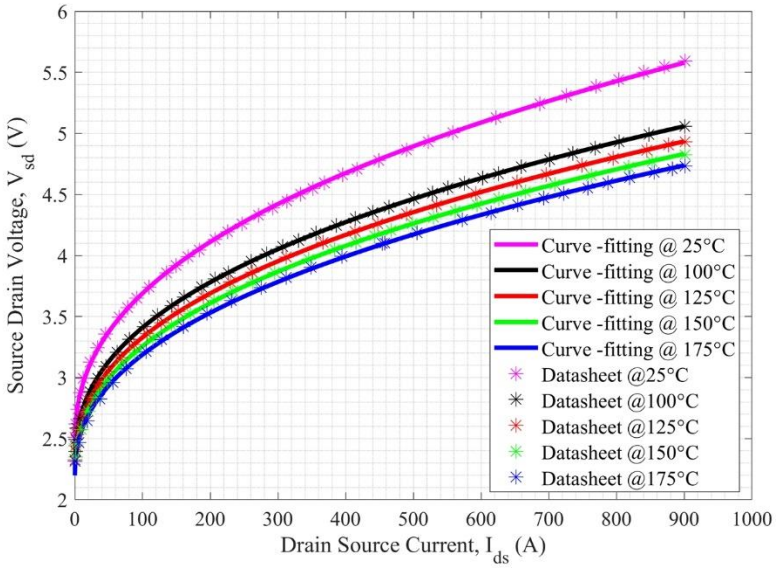

Figure 6.19: I_{ds} vs. V_{sd} comparison between curve-fitting and datasheet.

6.2.1.5 Thermal Impledance Network

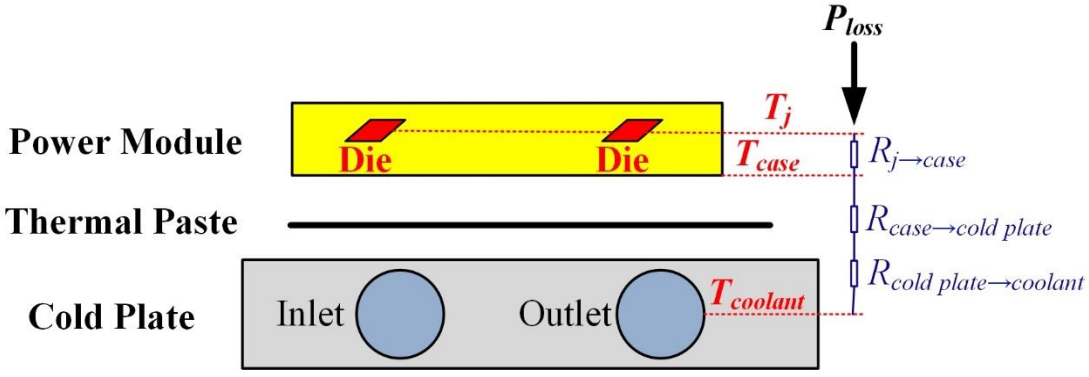

Figure 6.20: Equivalent thermal model where the module is mounted on a cold plate.

A thermal impedance network is modeled from the MOSFET junction to the coolant liquid in the cold plate as shown in Figure 6.20. The total power loss is flowing through a series total

impedance network from the junction to liquid coolant can be denoted as $R_{j\rightarrow coolant}$ and shown in analytical form as,

$$R_{j\rightarrow coolant} = \frac{T_j - T_{coolant}}{P_{loss}} \tag{6.13}$$

Based on Equation (6.13), it is possible to simply calculate the maximum possible power transfer achievable from the module junction to the liquid using a simplified thermal impedance modeled shown in Figure 6.20.

6.3 Results from the Proposed Electrothermal Characterization model

For validating the proposed electro-thermal model for SiC-based converter, in this section a MATLAB/Simulink based simulation model is developed and used. The working characteristics of the device in the saturation region is also considered. And to further validation the result from the proposed loss model is compared with a reference inverter design using XM3 power module in [119].

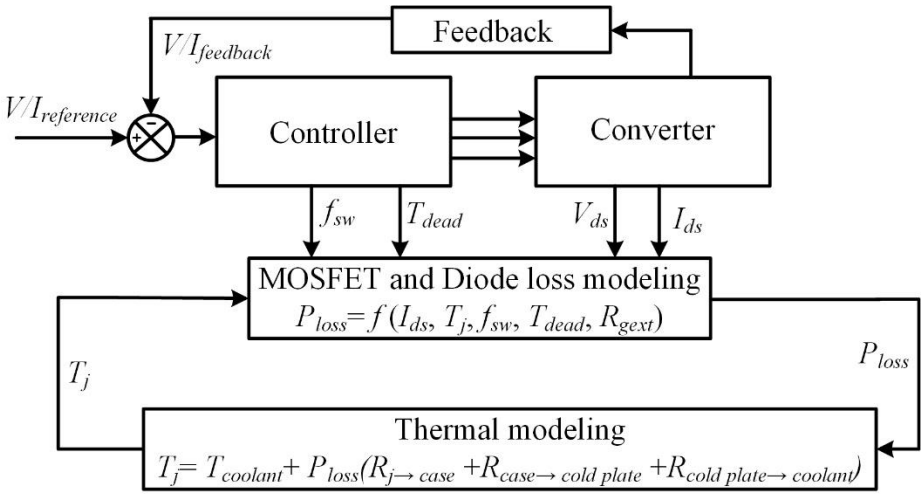

Figure 6.21: Simple block diagram for the Simulink based loss model.

Figure 6.21 represents the simple block diagram of the MATLAB/Simulink-based loss model where the information from all the curve-fitting polynomial equations is used and the information

from the system is adopted. Two operating conditions are considered, 200kW power and 300kW power. At 200kW power level, the parameters that considered are shown in Table A-3 in Appendix. For 200kW power level there are two modes of operation with SVPWM control strategy, high current (I_{peak} = 450A) when the modulation index (MI) is 0.64 and high voltage (V_{peak} = 760) when the MI is 0.95. First the simulation is done in high current mode.

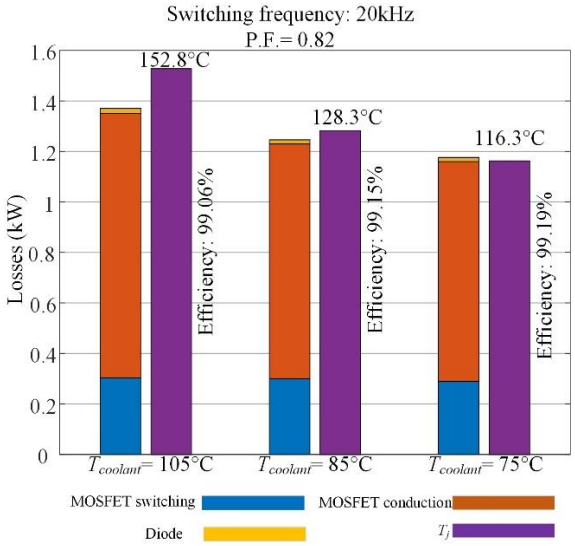

Figure 6.22: Power loss when I_{peak} = 450A and f_{sw} = 20 kHz.

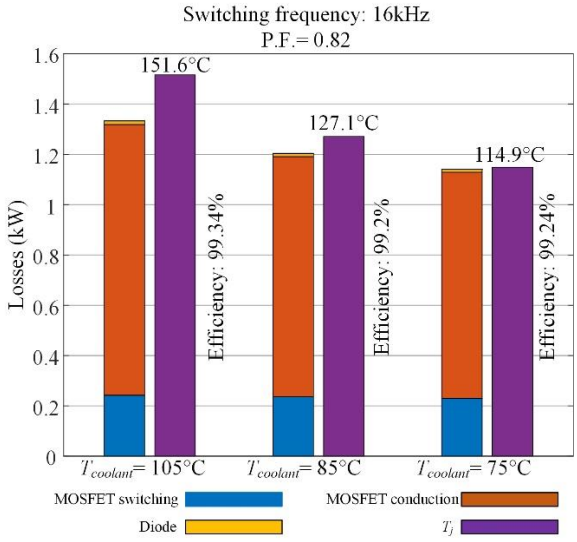

Figure 6.23: Power loss when I_{peak} = 450A and f_{sw} = 16 kHz.

Figure 6.22 shows the power loss of a two-level inverter consisting three XM3 half-bridge module when the switching frequency is 20 kHz. Three simulation were done with three different coolant temperature as $T_{coolant}$ = 105°C, $T_{coolant}$ = 85°C, and $T_{coolant}$ = 75°C. For all the case in Figure 6.22, the MOSFET conduction loss is dominating. The efficiency is also presented in the bar graph. Figure 6.23 is also showing bar graph of the losses and the junction temperature with 16 kHz f_{sw}. In this figure the MOSFET conduction loss is also dominating, and the next biggest source of losses are coming from the MOSFET switching.

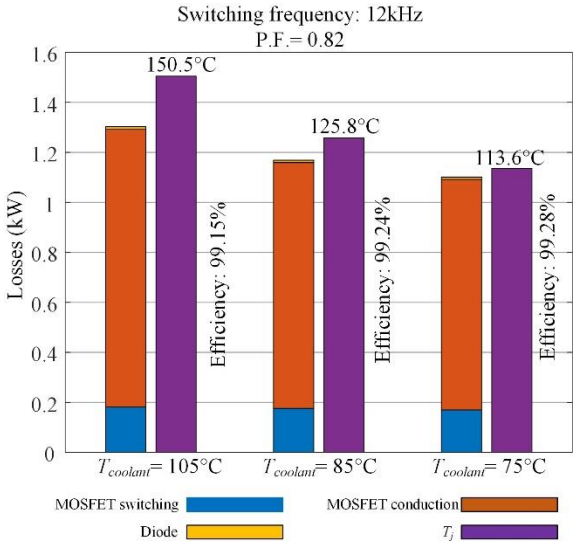

Figure 6.24: Power loss when I_{peak} = 450A and f_{sw} = 12 kHz.

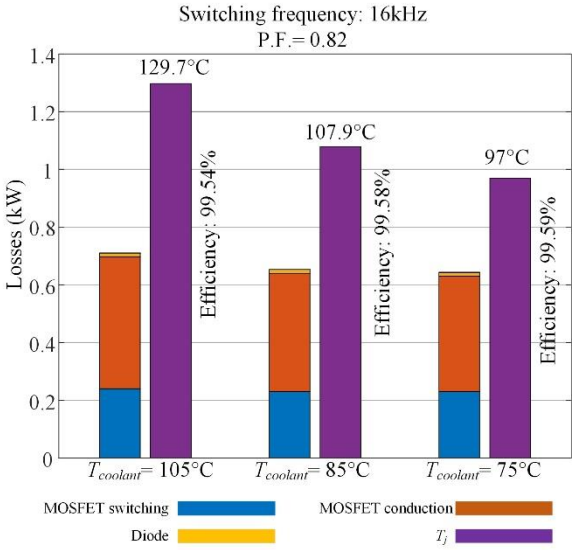

Figure 6.26: Power loss when V_{peak} = 760V and f_{sw} = 16 kHz.

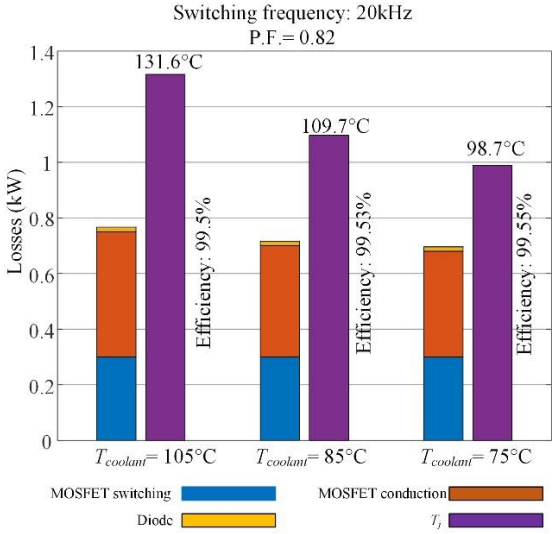

Figure 6.25: Power loss when V_{peak} = 760V and f_{sw} = 20 kHz.

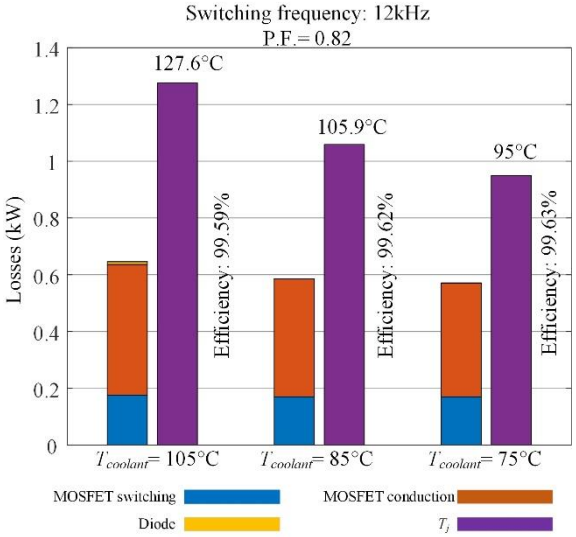

Figure 6.27: Power loss when V_{peak} = 760V and f_{sw} = 12 kHz.

The simulation result in high current mode with 12 kHz switching frequency is shown in Figure 6.24. Then from Figure 6.25 to Figure 6.27, the high voltage mode results are shown with 20 kHz, 16 kHz, and 12 kHz respectively. In all the loss data figures, it is clear that with lowest coolant temperature, the loss will reduce, and the efficiency will increase simultaneously which is obvious.

Next, the second operating condition were consider where the loss model was simulated for 300 kW power with exactly same parameters as the Cree 300 kW inverter in [119] to further validate the accuracy of the proposed loss model. The frequency levels were 20 kHz, 15 kHz, and 10 kHz. Other fundamental parameters were listed in Table A-4 in Appendix.

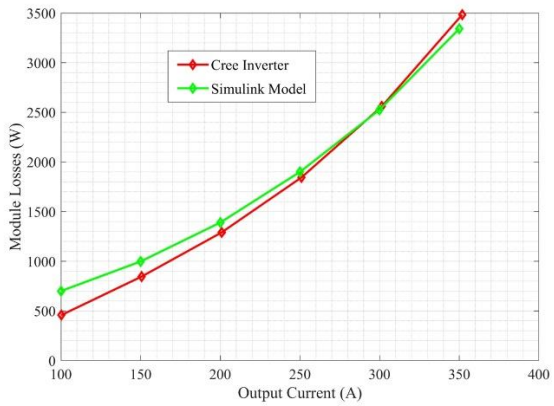

Figure 6.28: Loss comparison between Cree inverter and loss model at 20 kHz.

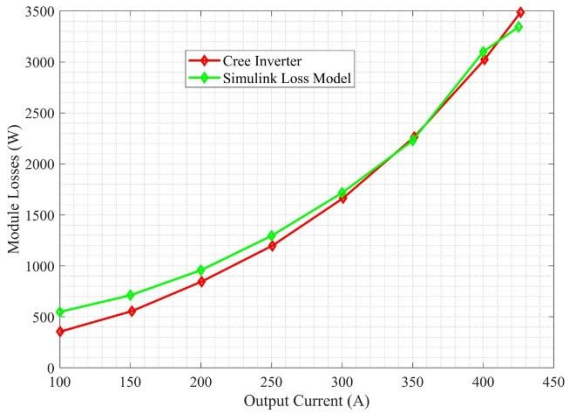

Figure 6.30: Loss comparison between Cree inverter and loss model at 10 kHz.

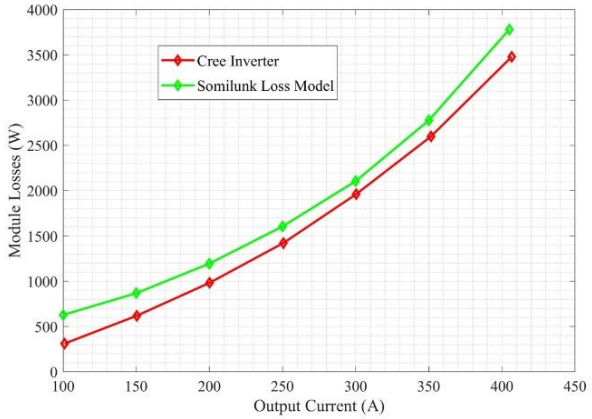

Figure 6.29: Loss comparison between Cree inverter and loss model at 15 kHz.

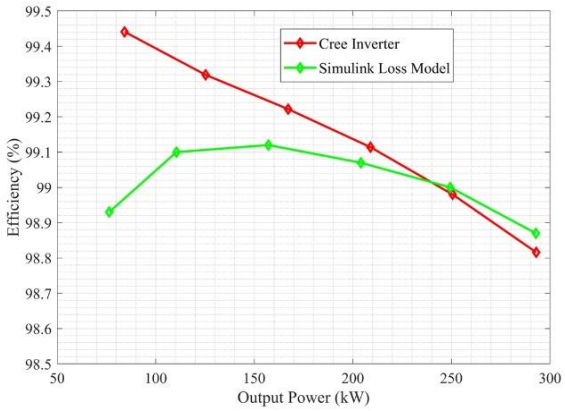

Figure 6.31: Efficiency comparison between Cree inverter and loss model at 20 kHz.

From Figure 6.28 to Figure 6.30 show the module loss comparison between the commercially available Cree 300 kW inverter and the proposed loss model with same parameters. And from Figure 6.31 to Figure 6.33, the output power vs. efficiency plot is shown for both Cree inverter

and proposed loss model. In output power vs. efficiency comparison section, green line in all the figures indicates the Simulink loss model. From those figures it can be observed that the Simulink loss model results show higher power losses than the Cree data. The error in grabbing the data and curve fitting is the reason behind it. In the low junction temp. (T_j<85°C) region, the MOSFET turn-on loss is not linear with respect to T_j and the fitting curve shows higher approximation error. In the high output power/high junction temp. region, all the simulation results are close to the Cree data.

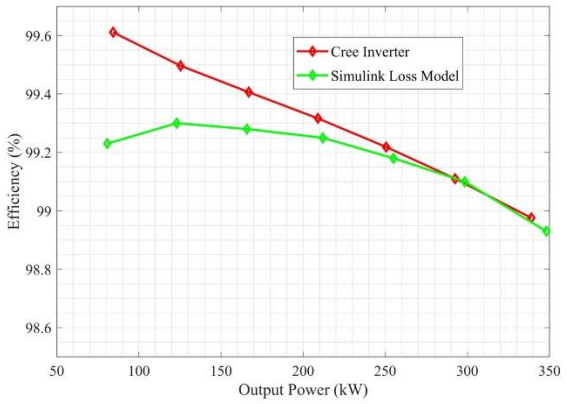

Figure 6.32: Efficiency comparison between Cree inverter and loss model at 15 kHz.

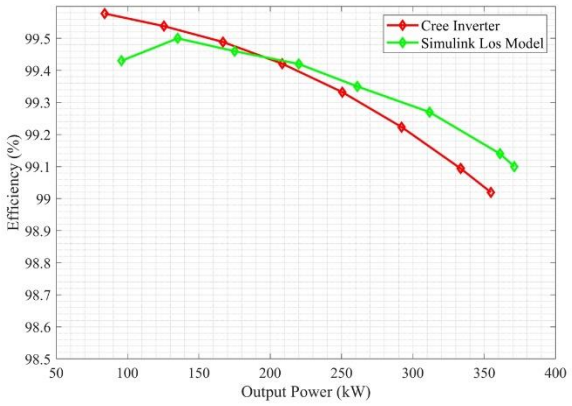

Figure 6.33: Efficiency comparison between Cree inverter and loss model at 10 kHz.

6.4 Conclusions

To summarize the above loss modeling, it is clear from the figure presented in this chapter that in all the cases the conduction loss has the dominating contribution in the overall loss in the system. Therefore, it is important to minimize the conduction loss in order to enhance the efficiency. The ESC and the advanced DTC presented in chapter 5 and chapter 4 respectively, offer the way of minimizing the losses so that the efficiency can be increased. These are the reason to understand the losses of the system carefully and study it thoroughly. In this chapter the Simulink based loss

model is developed and the polynomial equations are developed based on curve-fitting for the MOSFET and/or Diode conduction and switching losses.

CHAPTER 7

SIMULATION AND EXPERIMENTAL SETUP

All the simulation studies and results conducted in this dissertation are done in MATLAB/Simulink platform and corresponding experimental studies are also presented to validate the effectiveness of the proposed and conventional methods. There are three Simulink models, (1) a Simulink model to validate the proposed advanced DTC for T-type NPC-fed IPM motor, (2) a Simulink model to validate the proposed P & O for searching the optimal flux for the DTC, and (3) a Simulink model to validate the proposed ESC for searching the optimal flux for the DTC. Additionally, there are two test setups for experimental validation which are (1) a 200 W IPMSM test stand with a three-level inverter for advanced DTC approach, and (2) a 200 W IPMSM test stand with a two-level inverter for optimal flux searching algorithm.

7.1 Simulation Model for Advanced Direct Torque Control for IPMSM

The simulation model of the advanced direct torque control for an IPMSM is shown in the Figure 7.1. The machine parameters were measured and presented in Table A-1 in Appendix section. The initial rotor position was also measured to find the offset between the encoder/resolver position and the actual rotor position. This is a direct torque control approach, therefore, the IPM motor is operated by directly commanding the torque reference. Based on the torque and flux hysteresis command the proposer voltage vector is selected depending on the sector of operation. The other elements in the overall control system of the DTC are, park transformation, torque, flux, and sector estimation, and a T-type NPC three-level inverter. There is also a modulator in the system to generate the gate signal from the proposed voltage vectors which is shown in the Figure 7.1.

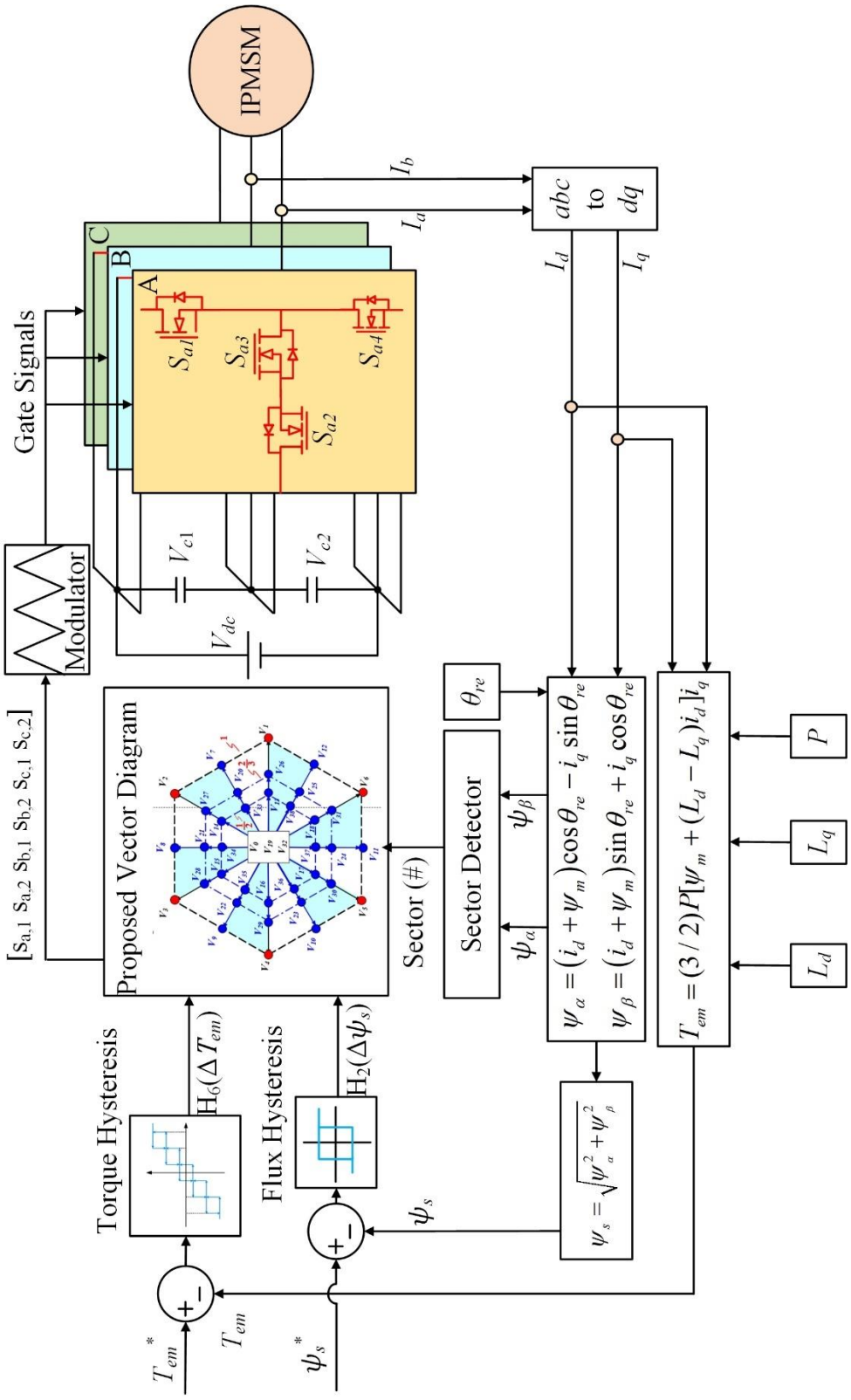

Figure 7.1: Block diagram of the simulation model of the proposed DTC with T-type NPC inverter.

7.2 Simulation Model for the Proposed Perturb and Observe (P & O)

The simulation model of the proposed perturb and observe method for optimal flux searching for an IPMSM is shown in the Figure 7.2. The machine parameters were measured and presented in Table A-1 in Appendix section. The initial rotor position was also measured to find the offset between the encoder/resolver position and the actual rotor position. This is a signal injection based optimal flux searching approach, therefore, in this method a small value of the flux is injected into the system and based on the response from the stator current magnitude the MTPA point is obtained. In the P & O a low pass filter is used to eliminate the high frequency components. The key point in here is to find the position of the current operating state.

7.3 Simulation Model for the Proposed ESC

The simulation model of the ESC method for optimal flux searching for an IPMSM is shown in the Figure 7.3. The machine parameters were measured and presented in Table A-1 in Appendix section. The initial rotor position was also measured to find the offset between the encoder/resolver position and the actual rotor position. This is a high frequency signal injection based optimal flux searching approach, therefore, in this method a small value of the flux with a high frequency is injected into the system and based on the response from the stator current magnitude the MTPA point is obtained. In the ESC a high-pass filter is used first to get the high frequency term from the stator current and then a low-pass filter is used to obtain the DC component which holds the information of the MTPA point. There are some other elements in the ESC system, i.e., demodulation, PI controller and high frequency signal itself.

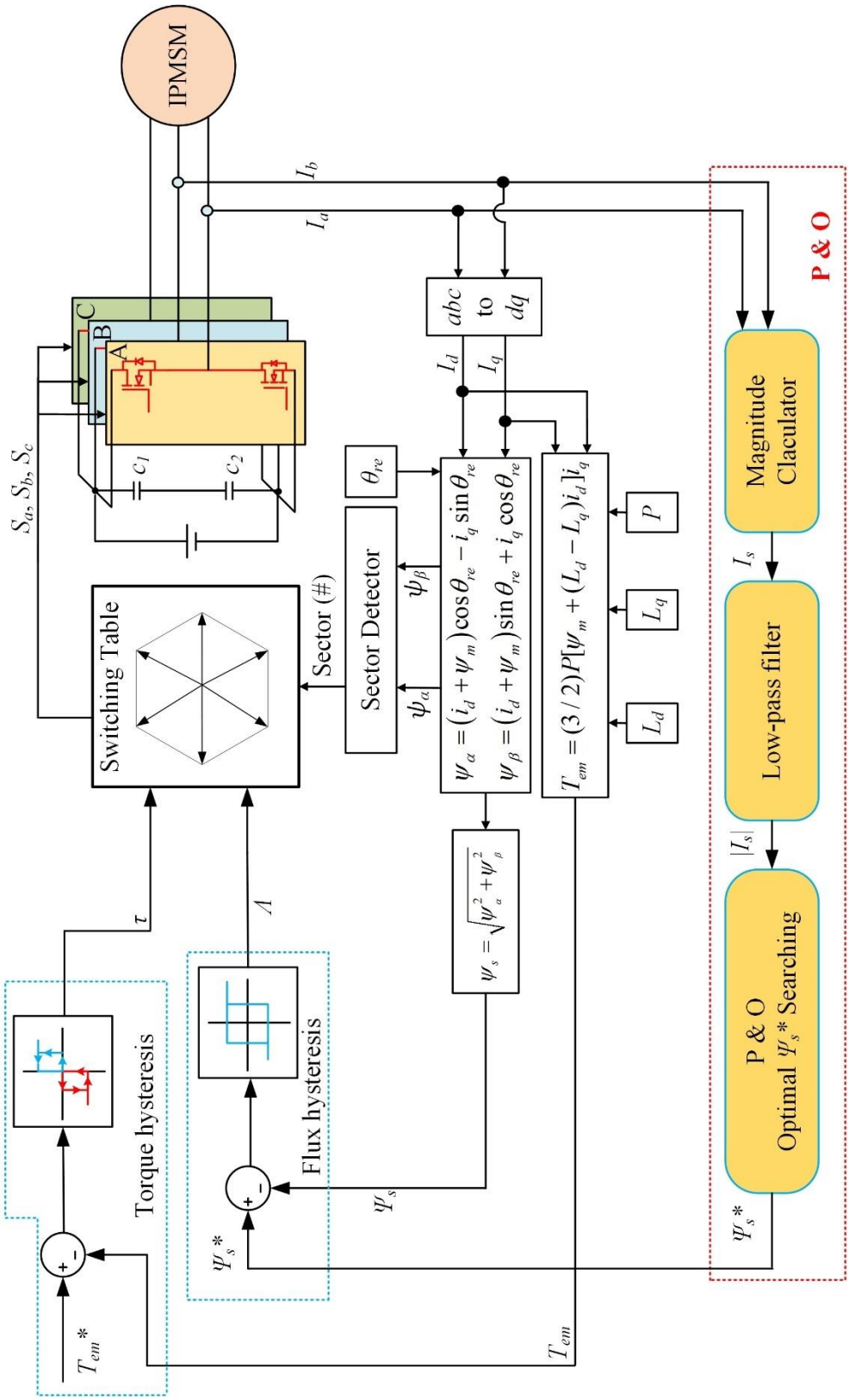

Figure 7.2: Block diagram of the simulation model of the DTC control IPM with the proposed P & O.

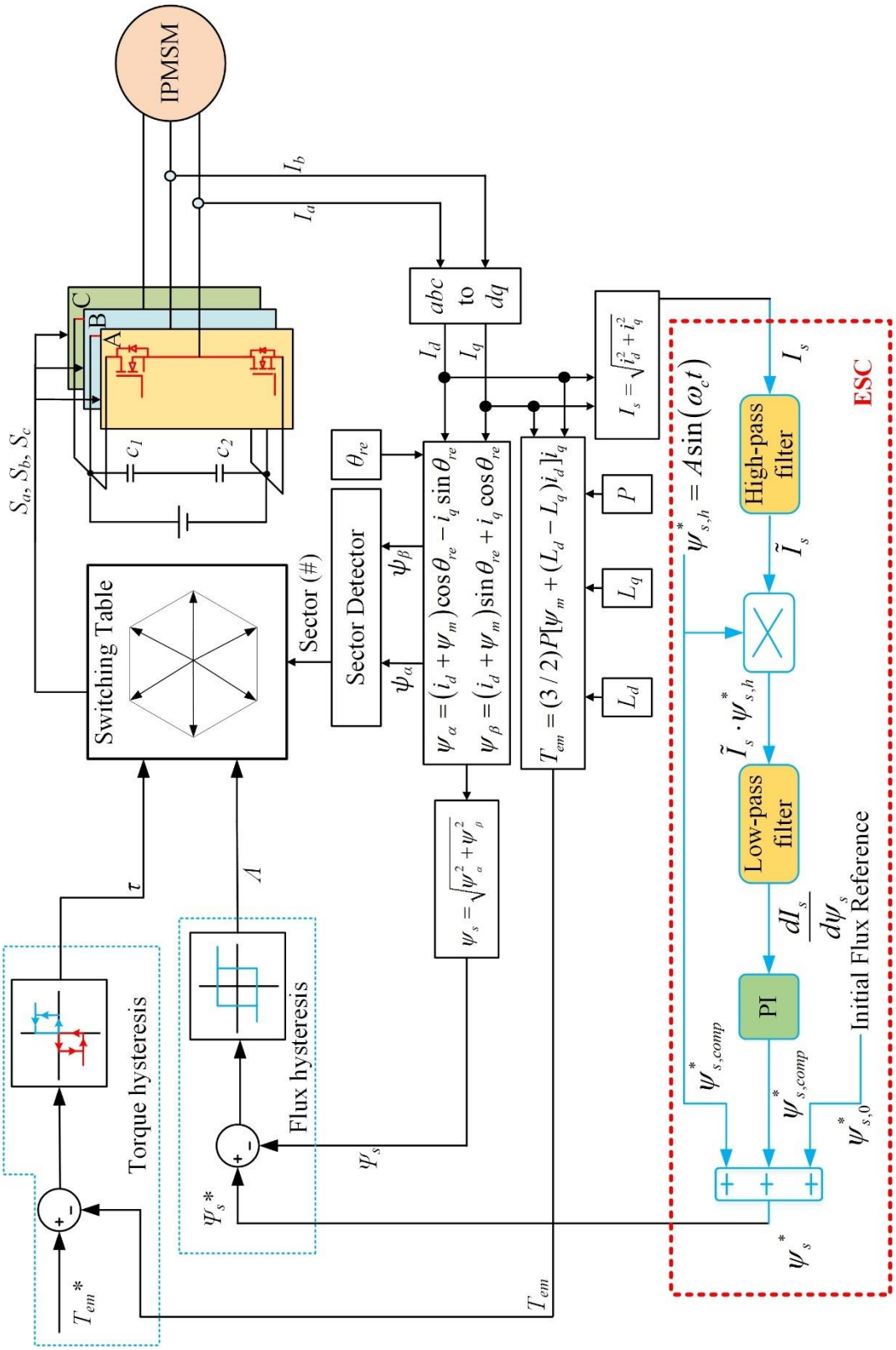

Figure 7.3: Block diagram of the simulation model of the DTC control IPM with the proposed ESC.

7.4 Test Setup for the Proposed Advanced Direct Torque Control

To further validate the effectiveness of the proposed advanced DTC experimental studies were performed. The experiment was carried out on the prototype of an all SiC three-level T-type inverter. The 3-L T-type VSC was designed in the lab using discrete SiC MOSFETs from CREE (C2M0160120D) [121]. A 250 W IPM motor was used in the experiment with major parameters shown in Table A-1 in the appendix section. The overall DTC algorithm is implemented on MicrolabBox dSPACE real time control system. The overall experimental setup is shown in Figure 7.4, which consists of an IPM motor controlled by a 3-L T-type inverter, and a DC motor is controlled by a H-bridge converter. The DC motor can work as either a prime mover to maintain constant speed on the IPM motor or a load machine. Both motors share the same DC bus. The DC bus voltage was maintained 42 V by a DC power supply which is also shown in the Figure. The sampling frequency of the DTC is 50 kHz at variable motor shaft speed.

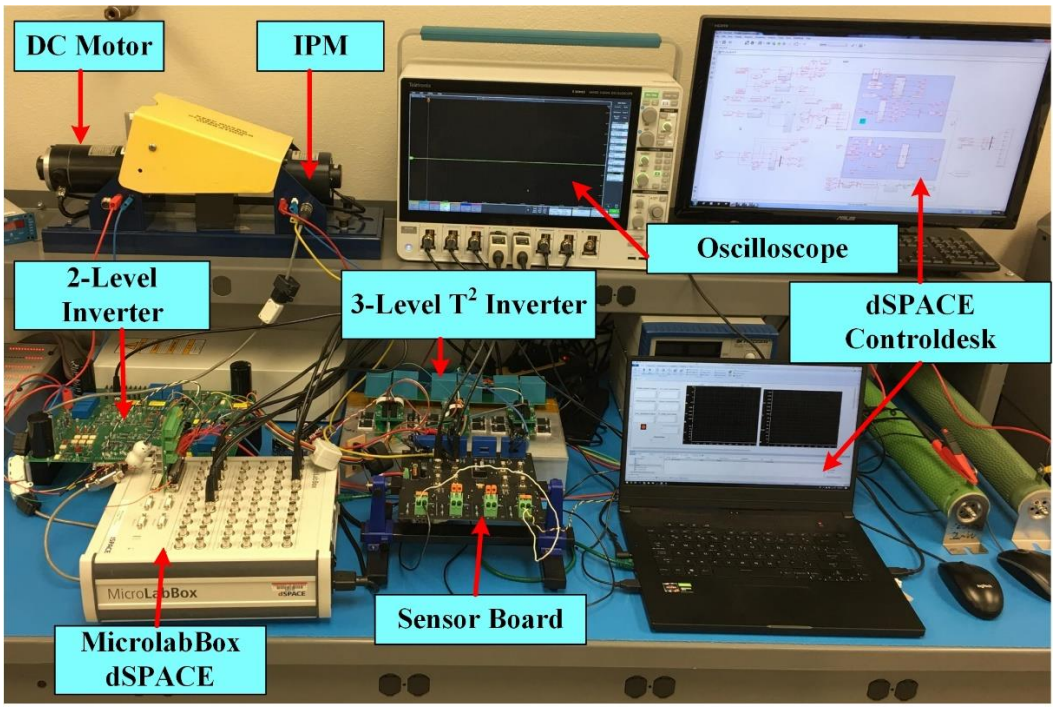

Figure 7.4: Experimental setup for advanced direct torque control.

7.5 Test Setup for the Proposed Signal Injection Base Flux Searching Algorithm

To further validate the effectiveness of the proposed flux searching algorithm (P&O and ESC) and the resulting DTC, experimental studies are performed on a bench top IPM drive setup. The overall experimental setup is shown in Figure 7.5. The setup consists of a two-level inverter, an IPM motor, a DC motor and dSPACE 1103 controller platform. Additionally, the proposed ESC based DTC scheme, the DC motor controller is also realized in the dSPACE platform. The DC motor was connected to the H-bridge converter which is also shown in the Figure 7.5. The sampling frequency of the DTC algorithm is 55 kHz. The references for the control can be easily controlled from the dSAPCE proprietary software ControlDesk in real time.

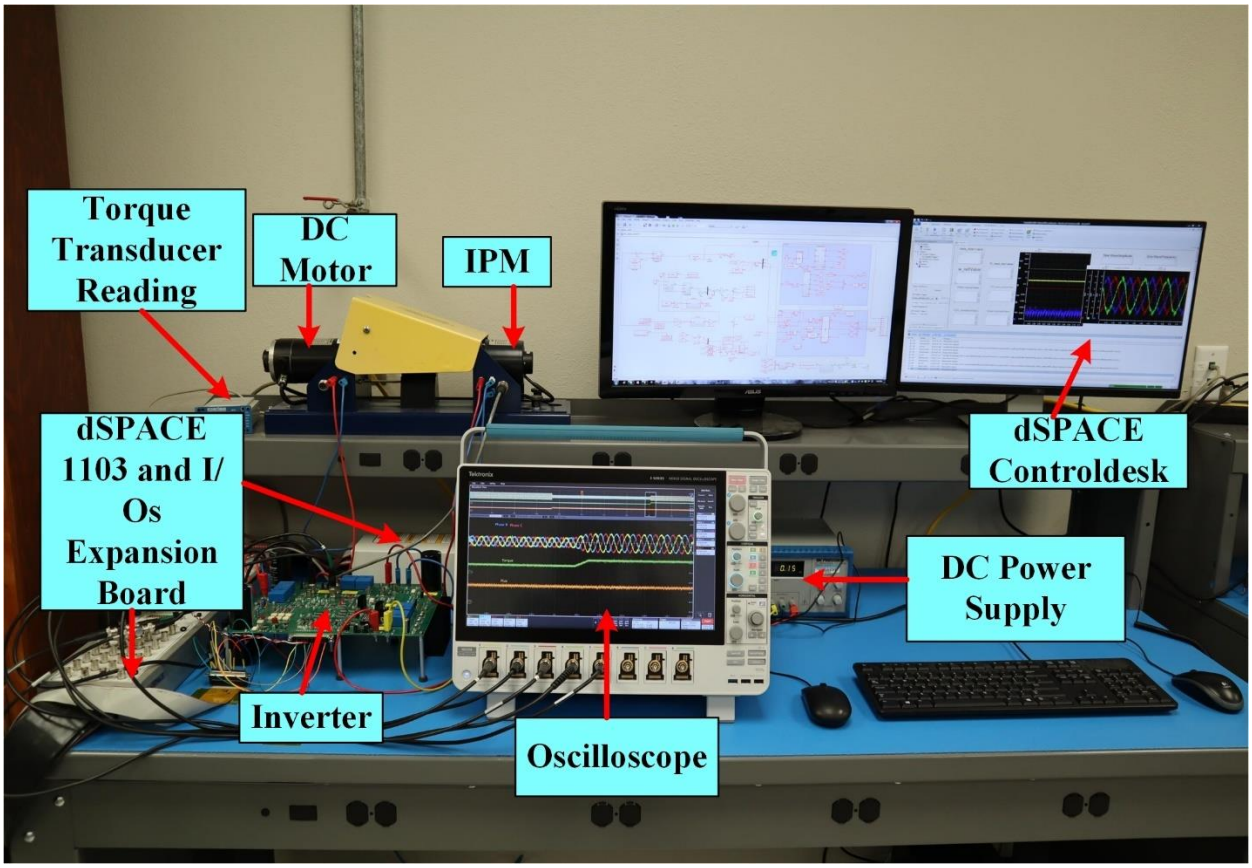

Figure 7.5: Experimental setup for optimal flux searching algorithm with DTC.

CHAPTER 8

SIMULATION AND EXPERIMENTAL VALIDATION

8.1 Introduction

In this chapter, various simulation and experimental results are presented to verify the effectiveness of the methods developed and the associated algorithms for the motor drive. Additionally, the challenges faced in the simulations and experiments are also discussed.

8.2 Simulation Studies for Advanced Direct Torque Control with Virtual Voltage Vector for IPMSM

8.2.1 DC-link Cpapacitor Voltage

Figure 8.1 shows the DC-link capacitor voltages, i.e., V_{c1} and V_{c2}, when using the conventional DTC for 3-L T-type NPC converter with additional DC-link voltage balancing control, which requires the measurements of the two capacitor voltages using voltage sensors. At first, the torque reference is increased from 0.3Nm to 0.7Nm and then step changed to -0.3Nm to see the effect of the transient on the DC-link capacitor voltage balancing. As show in Figure 8.1, the ripples of the DC-link capacitor voltages are higher when the torque reference is larger. However, the dc capacitor voltages deviated when torque changed its direction with V_{c1} dropped to zero, while V_{c2} was equal to the dc bus voltage. In this condition, the 3-L inverter operated as a 2- Level inverter, which however may overstress the power devices and bottom capacitors in practical applications if they are selected based on half of the dc bus voltage. Figure 8.2 shows the capacitor voltages when using the proposed DTC with VSVs under the same torque reference profile. The voltage ripples were noticeably reduced, and system remained stable even when torque changed its

direction. The transient of the torque reference does not affect the DC-link capacitor voltages when the proposed VSV based DTC is applied.

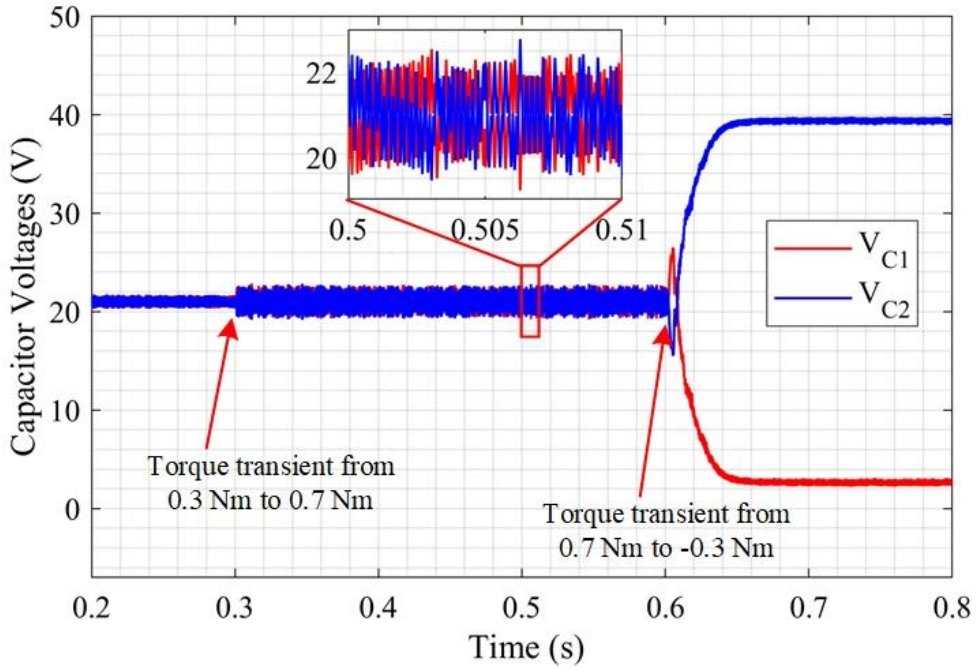

Figure 8.1: DC-link capacitor voltages when using the conventional DTC.

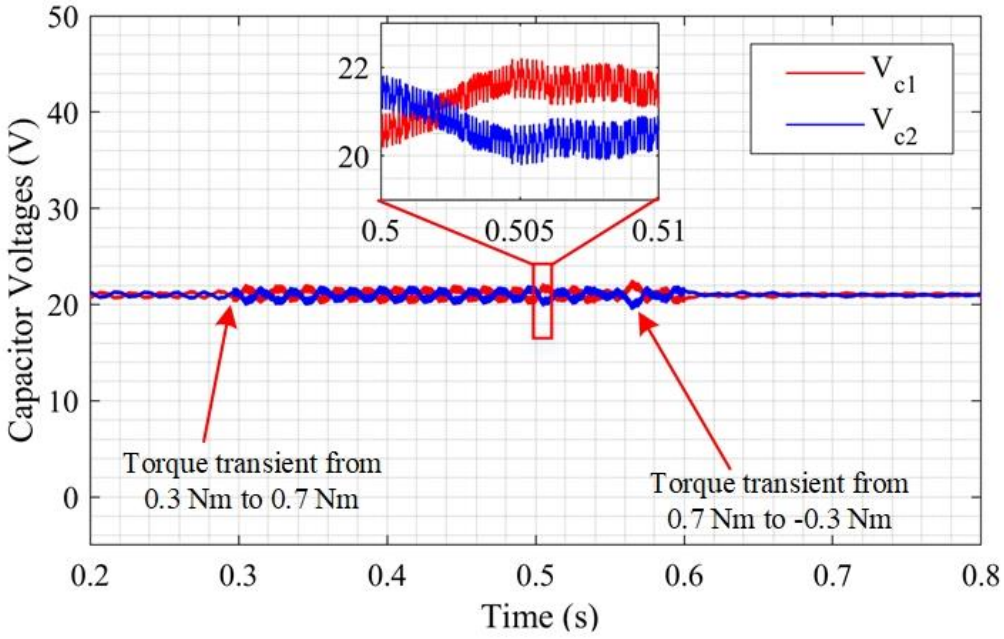

Figure 8.2: DC-link capacitor voltages when using the proposed DTC.

8.2.2 Torque Response

Figure 8.3 shows the torque response of the IPM motor when the conventional DTC algorithm is applied. At first the torque reference was kept constant at 0.3Nm, then first step change was applied from 0.3Nm to 0.7Nm and at the end another step change was applied from 0.7Nm to -0.3Nm. From the previous Figure 8.1, it was show that the when the torque changes its direction the DC-link capacitor voltages can diverged and that affects the torque ripple which is shown in the Figure 8.3. On the other hand, when the same torque profile was applied to the proposed DTC the torque ripple was significantly reduced and the at the same time the capacitor voltages were balanced. The torque response from the proposed DTC is shown in Figure 8.4. When the DC-link is balanced, the torque ripples are 0.06Nm and 0.055Nm for conventional and proposed approach, respectively. Additionally, when the DC-link is unbalanced, the conventional DTC has 0.1Nm torque ripple whereas the proposed DTC has balanced DC-link and torque ripple reduced more to 0.054Nm.

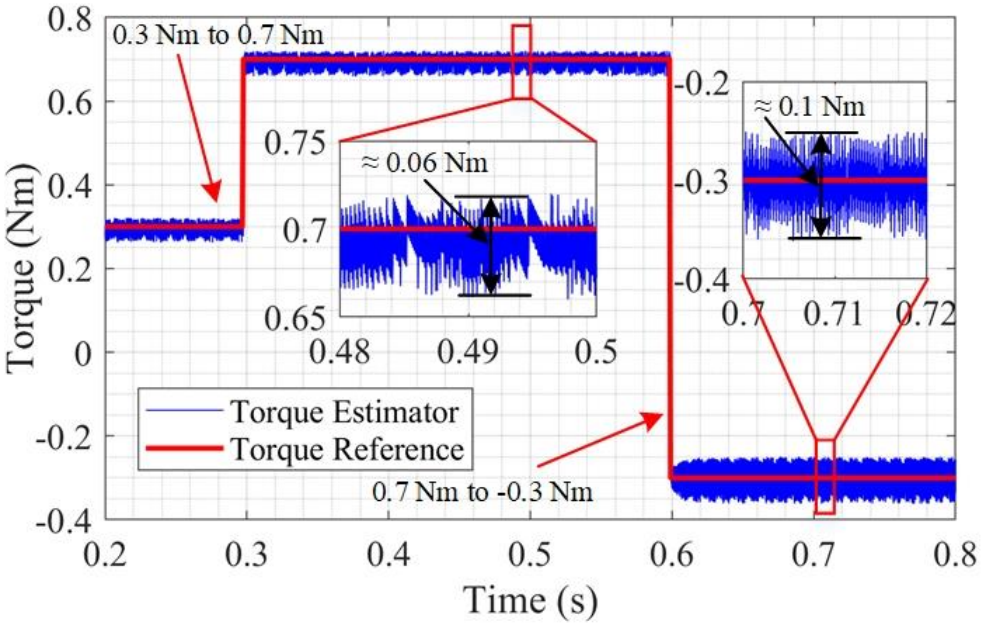

Figure 8.3: Torque response when using the conventional DTC.

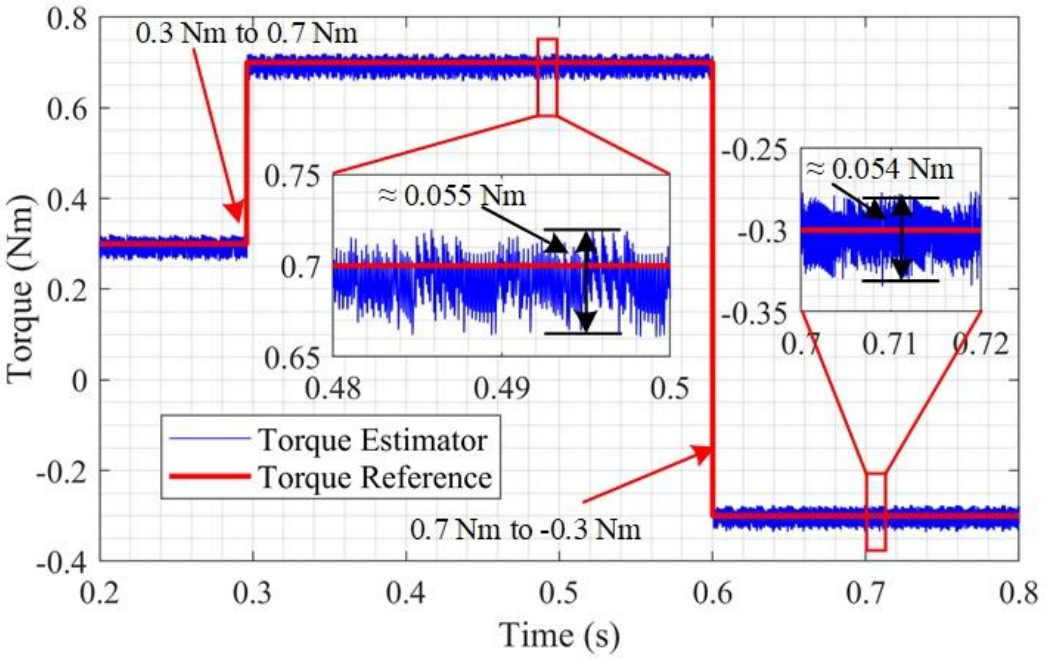

Figure 8.4: Torque response with proposed DTC.

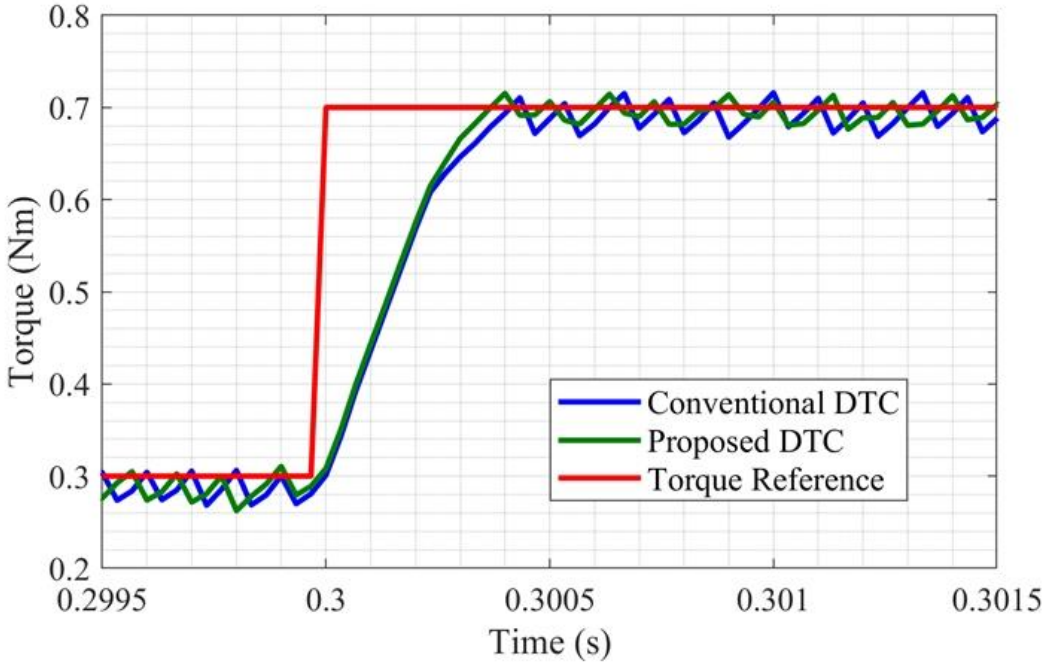

Figure 8.5: Comparison of the dynamic responses.

The transient performance was also evaluated for both the conventional and proposed DTC as shown in Figure 8.5. The DC-link capacitor voltages were clamped at constant using dc voltage

sources, such that this simulation study can expose the dynamic performance for both method without the dc link unbalancing issue. The proposed DTC used the same hysteresis band as the conventional DTC. Therefore, in the beginning, both methods had the same slew rate of the torque increment. Then proposed DTC had higher slew rate of the torque increment due to the insertion of middle voltage hexagon, while the conventional DTC was using the vectors on the inner voltage hexagon. At the steady state, both methods had the similar torque ripple since there is no DC-link voltage unbalancing issue. Now the torque transient response can be tuned by tuning the large hysteresis band. The torque transient response is shown with different value of the large hysteresis band in Figure 8.6.

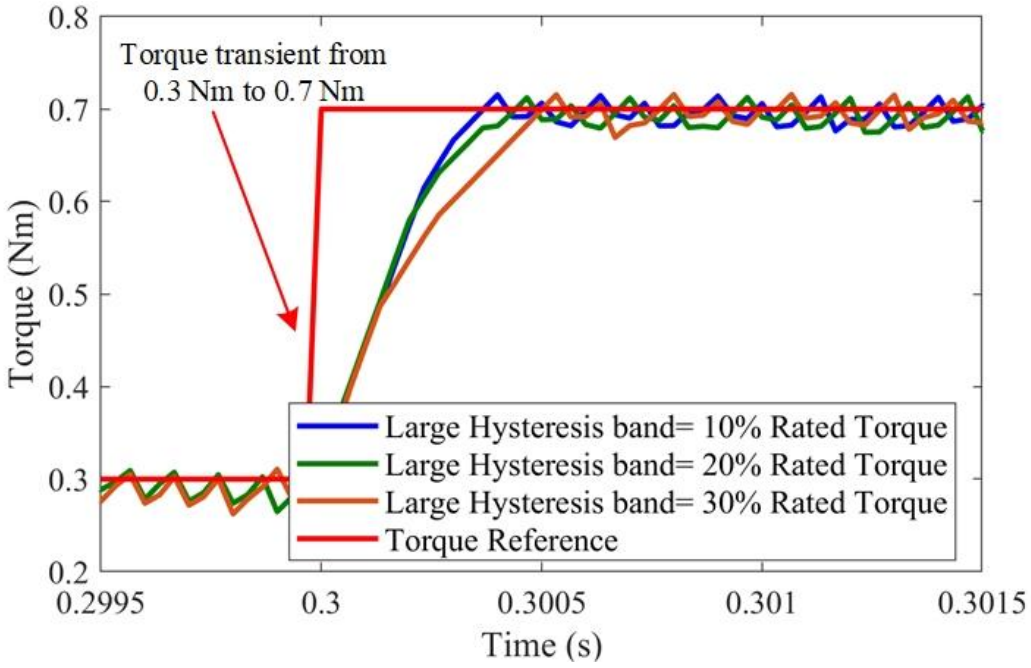

Figure 8.6: Comparison of the dynamic responses of different value of the large hysteresis band.

8.2.3 Stator Current Respsonse

Figure 8.7 shows the corresponding stator currents while the IPM motor was following the same torque profile as Figure 8.4. The THD was 6 % when the DC-link was balanced and 11%

with unbalanced dc link. In contrast, Figure 8.8 shows the phase current THD for the proposed DTC, which is lower comparing to the conventional DTC.

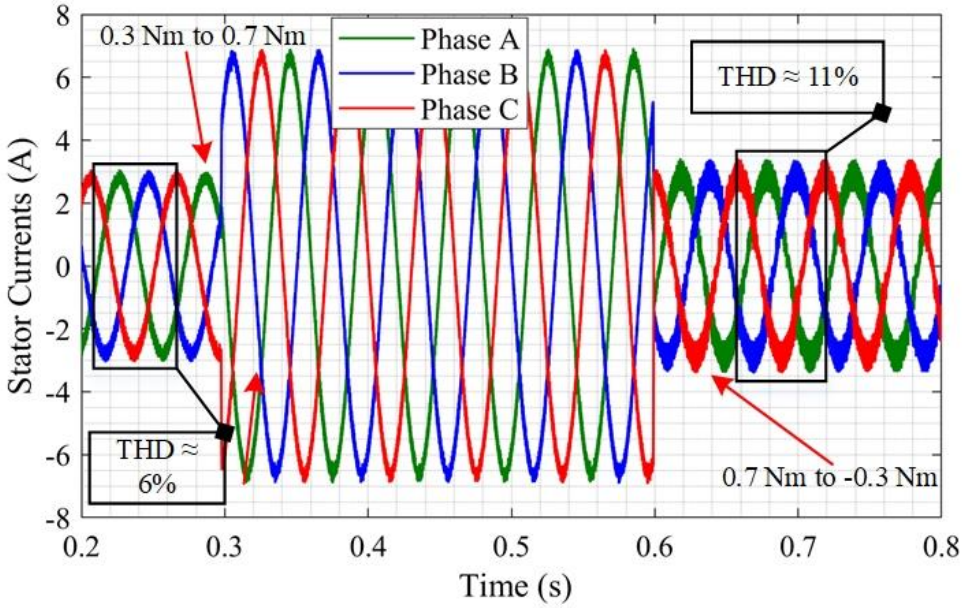

Figure 8.7: Three phase stator currents when using the conventional DTC.

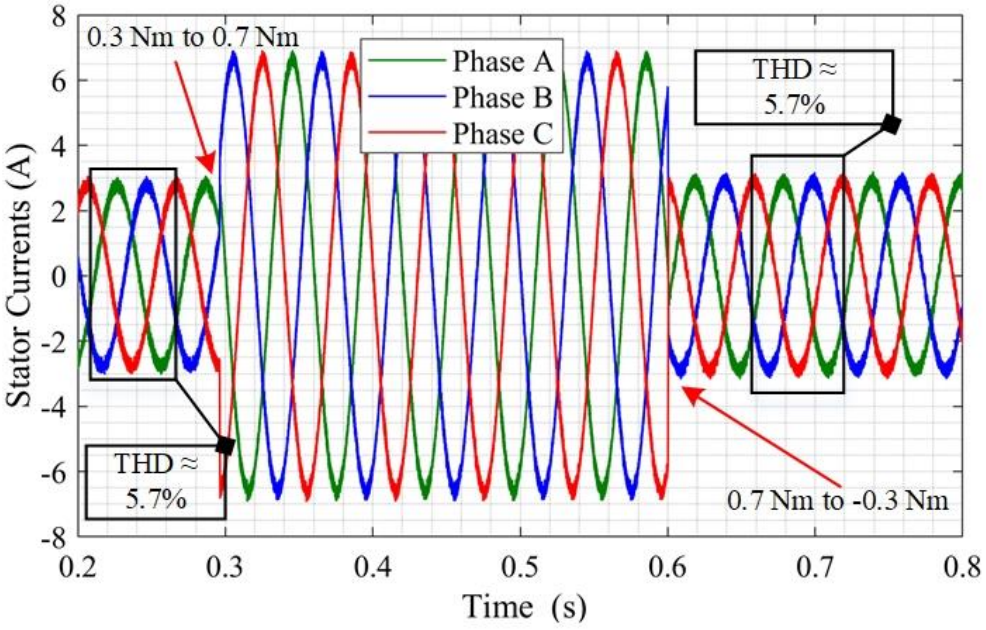

Figure 8.8: Three phase stator currents with proposed DTC.

8.2.4 Speed-Torque Charecteristic

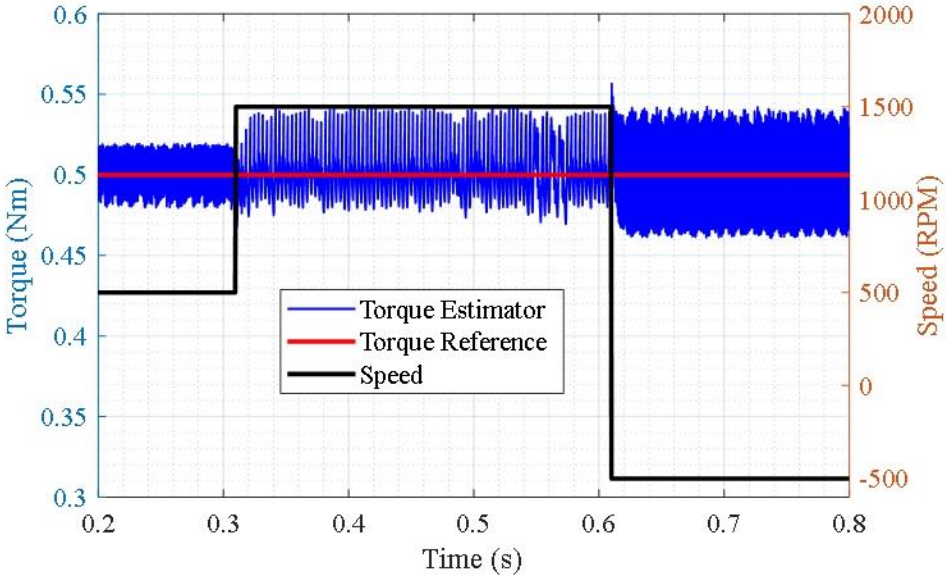

Figure 8.9: Speed and torque characteristic with conventional DTC.

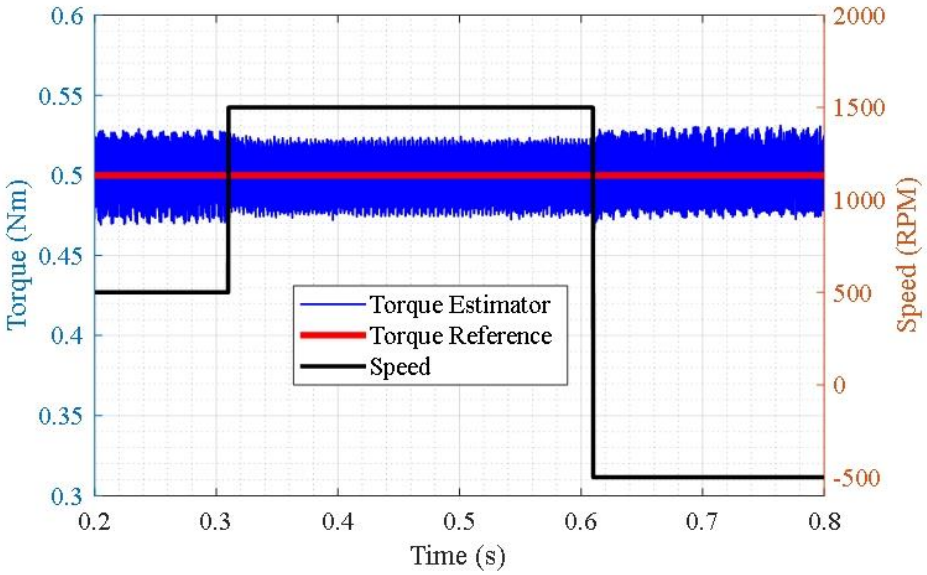

Figure 8.10: Speed and torque characteristic with proposed DTC.

The conventional and the proposed DTC both methods were validated for variable speed profiles. Figure 8.9 and Figure 8.10 represent reference toque and torque estimator output under a

variable speed profile. As shown in Figure 8.9, at higher speed and speed reversal, due to DC-link capacitor voltage offset, the conventional method suffers from high torque ripples. On the other hand, the proposed DTC method has lower torque ripple since the DC-link capacitor voltages are balanced which can be seen from Figure 8.10.

8.2.5 Neutral Point Current

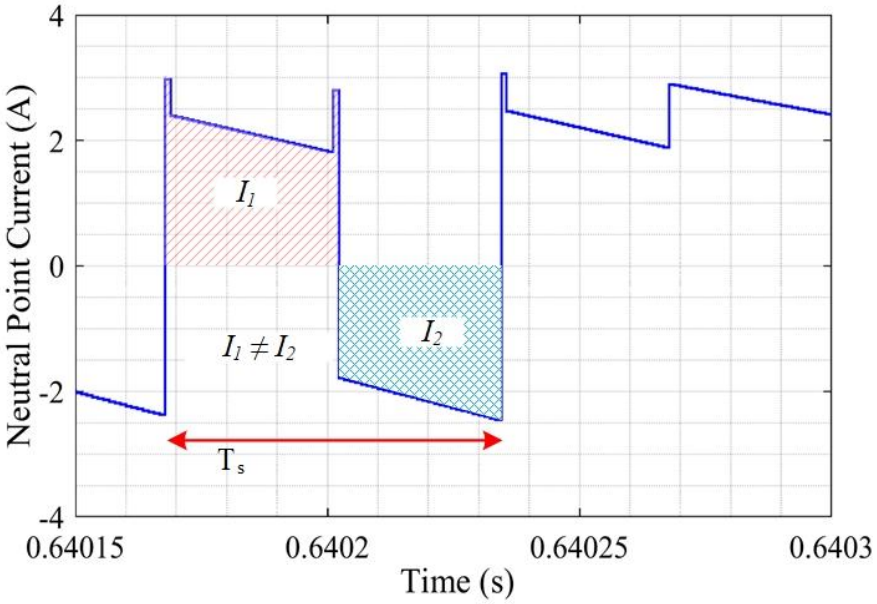

Figure 8.11: Neutral point current, i_n with convention DTC.

In the simulation the neutral point current was measured to validate the effectiveness of the proposed DTC and compare with the conventional DTC approach. Neutral point current is the main reason behind the DC-link capacitor unbalance issue. If the neutral point current is flowing through the systema and the average of the neutral point current is not zero over one switching period, then that will cause the capacitor voltage unbalancing. In the conventional method the neutral point current is not zero over one switching cycle shown in Figure 8.11 and in contrast the proposed method can balance the neutral point current without measuring the voltage or current which is shown in Figure 8.12.

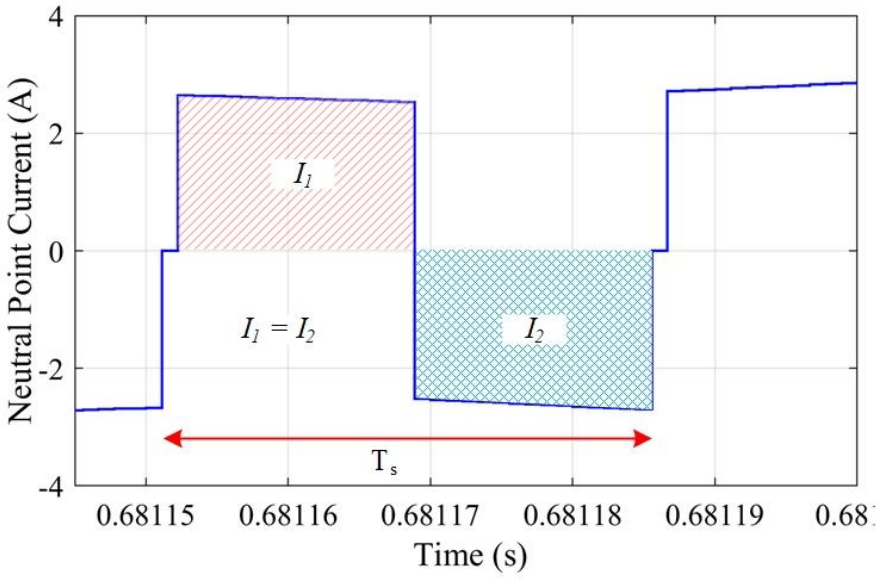

Figure 8.12: Neutral point current, i_n with proposed DTC.

8.2.6 Inverter Loss Analysis

Inverter losses are major part of the overall system loss and its affects the efficiency of the system as well. Moreover, the additional switching actions of the proposed DTC, the system efficiency can be lower than that when using the conventional DTC. Hence, in this section T-type NPC inverter losses are evaluated for both conventional and proposed DTC approaches to quantify the impact to the system efficiency. Switching losses and conduction losses data are extracted from the device datasheet [121]. The proposed loss model the conduction loss of a MOSFET is the 1st or 3rd quadrant can be determined as (8.1) and (8.2), respectively [64], [27],

$$P_{con(F)} = I_D^2 \cdot R_{DS(on)(F)} \tag{8.1}$$

$$P_{con(R)} = \begin{cases} I_D^2 \cdot R_{DS(on)(R),} I_D \le I_{SC} \\ I_D^2 \cdot R_{DS(on)(R)}^{'} + V_{TH} \cdot I_{D,} I_D > I_{SC} \end{cases} \tag{8.2}$$

where, I_D and I_{SC} are the MOSFET drain and the threshold current, respectively. $R_{DS(on)(F)}$ and $R_{DS(on)(R)}$ are the on-state resistances of the devices. $R'_{DS(on)(R)}$ and V_{TH} are the equivalent resistance

and the voltage source of the MOSFET and diode parallel circuit, respectively. The switching loss can be represented as,

$$E_{on} = \frac{E_{on(datasheet)} \cdot V_{DS(test)}}{V_{DS(datasheet)}} \tag{8.3}$$

$$E_{off} = \frac{E_{off(datasheet)} \cdot V_{DS(test)}}{V_{DS(datasheet)}} \tag{8.4}$$

where, E_{on} and E_{off} are the device turn-on and turn-off losses. $E_{on(datasheet)}$ and $E_{on(datasheet)}$ are turn-on and turn-off losses at a specific voltage mentioned in the datasheet of the power device. $V_{DS(datasheet)}$ is the voltage used in the switching characterization by the manufacturer also specified in the datasheet. The diode reverse recovery loss can be denoted as,

$$E_{rr} = \frac{E_{rr(datasheet)} \cdot V_{DS(test)}}{V_{DS(datasheet)}} \tag{8.4}$$

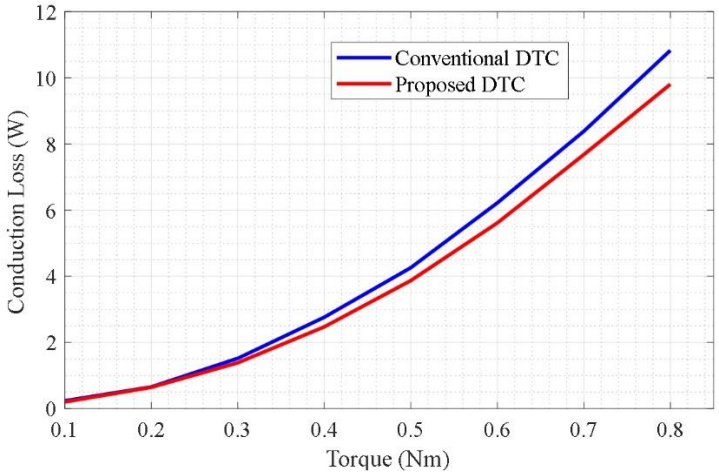

Figure 8.13: Conduction loss for conventional and proposed DTC at 1000 RPM.

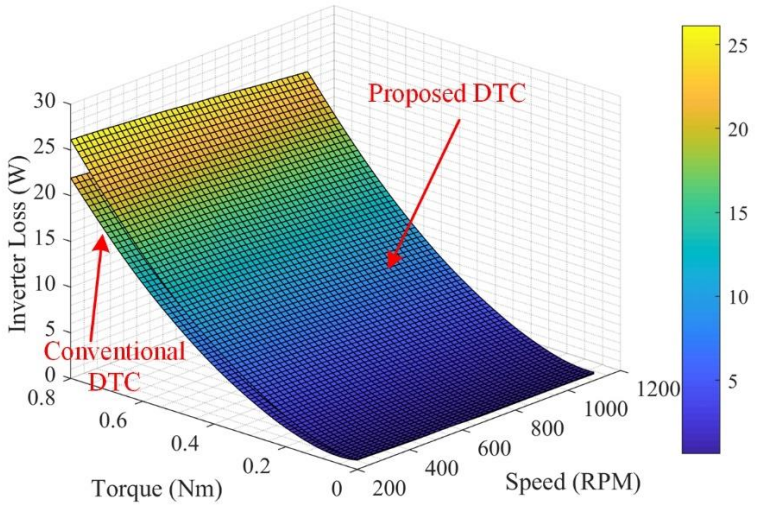

Figure 8.14: 3D map of the inverter loss for the conventional and proposed DTC.

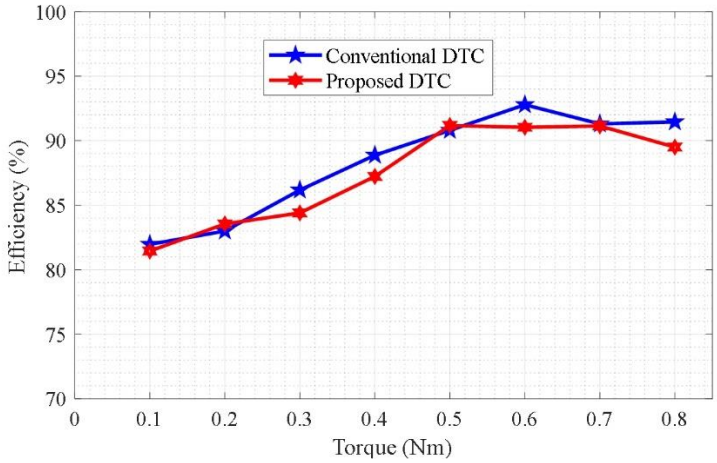

Figure 8.15: Efficiency curve for conventional and proposed DTC.

The ohmic loss curve is added in this section which is shown in Figure 8.13. Simulations for different operating conditions are conducted to analyze the losses of the inverter for conventional and proposed DTC methods. As shown in Figure 8.14, since the proposed method has higher equivalent switching frequency, it has higher switching losses than the conventional DTC. However, since the SiC MOSFETs are used in this study, the conduction losses of the power devices

are still dominant. Therefore. The efficiency of the system is reduced less than 1% over a wide operating range using the proposed method. Figure 8.15 is the efficiency curve for both methods.

8.3 Experimental results for Advanced Direct Torque Control with Virtual Voltage Vector for IPMSM

8.3.1 DC-link Cpapacitor Voltage

Figure 8.16 shows the experimental results when using conventional DTC for three-level converter without an additional control loop for DC-link voltage, as such the DC-link capacitor voltages were biased and unequal to each other. It is clear to witness from Figure 8.16 that when ΔV_{dc} is almost 60% then the torque ripple is around 40% which were close to the numerical analysis done in Figure 4.8. To compare the conventional DTC with the proposed DTC, experiment was conducted, and results are shown in Figure 8.17, where the DC-link capacitor voltages were quite close to each other before and after torque step change. Additionally, both torque and stator current ripples reduced significantly due to VSVs in the proposed DTC which can be observed from the Figure 8.16 as well. Figure 8.18 shows the speed transient response when the DC-link balanced.

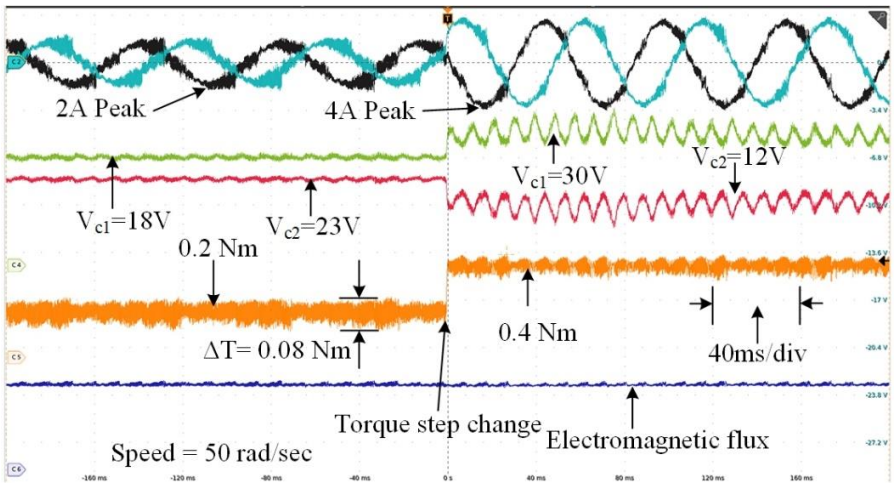

Figure 8.16: DC-link unbalanced condition with torque transient.

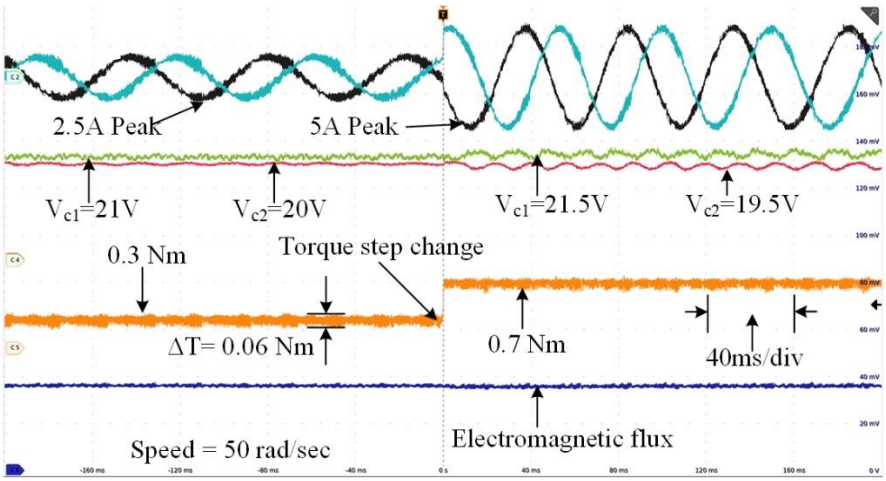

Figure 8.17: DC-link balanced condition with torque transient.

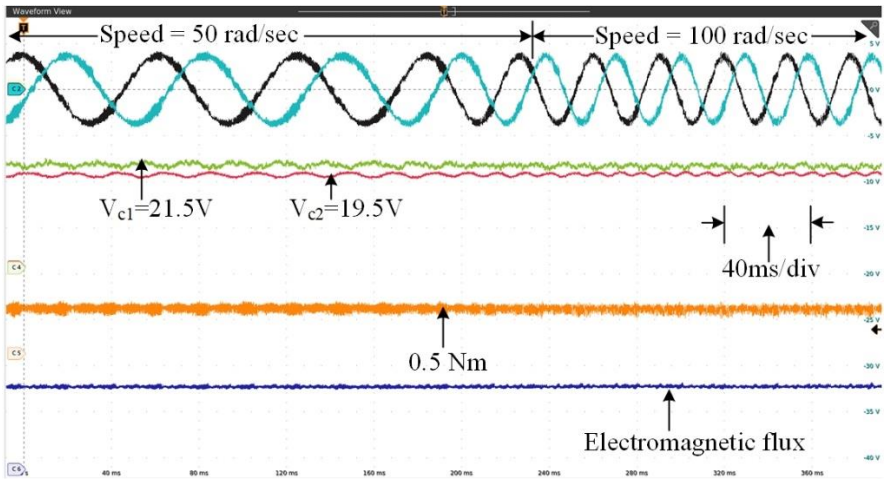

Figure 8.18: DC-link balanced condition with speed transient.

8.3.2 Performace Under Different Speed Profile

To compare the performance of the proposed method with the conventional DTC over a wide range of speeds, various tests were executed. Figure 8.19 to Figure 8.26 are the results at low speeds and in flux weakening region for both conventional and proposed method, respectively. In Figure 8.19, the speed command is 100 RPM constant. The conventional DTC can balance the DC-link voltages with higher ripples in the stator current and torque compared to Figure 8.21, where the results from the proposed DTC are shown with same operating conditions which is low

speed region. Operation in the flux weakening mode was also considered using conventional and proposed DTC as shown in Figure 8.20 and Figure 8.22, respectively. As shown in Figure 8.20, the conventional DTC has higher DC-link voltage offset between the capacitors and that results higher torque and stator current ripples compared to the proposed method in Figure 8.22. And the DC-link voltages are balanced with the VSV based DTC as well.

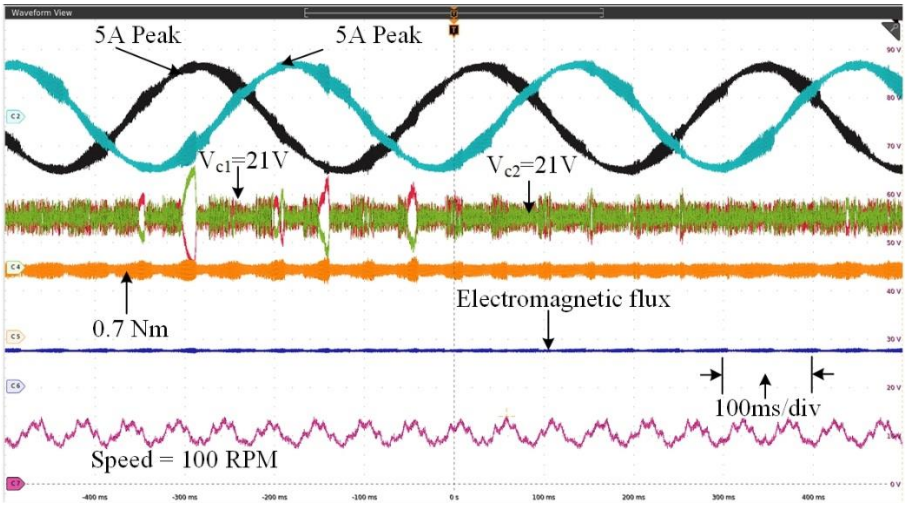

Figure 8.19: Low speed response with conventional DTC.

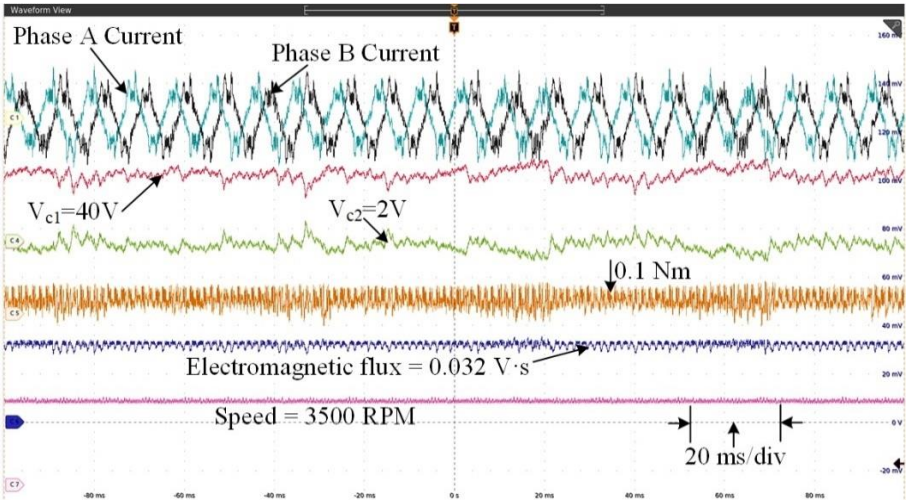

Figure 8.20: Conventional DTC in flux weakening region.

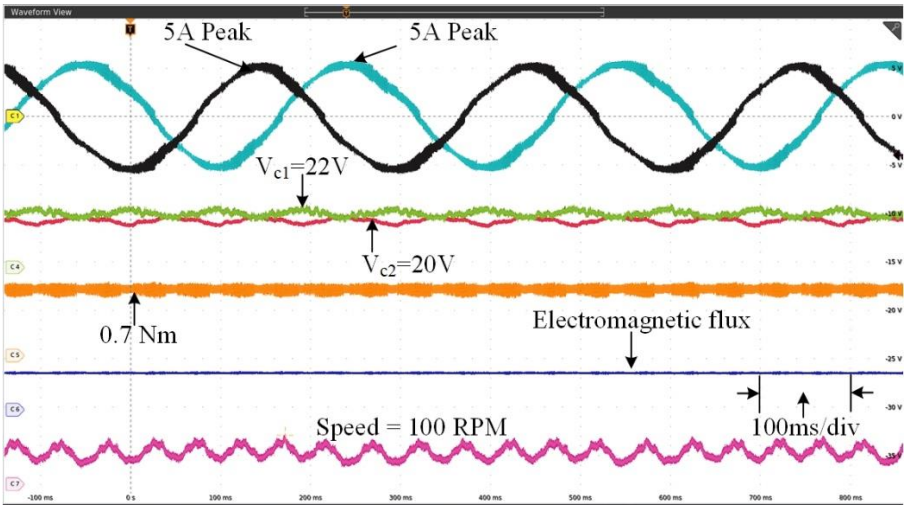

Figure 8.21: Low speed response with proposed DTC.

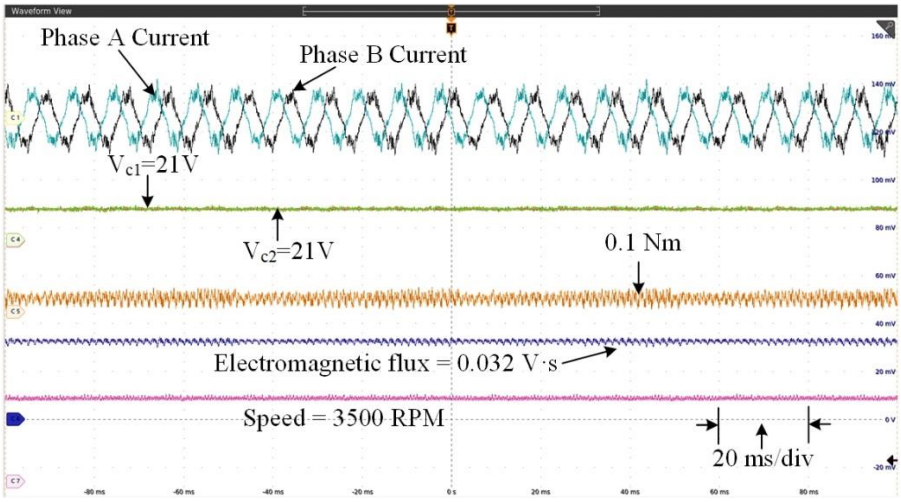

Figure 8.22: Proposed DTC in flux weakening region.

Acceleration and speed reversal of the motor experiments were also performed to validate the performance of the proposed DTC method. Figure 8.23 shows the acceleration of the motor from 500 RPM to 1500 RPM using conventional DTC. The DC-link voltages are measured and considered for selecting the appropriate voltage vector in the conventional DTC method, therefore the V_{c1} and V_{c2} are balanced. However, when the reverse speed is applied, i.e., from 500 RPM to -1000 RPM, the conventional DTC cannot maintain balanced DC-link which is shown in Figure 8.24. In contrast, in both acceleration and speed reversal mode of operation the proposed DTC can

maintain balanced DC-link voltages with less torque and current ripples, which are confirmed in Figure 8.25 and Figure 8.26, respectively.

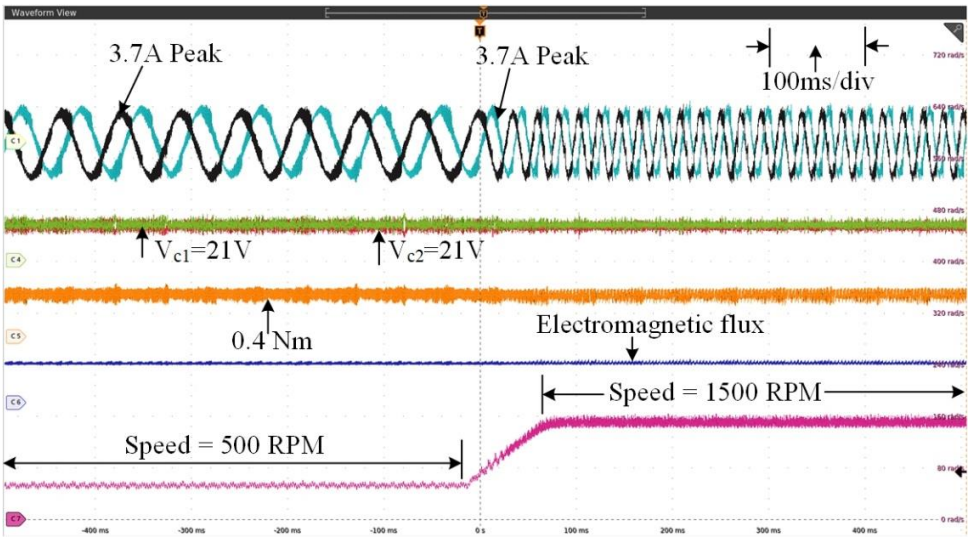

Figure 8.23: Acceleration of the motor with conventional DTC.

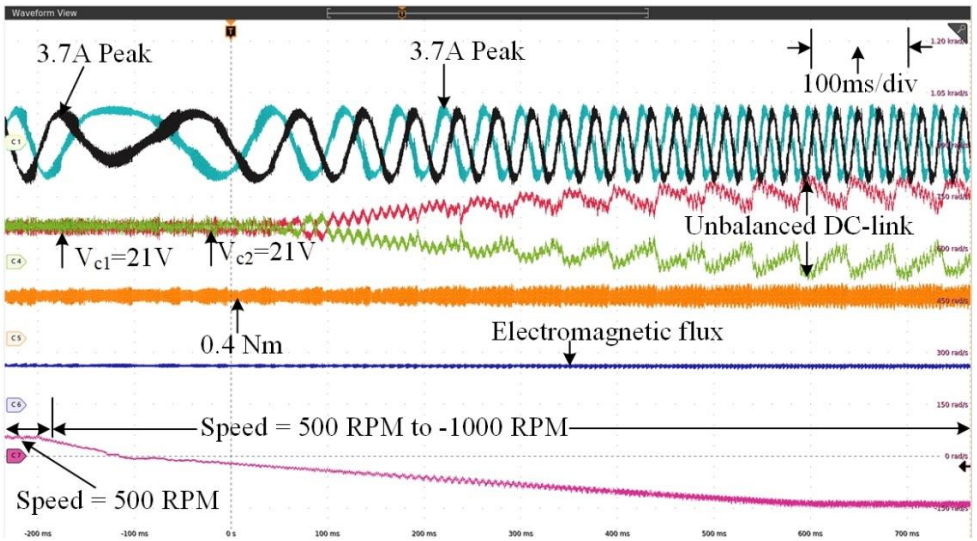

Figure 8.24: Speed reversal of the motor with conventional DTC.

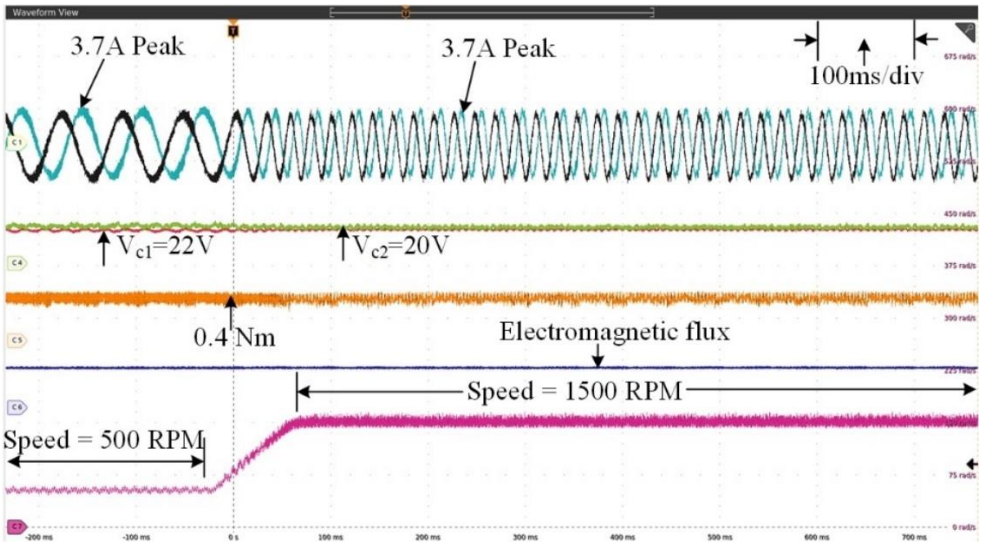

Figure 8.25: Acceleration of the motor with proposed DTC.

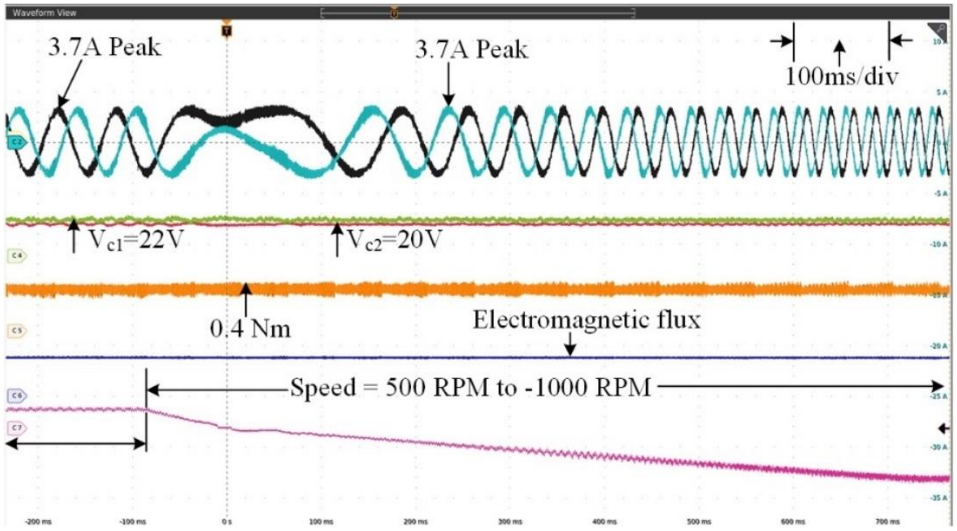

Figure 8.26: Speed reversal of the motor with proposed DTC.

8.3.3 Torque , Flux and Satator Current Ripples in the Steady State

To analyze the torque ripples more carefully and evaluate the performance of both conventional and the proposed DTC, the torque data was saved for the experiment and processed in MATLAB later. Figure 8.27 shows the steady state torque ripples comparison between the conventional and proposed DTC when the command torque is 0.4 Nm. From the figure, it is clear

that the proposed advanced DTC has more than 20% less torque ripple than the conventional DTC when the speed is maintained at 1500 RPM.

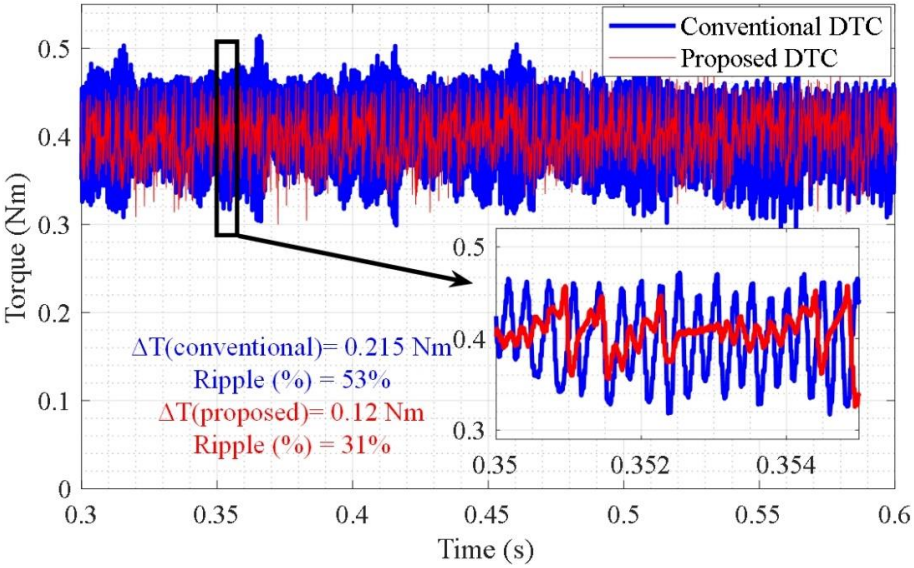

Figure 8.27: Steady state torque comparison between conventional and proposed DTC.

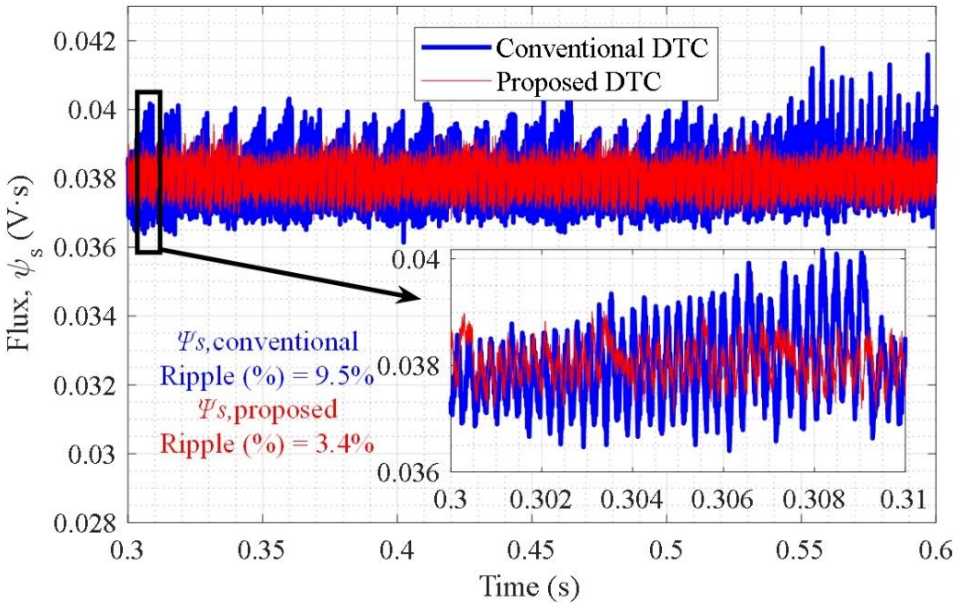

Figure 8.28: Flux ripple comparison for both control method.

Flux ripples also reduced to 3.4% using the proposed DTC, which is 6% less the conventional DTC. The flux ripple comparison is shown in Figure 8.28. Figure 8.29 represents the THD (%) of the stator current from the experimentally measured current which was analyzed in MATLAB. The conventional DTC has higher stator current THD (%) than the proposed DTC as shown in the Figure 8.29. Both simulation and experimental results validate the proposed enhanced DTC with of IPM machine.

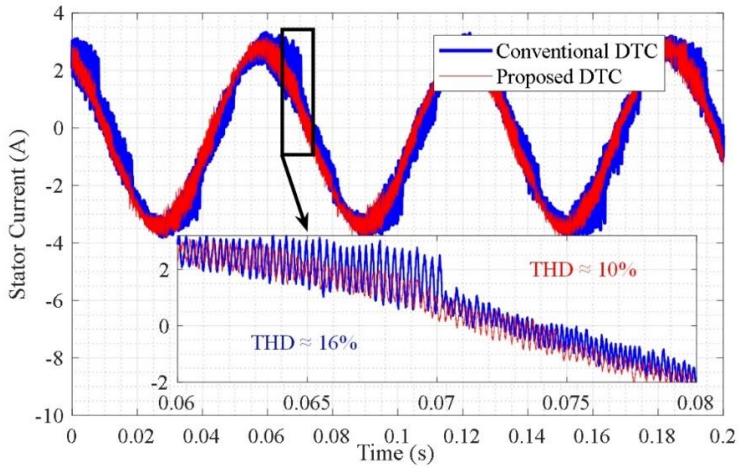

Figure 8.29: Stator current THD (%) for both conventional and proposed DTC at 0.4 Nm torque.

8.3.4 Torque Transient Response

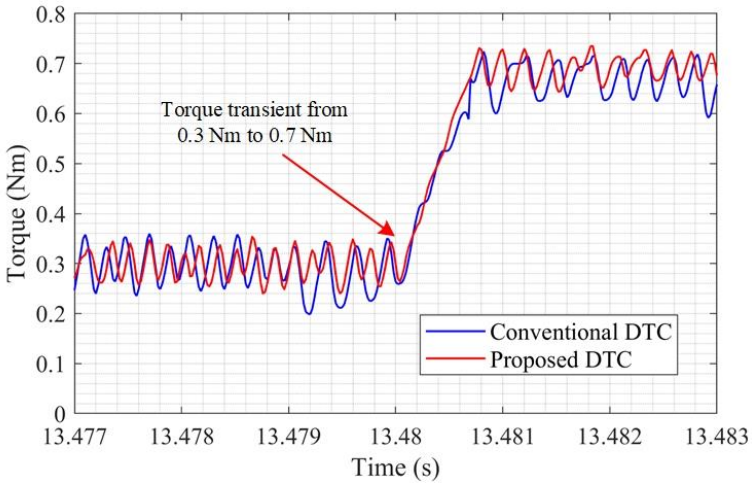

Figure 8.30: Torque dynamics for both conventional DTC and proposed DTC.

The major advantage of the DTC is the fast dynamic response. Therefore, any upgrade or customization in DTC approach should have similar dynamic performance as the conventional DTC. Torque response with step change in the torque command is shown in Figure 8.30, where the dynamic responses are similar to each other under the conventional and proposed DTC.

8.3.5 Average Swithcing Frequency Comparison

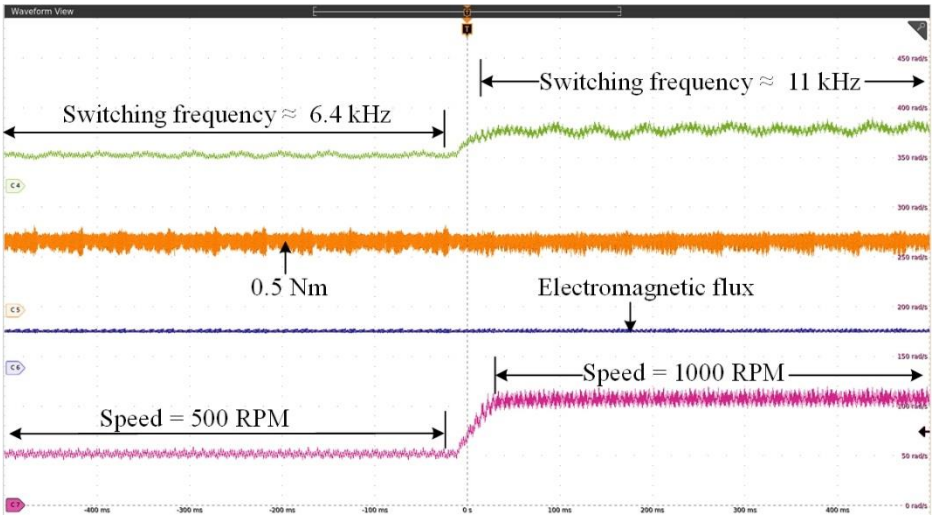

Figure 8.31: Average switching frequency with conventional DTC.

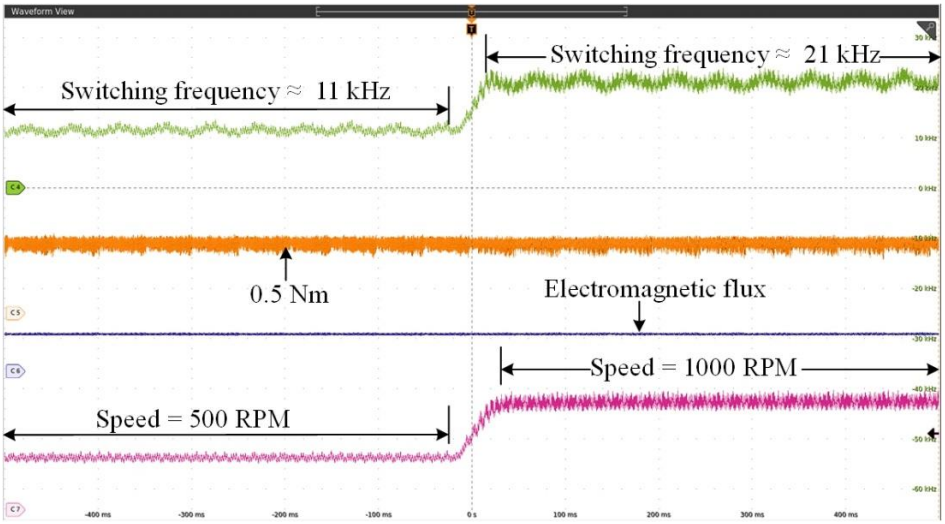

Figure 8.32: Average switching frequency with proposed DTC.

Figure 8.31 and Figure 8.32 below show the average switching frequency of both conventional DTC scheme and proposed DTC scheme. The average switching frequency is measured by the dSPACE and outputted through the on-board digital to analog (DAC) channels. It can be seen that the proposed scheme has higher average switching frequencies due to the implementation of the VSVs which validates the higher switching loss in the proposed DTC comparing to the conventional DTC.

8.4 Simulation studies for Perturb and Observe (P & O) for Optimum Flux searching for IPMSM

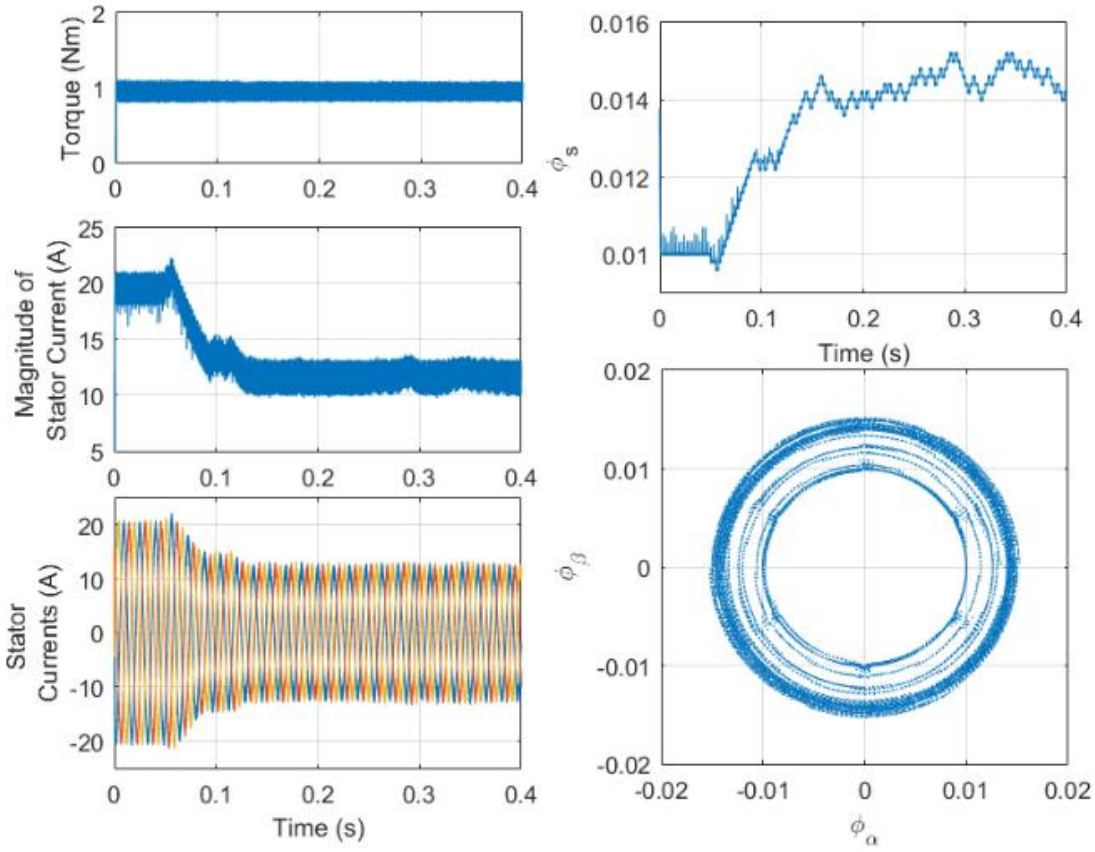

Figure 8.33: Simulation results for torque, stator current and flux when, $T_w = 100 \cdot T_c$.

The window length of the moving average LPF, i.e., T_w, will be critical to the performance of the online optimal ψ_s^* identification. Figure 8.33 and Figure 8.34 compares the performance of the proposed method using different T_w. Figure 8.33 illustrates the case $T_w = 100 \cdot T_c$, where T_c is the sampling period of DTC controller. The motor parameters used for this simulation is shown in Table A-5 in the Appendix. The proposed optimal ψ_s^* searching algorithm is enabled at t = 0.05s, before which, ψ_s^* is a constant 0.01 V.s. It is noticeable that proposed algorithm effectively reduces the magnitude of the stator current, $|I_s|$ from 20 A to 12 A. However, the ψ_s has large variation around its optimal value due to the large window length of the moving average. Figure 8.34 shows the case when $T_w = 314 \cdot T_c$, which is corresponding to half cycle of the fundamental stator current. Similarly, to the previous case, $|I_s|$ reduced from 20 A to 12 A. However, the variation of $\psi_s^*$is much smaller than that shown in the previous case.

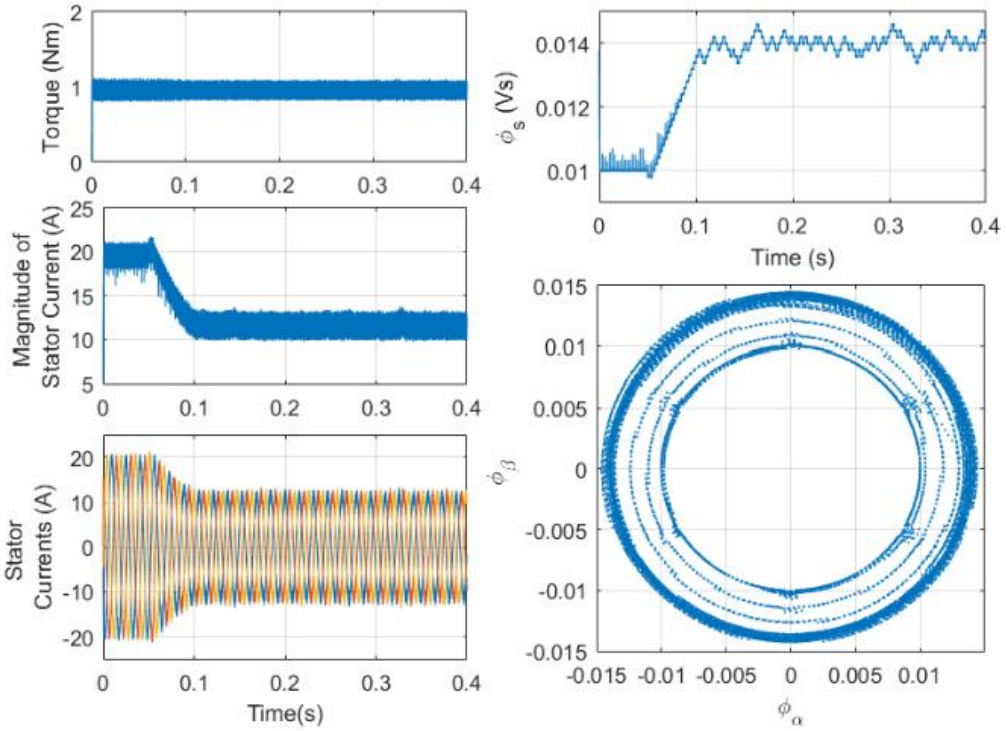

Figure 8.34: Simulation results for torque, stator current and flux when, $T_w = 314 \cdot T_c$.

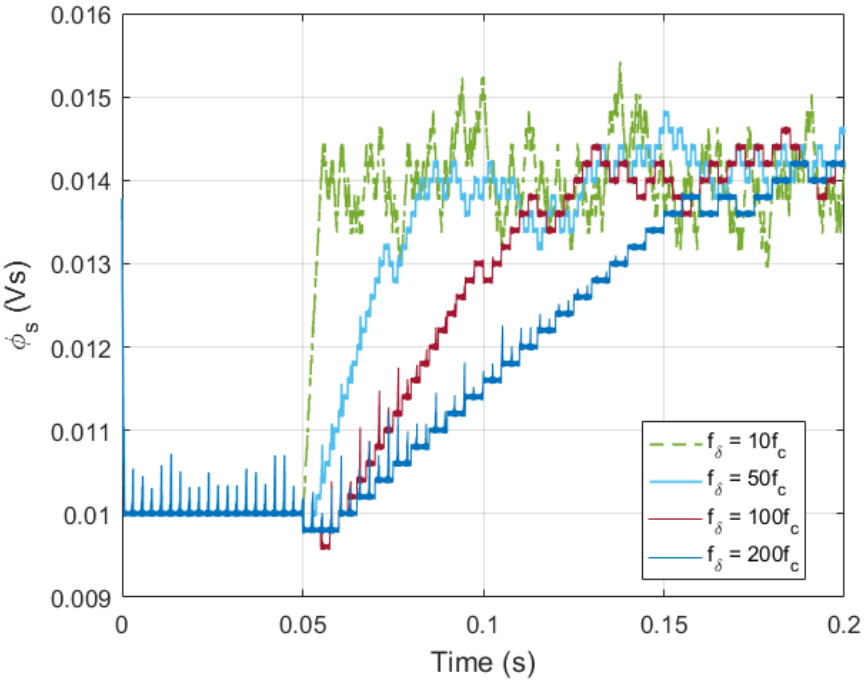

Figure 8.35: The effect of the execution rate of the proposed algorithm.

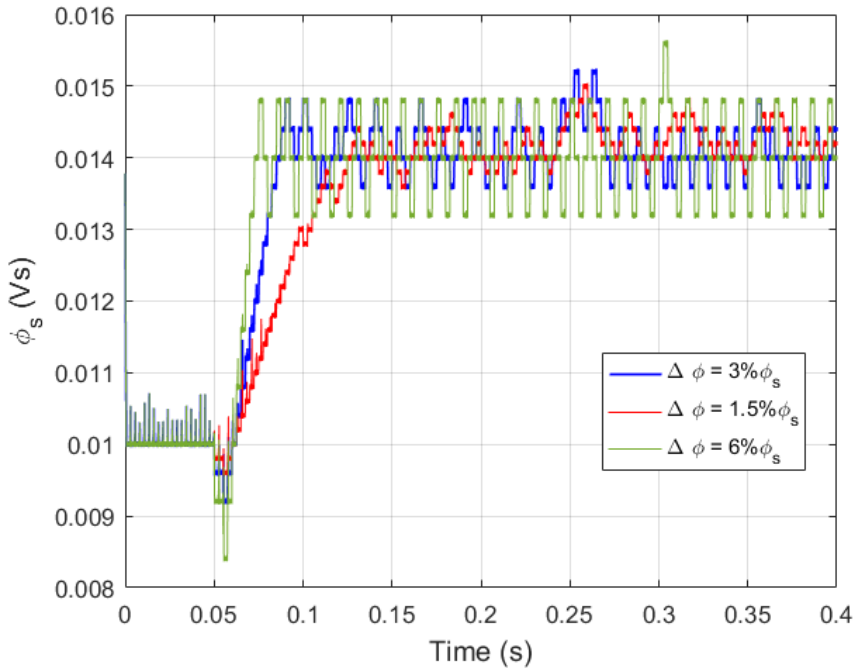

Figure 8.36: The effect of the minimum step the proposed algorithm.

Figure 8.35 reflects the effect of the execution rate, i.e., T_δ, of the searching algorithm. Multiple values are investigated, including, $T_\delta = 10 \cdot T_c$, $50 \cdot T_c$, $100 \cdot T_c$, and $200 \cdot T_c$. When T_δ is too short, e.g., $T_\delta = 10 \cdot T_c$, the convergence speed is fast, however, the steady state oscillation is larger comparing to the other cases. When T_δ is too long, e.g., $T_\delta = 200 \cdot T_c$, the steady state oscillation is significantly reduced at the cost of longer time to converge. Figure 8.36 shows the effect of $\Delta\varphi$, which is the step for the searching algorithm. When $\Delta\varphi = 3\%\ \psi_s^*$, the performance of the search algorithm is the best, which shows a balanced dynamic and steady state performance.

8.5 Experimental Results for Perturb and Observe (P & O) for Optimum Flux searching for IPMSM

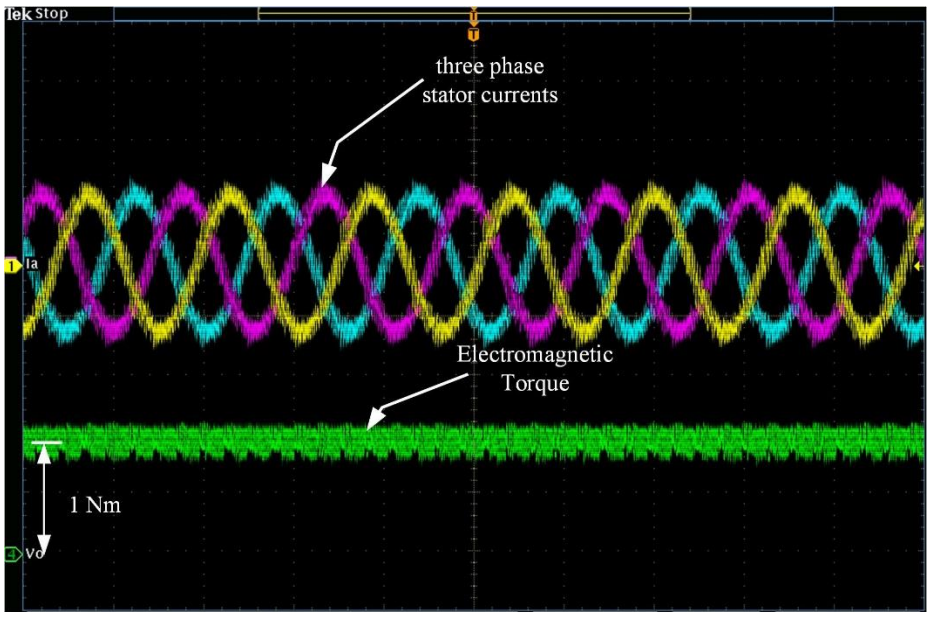

Figure 8.37: Experimental results of the DTC drive at steady state, i.e., 150 rad/s mechanical shaft speed and 1Nm shaft torque and three phase stator currents.

Figure 8.37 shows the experimental results of the DTC drive at the steady state, when the shaft speed is 150 rad/s and shaft torque is 1 Nm. All the 3-phase current waveforms and shaft torque are shown in Figure 8.37. The shaft torque is measured by the torque transducer. In the experimental studies, the sampling frequency of DTC is 20 kHz, and both of the window length of the moving

average LPF and the execution rate of the search algorithm are selected as $50 \cdot T_c$ = 2.5 ms. During the steady state, without using the proposed online optimal flux search approach, the IPM motor was operated at non-optimal operating points. Also, the mechanical rotor position and stator current magnitude is shown in the Figure 8.38.

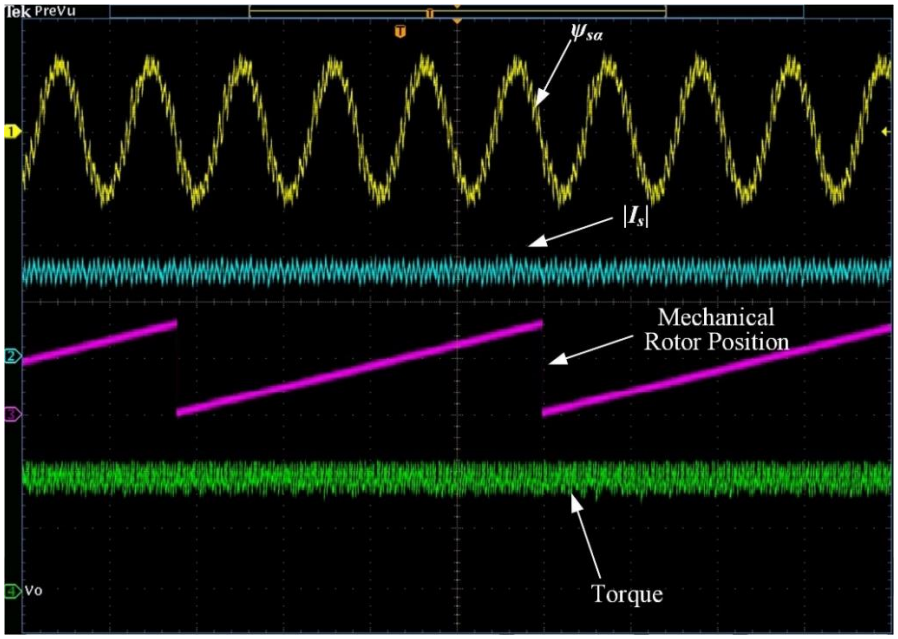

Figure 8.38: Experimental results of the DTC drive at steady state, i.e., 150 rad/s mechanical shaft speed, rotor position and torque.

Once the proposed online optimal flux search algorithm is enabled, the magnitude of the stator current quickly drops to its minimum and the magnitude of the flux linkage converges to its optimal value. The waveform of stator currents and flux linkage are shown in Figure 8.37 and Figure 8.38, respectively. In this typical case, the settling time for the search process is around 40 ms, which is very close to the settling time determined by the simulation studies, shown in Figure 8.34.

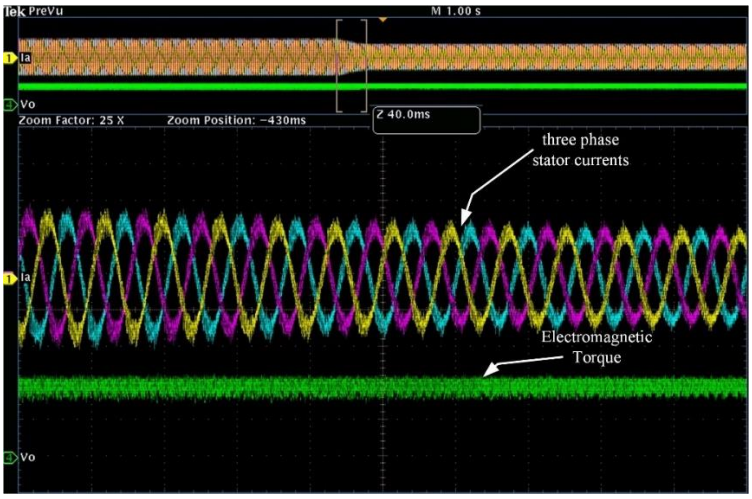

Figure 8.39: Experimental results of the 3-phase stator currents and torque when the proposed searching algorithm was enabled.

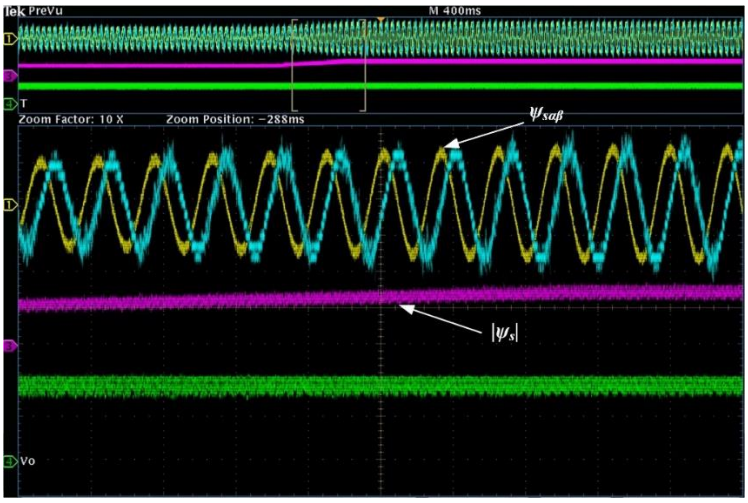

Figure 8.40: Experimental results of $\psi_{s\alpha\beta}$, $|\psi_s|$, and torque when the proposed searching algorithm was enabled.

8.6 Simulation studies for Extremum Seeking control (ESC) for Optimum Flux searching for IPMSM

8.6.1 Speed Profile for the Simulation

In the simulation, the mechanical shaft speed of the IPM motor follows a speed profile which is shown in Figure 8.41 and later various torque references were applied. From the theoretical calculation the optimal stator flux is 0.035 V·s when torque reference is 0.3 Nm. The frequency of

the injected high frequency signal, ω_c is set to be 300 Hz and amplitude is A = 0.00035 V·s, which is 1% of the ψ_s in this dissertation. The sampling frequency of the DTC algorithm in the simulation studies is 55 kHz.

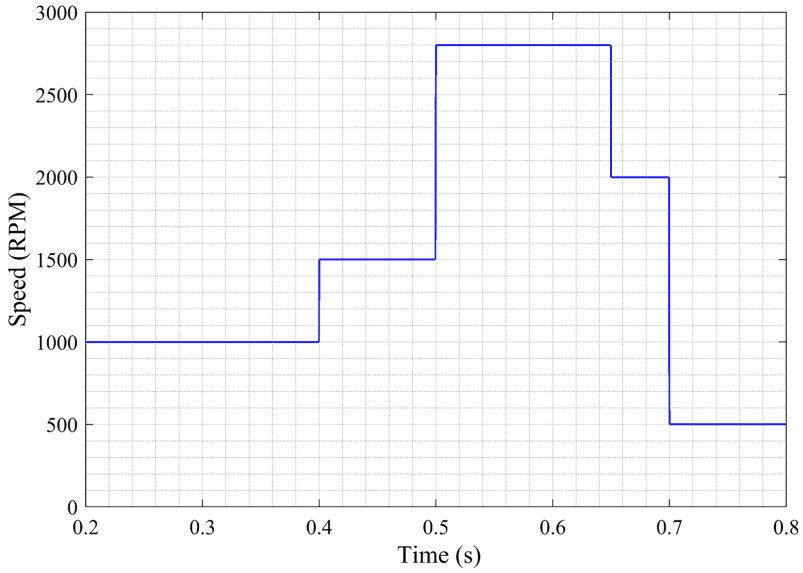

Figure 8.41: Speed profile used in the simulation.

8.6.2 Torque and Flux Transient Responses

For all the simulation results used in this section, the ESC is activated at 0.35 s and a torque profile was used for reference torque to assess the dynamic response of the system. Figure 8.42 shows that the three-phase stator currents reduced from 7 A to 3 A after ESC was activated. Figure 8.43 shows the estimated torque versus the torque reference. When the ESC was activated, at first the torque remains constant and then several step changes in the load torque were applied. From the Figure 8.44, it can be identified that the reference flux, ψ_s^* changed from its initial value to the optimal point when the ESC was activated at 0.35s and finds the optimal flux for various load torque. Figure 8.45 indicates the trajectory of the stator flux, where the inner circle indicates the original stator flux when the motor started, while the outer circle shows the optimal fluxes. With

the proposed ESC activated, the magnitude of the stator current reduces to its lowest possible value, while maintaining the same amount of torque.

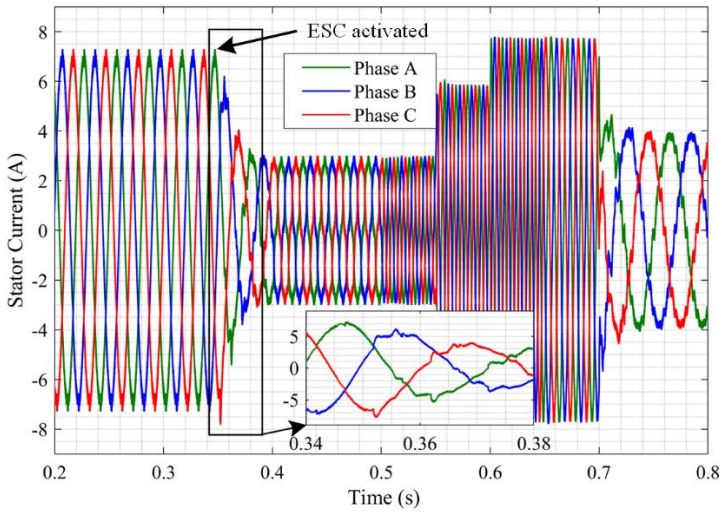

Figure 8.42: Three-phase stator currents.

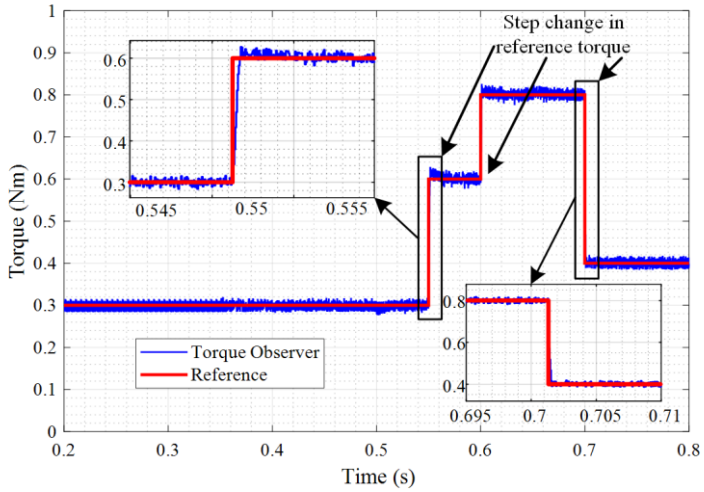

Figure 8.43: Reference torque vs. estimated torque.

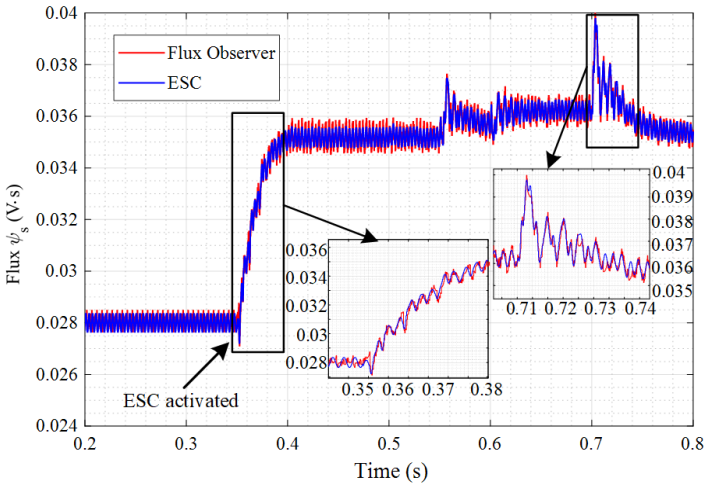

Figure 8.44: Stator reference flux, ψs*.

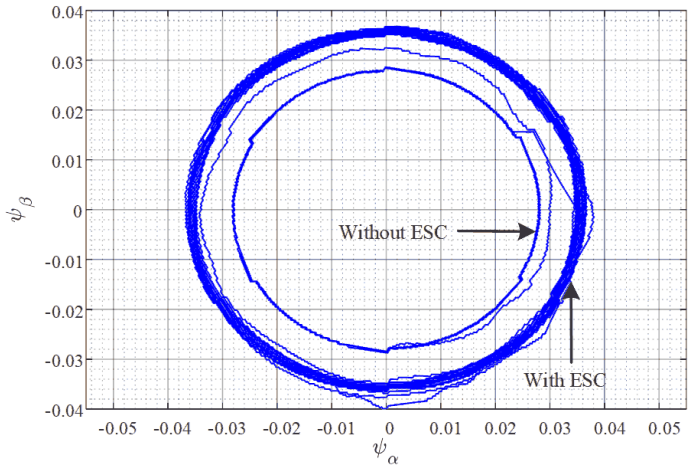

Figure 8.45: α, β flux trajectory.

8.6.3 P & O and ESC Comparison

To compare between the two proposed signal injection based optimal flux searching approaches, the simulation studies were conducted and presented in this section. In Figure 8.46, the P & O flux searching approach result is shown where the flux trajectory is shown when the P & O was activated and the stator current reduced. Figure 8.47 shows the flux trajectory when the ESC was activated at 0.35 s and the stator current reduced to its optimal value for the torque

reference profile which is 0.5 Nm to 0 and then 0 to 0.8 Nm. From both Figure it is conclusive that with ESC algorithm the ripple in the flux reference and the ripples in the torque can be reduced.

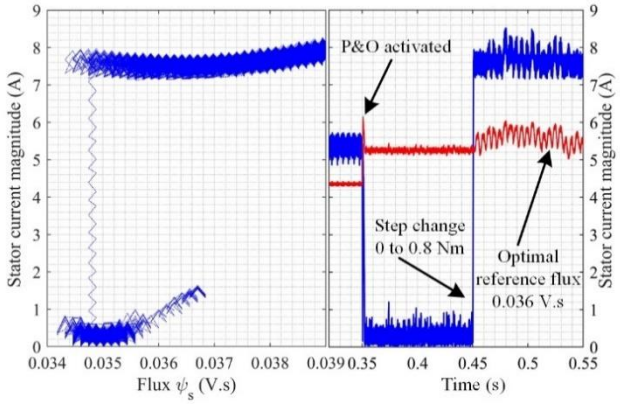

Figure 8.46: Optimal flux after activating the P & O and stator current reduction.

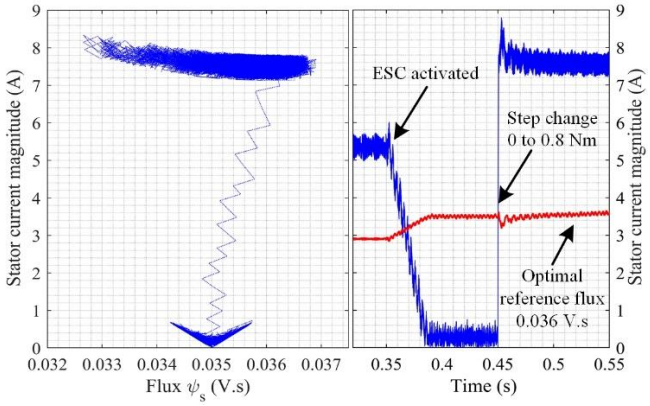

Figure 8.47: Optimal flux after activating the ESC and stator current reduction.

8.7 Experimental Results for Extremum Seeking control (ESC) for Optimum Flux searching for IPMSM

8.7.1 Simulation and Experiemental Results Comaprison for ESC

Figure 8.48 shows the comparison between the simulation and experimental results to demonstrate the relationship between the magnitude of the stator current and the magnitude of the stator flux linkage ψ_s when the torque reference is 0.4 Nm constant. In Figure 8.48, the blue line

indicates the profile obtained from simulation and red line indicates discrete data points from the experiment. When accurate machine parameters are used, simulation results and experimental measurements are close to each other.

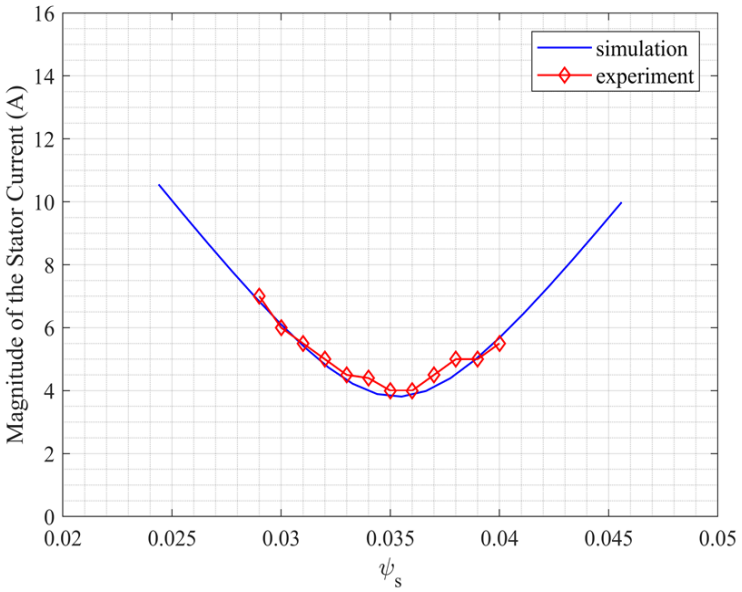

Figure 8.48: Simulation (blue line) vs. experimental (red line) result comparison at T^* = 0.4 Nm.

8.7.2 Flux Trajectory

Figure 8.49 show the actual flux and stator current magnitude trajectory where, ESC was activated when the reference torque was 0 Nm. Then a step change in the torque is applied from 0 to 0.8 Nm and the flux linkage reaches to its optimal point which is 0.036 Vs. Figure 8.50 indicates the dynamic response of proposed control approach before and after activating the ESC while the toque remained constant 0.4 Nm. Figure 8.51 shows flux trajectory of the searching approach, P & O when the torque reference was also 0.4 Nm.

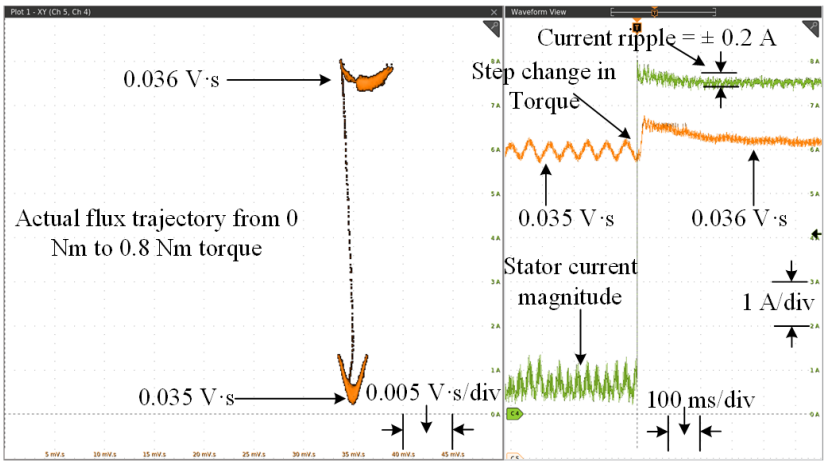

Figure 8.49: Flux trajectory from 0 Nm to 0.8 Nm load torque with ESC activated.

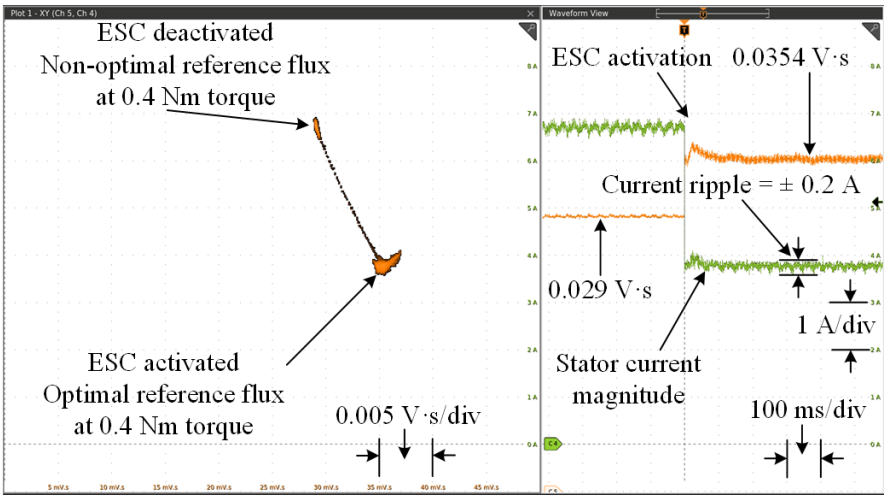

Figure 8.50: ESC effect on stator current and flux trajectory at 0.4 Nm torque.

The dynamic and steady state performance of the ESC and P & O can be discussed from Figure 8.50 and Figure 8.51. The ESC algorithm has advantage on having variable or adaptive step size of the injected signal, therefore, at the optimal point, the ESC can have minimum ripple. In contrast P & O is a fixed step size-based approach, so at the steady state of the optimal point its step size remains fixed which results to high ripple in the stator current than the ESC algorithm.

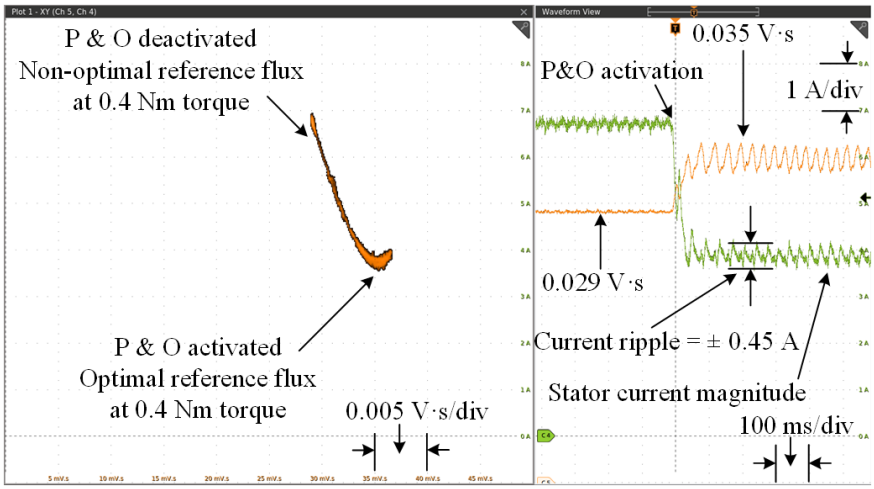

Figure 8.51: P&O effect on stator current and flux trajectory at 0.4 Nm torque.

8.7.3 Steady State Response

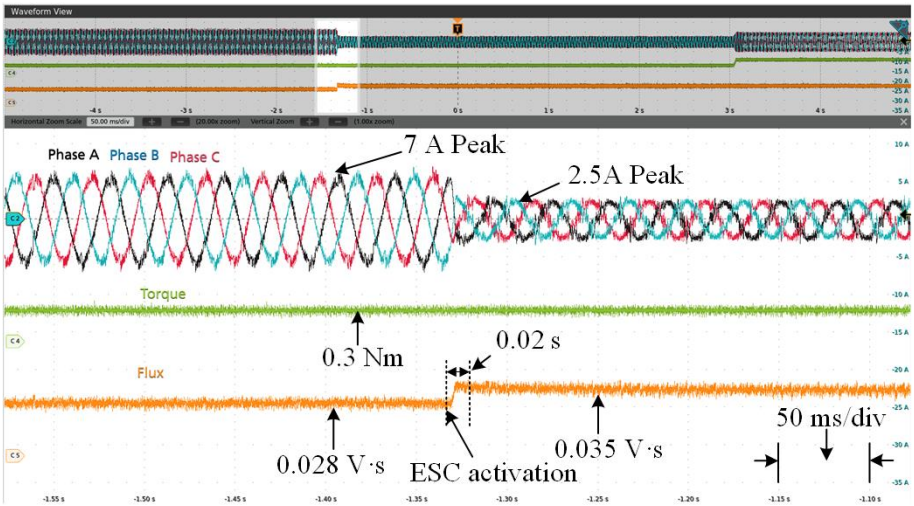

Figure 8.52: Experimental results of three-phase stator currents, torque and $|\psi_s|$ at T^* = 0.3 Nm.

Figure 8.52 shows the experimental results of three-phase stator currents, torque and magnetic flux linkage. Initially the flux reference was set to be 0.028 Vs, while the ESC algorithm is deactivated; the IPM motor operates in a non-optimal operating condition, which is indicated by the peak of the stator currents in Figure 8.52, 7 A. Once the ESC algorithm was enabled, the flux linkage reached to its optimum within 20 ms. The constant output torque is maintained, while the

RMS value of the stator current is reduced from 5 A to 1.8 A. The numerical values are shown in the Figure 8.52.

Based on the motor's parameter shown in Table A-1 in Appendix, the copper loss of the motor reduces from 3.4 W to 0.5 W after the ESC is activated which is a significant reduction in loss. Besides, the average switching frequency of the inverter after ESC activation is almost same as before activating ESC, which are 21.5 kHz and 22 kHz respectively. In other words, the ESC could significantly reduce the copper losses with less impact on the core losses, and the motor efficiency could be remarkably improved.

8.7.4 Transient Response

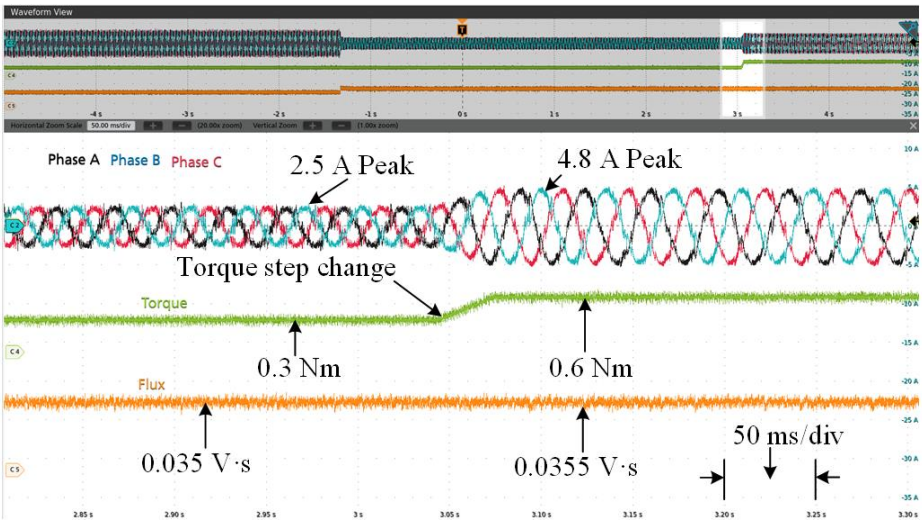

Figure 8.53: Experimental results of three-phase stator currents, torque and $|\psi_s|$ while step change (ramp within 25 ms) applied from 0.3 Nm to 0.6 Nm.

Figure 8.53: shows the dynamic response of the system while the ESC is active by applying a step command in torque reference from 0.3 Nm to 0.6 Nm. The IPM motor torque reaches to its reference value with optimal stator currents without compromising the system stability. To show the variation in the flux linkage properly a step change in the torque reference was applied from 0.3 Nm to 0.7 Nm which is shown in Figure 8.54. When a step change was applied, the flux quickly

reached to its optimal value 0.036 V·s for 0.7 Nm torque which can be located from the MTAP trajectory. The frequency of the injected signal, ω_c is set to be 300 Hz and amplitude is A = 0.00035 V·s, which is 1% of the ψ_s in the experiment.

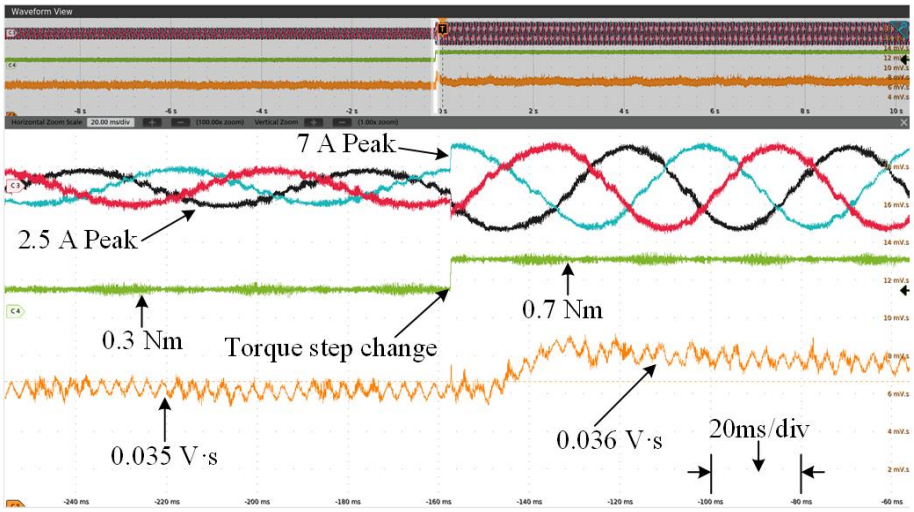

Figure 8.54: Experimental results of three-phase stator currents, torque and $|\psi_s|$ while step change applied from 0.3 Nm to 0.7 Nm.

8.7.5 Stator Current THD

Figure 8.55 and Figure 8.56 indicates the THD (%) before and after enabling the ESC while the T^* = 0.6 Nm and speed is 50 rad/sec. The THD (%) value increase only 0.86% due to high frequency signal injection in flux reference, however the RMS value of the stator current didn't increase. This is to be noted that this additional noise in the stator current can be minimized by manipulating the amplitude of the injected signal.

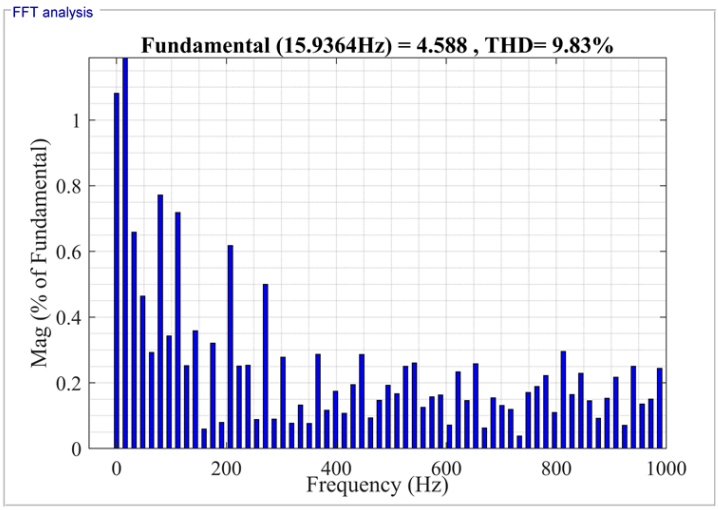

Figure 8.55: Stator currents THD (%) when ESC was deactivated at T^* = 0.6 Nm and 50 rad/sec constant speed.

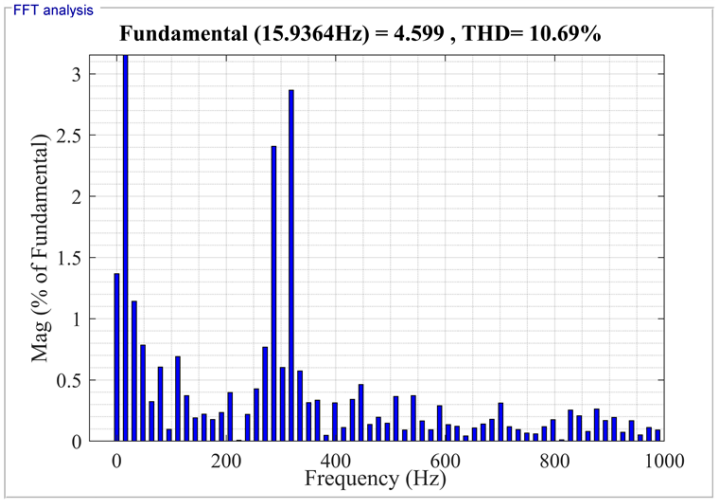

Figure 8.56: Stator currents THD (%) when ESC was activated at T^* = 0.6 Nm and 50 rad/sec constant speed.

CHAPTER 9

CONCLUSIONS, CONTRIBUTIONS AND FUTURE RESEARCH WORK

In this chapter, the objectives of this dissertation are reassessed, and conclusions of the research are illustrated. Moreover, the potential future research work on this topic is discussed.

9.1 Conclusions of This Dissertation

This dissertation was focused on developing a multi objective DTC algorithm for the IPMSM to mitigate the challenges and drawbacks of the conventional DTC. Novel DTC approach for multilevel converter and the signal injection based flux searching approach were proposed, investigated thoroughly and validated using simulation and experimental results.

These proposed methods offer solutions for the problems that the conventional DTC approach holds. The overall dissertation addressed five major issues and the solution related SiC based motor drive systems, which are,

- Virtual voltage vector based Direct Torque control for T-type NPC inverter.
- DC-link capacitor voltages balancing without additional voltage/current sensor for T-type NPC inverter-fed DTC.
- Signal injection based flux searching approach for DTC.
- Stability analysis of the ESC algorithm for DTC.
- Loss model development and analyze loss and efficiency of the system.

In this dissertation, detail research was conducted and analyzed on a novel VSV based DTC, MTPA technique and loss modeling approach for SiC based inverter. Based on the aforementioned problems and solutions, the following conclusions can be drawn.

In chapter 4, system and control-level multi-objective optimization is presented to extract all the benefits of an advanced DTC and 3-L T-type NPC inverters together for traction applications. The main circuit topology is built upon the T-type NPC inverter, which combines the positive aspects of two-level converters including low conduction losses and simple operation principles with the advantages of a 3-L converter such as low switching losses and superior output voltage quality. However, the NP voltage unbalancing is an inherent issue in all neutral point clamped inverters using conventional 3-L DTC which is the main reason for the distorted output voltages and cause extra voltage stresses on the blocking switches and the DC-link capacitors. Uneven charging and discharging of the capacitors C_1 and C_2 occur when any of the output terminals of the 3-L inverter is connected to the neutral point, O. In the voltage vector diagram of the conventional 3-L T-type NPC inverter which was presented in figure 2.6 of Chapter 2, both medium and small voltage vectors contribute to the NP currents. Theoretically, the average NP current within a switching cycle should be nearly zero to keep the capacitor voltage balanced. Generally, the small voltage vector has been utilized to minimize the voltage imbalance at the NP as each of them has their identical pair voltage vector with opposite NP current. Therefore, in conventional control approach for three-level inverter it is necessary to measure the DC-link capacitor voltages to select the appropriate voltage vectors for balancing the DC-link capacitor voltages. The DC-link voltage sensors or the NP current sensors come with additional system cost. Moreover, the unbalanced DC-link capacitor voltages have worse effect on the torque ripples and stators current ripples in the DTC applications. Therefore, in this dissertation a VSV based advanced DTC was proposed to inherently balance the DC-link capacitor voltages without any NP voltage of current sensors.

Signal injection based flux searching approaches were also proposed and discussed in the dissertation since optimal flux searching is a critical issue in the DTC algorithm. In the chapter 5,

two optimal flux searching approaches were presented, i.e., P&O and ESC. The P&O method based optimal flux searching approach is a simple and effective method which is easy to be implemented and effective as well. However, due to fixed injected signal magnitude it affects the steady state performances of the flux. At steady state conditions, the flux ripple is higher if the injected signal magnitude is large. In contrast with the smaller step size of the injected signal the steady state ripples in the electromagnetic flux can be reduced but the dynamic response may be slower. Consequently, the ESC algorithm was proposed to eliminate the issue of the P & O search method. The ESC is a high frequency signal injection based method which does not need the machine parameters to determine the optimal operating condition which can maintain MTPA operation over the whole range of DTC operation. Additionally, the ESC is an adaptive step size based approach so that the steady state flux ripple reduced significantly. The stability analysis was also conducted and analyzed in the chapter 5.

Since the ESC ensures that the PMSM can run under MTPA which can potentially increase the efficiency by reducing the copper loss, it is important to validate the method by analyzing the loss of the system. Hence, in chapter 6 a loss model was developed for the SiC MOSFET based inverter. Accuracy of the loss model was analyzed and validated by building a simulation model and compare the loss and efficiency data with a known system loss data.

At the end, all the proposed methods were supported by the substantial amount of simulation and experimental results provided in the chapter 8.

9.2 Contributions of This Dissertation

The contributions and the accomplishments of this dissertation can be summarized as follows,

- A comprehensive review of the existing state of the art of the DTC approaches with multi-level converter has been presented.

- Issues with the unbalanced DC-link capacitor voltages in the multi-level converter-fed DTC were discussed and their effects on the torque and current ripples were analyzed and showed numerically.
- Advanced VSV based DTC algorithm was proposed to enhance the performance of the conventional DTC for three-level converters. The reduction of the torque and current ripples were validated by the simulation and experimental results. A new voltage vector diagram and switching table was proposed with virtual volage vectors. The VSVs were generated in such a way that none of the VSVs contribute zero NP current over one switching cycle. Therefore, the intrinsic DC-link capacitor voltages balancing is achievable by the proposed DTC algorithm as well.
- Multiple signal injection based optimal flux searching approaches were proposed in this dissertation to obtain the MTPA for the DTC. First the P & O algorithm was implemented which could achieve the MTPA, however, it has large steady state ripple in the flux. Therefore, high frequency signal injection based ESC algorithm was proposed later as an adaptive control approach to find the optimal flux which lead to MTPA for the DTC. The simulation and experimental studies were presented to validate the claim.
- A general electro-thermal characterization procedure was proposed to acquire the detail loss in the system. The proposed loss model was used to compare the loss and the efficiency of the system while implementing the conventional and proposed control algorithms.

9.3 Future Research Recommendations

Future research recommendations are listed below,

- Although the proposed DTC can balance the DC-link capacitor voltages without having any neutral point voltage/current, it should be noted that the DC-link capacitor voltage may

have ripples or even some offset due to fast dynamics of the DTC. Therefore, it is worth exploring the possibility to develop an observer to monitor the DC-link capacitor voltages without any additional sensor.

- Develop a mathematical relationship between he the DC-link capacitor voltages and the torque and stator current ripples. In this dissertation, a numerical analysis has been conducted to show the relationship between the torque, flux ripples and DC-link capacitor voltages due to the complexity of the mathematical model.
- Investigate a way to achieve fixed switching frequency based DTC by even using virtual voltage vectors with external modulator since proposed DTC has variable switching frequency which may cause higher torque ripple than fixed switching frequency.
- Investigate the possibility to implement virtual signal injection based optimal flux searching approach such way the conduction loss introduced by real signal injection based flux searching approach can be minimized.
- The loss model developed in this dissertation can be investigated in detail and an active thermal control algorithm can be used to enhance the efficiency of the DTC system. This active thermal control can be integrated with the existing DTC algorithm and monitor the loss information online.
- Investigate the common mode reduction by implementing the proposed DTC and comparing with the conventional DTC.

BIBLIOGRAPHY

[1] N. Mohan, *Advanced electric drives: analysis, control, and modeling using MATLAB/Simulink*. John wiley & sons, 2014.

[2] B. K. Bose, *Power electronics and motor drives: advances and trends*. Academic press, 2020.

[3] S.-K. Sul, *Control of electric machine drive systems*. John Wiley & Sons, 2011.

[4] J. F. Gieras, *Permanent magnet motor technology: design and applications*. CRC press, 2002.

[5] I. Takahashi and T. Noguchi, "A new quick-response and high-efficiency control strategy of an induction motor," *IEEE Transactions on Industry applications*, no. 5, pp. 820-827, 1986.

[6] M. Depenbrock, "Direct self-control of the flux and rotary moment of a rotary-field machine," ed: Google Patents, 1987.

[7] M. Schweizer and J. W. Kolar, "Design and implementation of a highly efficient three-level T-type converter for low-voltage applications," *IEEE Transactions on Power Electronics*, vol. 28, no. 2, pp. 899-907, 2012.

[8] Y. Ren, Z.-Q. Zhu, and J. Liu, "Direct torque control of permanent-magnet synchronous machine drives with a simple duty ratio regulator," *IEEE Transactions on Industrial Electronics*, vol. 61, no. 10, pp. 5249-5258, 2014.

[9] Z. Zhang, Y. Zhao, W. Qiao, and L. Qu, "A space-vector-modulated sensorless direct-torque control for direct-drive PMSG wind turbines," *IEEE Transactions on Industry Applications*, vol. 50, no. 4, pp. 2331-2341, 2014.

[10] F. Niu, K. Li, and Y. Wang, "Direct torque control for permanent-magnet synchronous machines based on duty ratio modulation," *IEEE Transactions on Industrial Electronics*, vol. 62, no. 10, pp. 6160-6170, 2015.

[11] G. Abad, M. A. Rodriguez, and J. Poza, "Two-level VSC based predictive direct torque control of the doubly fed induction machine with reduced torque and flux ripples at low constant switching frequency," *IEEE transactions on power electronics*, vol. 23, no. 3, pp. 1050-1061, 2008.

[12] Y.-S. Choi, H. H. Choi, and J.-W. Jung, "Feedback linearization direct torque control with reduced torque and flux ripples for IPMSM drives," *IEEE Transactions on Power Electronics*, vol. 31, no. 5, pp. 3728-3737, 2015.

[13] I. M. Alsofyani and K.-B. Lee, "Enhanced Performance of Constant Frequency Torque Controller–Based Direct Torque Control of Induction Machines with Increased Torque-

Loop Bandwidth," *IEEE Transactions on Industrial Electronics,* vol. 67, no. 12, pp. 10168-10179, 2019.

[14] G. Foo, S. Sayeef, and M. Rahman, "Low-speed and standstill operation of a sensorless direct torque and flux controlled IPM synchronous motor drive," *IEEE Transactions on Energy Conversion,* vol. 25, no. 1, pp. 25-33, 2010.

[15] Y. Xu, C. Morito, and R. D. Lorenz, "Extending high-speed operating range of induction machine drives using deadbeat-direct torque and flux control with precise flux weakening," *IEEE Transactions on Industry Applications,* vol. 55, no. 4, pp. 3770-3780, 2019.

[16] J. S. Lee, C.-H. Choi, J.-K. Seok, and R. D. Lorenz, "Deadbeat-direct torque and flux control of interior permanent magnet synchronous machines with discrete time stator current and stator flux linkage observer," *IEEE Transactions on Industry Applications,* vol. 47, no. 4, pp. 1749-1758, 2011.

[17] M. H. Vafaie, B. M. Dehkordi, P. Moallem, and A. Kiyoumarsi, "Minimizing torque and flux ripples and improving dynamic response of PMSM using a voltage vector with optimal parameters," *IEEE Transactions on industrial electronics,* vol. 63, no. 6, pp. 3876-3888, 2015.

[18] F. Ban, G. Lian, J. Zhang, B. Chen, and G. Gu, "Study on a novel predictive torque control strategy based on the finite control set for PMSM," *IEEE Transactions on Applied Superconductivity,* vol. 29, no. 2, pp. 1-6, 2019.

[19] M. N. Uddin and M. M. Rahman, "Online torque-flux estimation-based nonlinear torque and flux control scheme of IPMSM drive for reduced torque ripples," *IEEE Transactions on Power Electronics,* vol. 34, no. 1, pp. 636-645, 2018.

[20] K.-B. Lee, J.-H. Song, I. Choy, and J.-Y. Yoo, "Improvement of low-speed operation performance of DTC for three-level inverter-fed induction motors," *IEEE Transactions on Industrial Electronics,* vol. 48, no. 5, pp. 1006-1014, 2001.

[21] K.-B. Lee, J.-H. Song, I. Choy, and J.-Y. Yoo, "Torque ripple reduction in DTC of induction motor driven by three-level inverter with low switching frequency," *IEEE Transactions on Power Electronics,* vol. 17, no. 2, pp. 255-264, 2002.

[22] P. Naganathan, S. Srinivas, and H. Ittamveettil, "Five-level torque controller-based DTC method for a cascaded three-level inverter fed induction motor drive," *IET power electronics,* vol. 10, no. 10, pp. 1223-1230, 2017.

[23] S. Kouro *et al.*, "Recent advances and industrial applications of multilevel converters," *IEEE Transactions on industrial electronics,* vol. 57, no. 8, pp. 2553-2580, 2010.

[24] W. Jing, I. Rabl, P. Beckedahl, and N. Pluschke, "Performance evaluation of split NPC 3L modules for 1500VDC central solar inverter up to 1.5 MW," in *PCIM Asia 2017; International Exhibition and Conference for Power Electronics, Intelligent Motion, Renewable Energy and Energy Management,* 2017: VDE, pp. 1-6.

[25] Y. Jiao, S. Lu, and F. C. Lee, "Switching performance optimization for high frequency high power 3-level neutral point clamped phase leg," in *2013 IEEE Energy Conversion Congress and Exposition*, 2013: IEEE, pp. 3949-3956.

[26] J. Rodriguez, S. Bernet, P. K. Steimer, and I. E. Lizama, "A survey on neutral-point-clamped inverters," *IEEE transactions on Industrial Electronics,* vol. 57, no. 7, pp. 2219-2230, 2009.

[27] Z. Wang, Y. Wu, M. H. Mahmud, Z. Zhao, Y. Zhao, and H. A. Mantooth, "Design and validation of a 250-kw all-silicon carbide high-density three-level t-type inverter," *IEEE Journal of Emerging and Selected Topics in Power Electronics,* vol. 8, no. 1, pp. 578-588, 2019.

[28] Y. Zhao, M. H. Mahmud, and L. Wang, "An online optimal reference flux searching approach for direct torque control of interior permanent magnet synchronous machines," in *IECON 2017-43rd Annual Conference of the IEEE Industrial Electronics Society*, 2017: IEEE, pp. 1790-1795.

[29] M. H. Mahmud, Y. Wu, W. Alhosaini, F. Diao, and Y. Zhao, "A High Frequency Signal Injection based Optimum Reference Flux Searching for Direct Torque Control of a Three-Level Traction Drive," in *2019 IEEE Energy Conversion Congress and Exposition (ECCE)*, 2019: IEEE, pp. 4540-4545.

[30] M. H. Mahmud, Y. Wu, and Y. Zhao, "Extremum Seeking-Based Optimum Reference Flux Searching for Direct Torque Control of Interior Permanent Magnet Synchronous Motors," *IEEE Transactions on Transportation Electrification,* vol. 6, no. 1, pp. 41-51, 2019.

[31] H.-c. Chen, M.-j. Tsai, Y.-b. Wang, and P.-t. Cheng, "A novel neutral point potential control for the three-level neutral-point-clamped converter," in *2016 IEEE Energy Conversion Congress and Exposition (ECCE)*, 2016: IEEE, pp. 1-7.

[32] N. Celanovic and D. Boroyevich, "A comprehensive study of neutral-point voltage balancing problem in three-level neutral-point-clamped voltage source PWM inverters," *IEEE Transactions on power electronics,* vol. 15, no. 2, pp. 242-249, 2000.

[33] G. H. B. Foo, T. Ngo, X. Zhang, and M. F. Rahman, "SVM direct torque and flux control of three-level simplified neutral point clamped inverter fed interior pm synchronous motor drives," *IEEE/ASME Transactions on Mechatronics,* vol. 24, no. 3, pp. 1376-1385, 2019.

[34] D. Mohan, X. Zhang, and G. H. B. Foo, "A simple duty cycle control strategy to reduce torque ripples and improve low-speed performance of a three-level inverter fed DTC IPMSM drive," *IEEE Transactions on Industrial Electronics,* vol. 64, no. 4, pp. 2709-2721, 2016.

[35] D. Mohan, X. Zhang, and G. H. B. Foo, "Three-level inverter-fed direct torque control of IPMSM with constant switching frequency and torque ripple reduction," *IEEE Transactions on Industrial Electronics,* vol. 63, no. 12, pp. 7908-7918, 2016.

[36] S. Bolognani, L. Peretti, and M. Zigliotto, "Online MTPA control strategy for DTC synchronous-reluctance-motor drives," *IEEE Transactions on Power Electronics,* vol. 26, no. 1, pp. 20-28, 2010.

[37] C. Mademlis, I. Kioskeridis, and N. Margaris, "Optimal efficiency control strategy for interior permanent-magnet synchronous motor drives," *IEEE Transactions on Energy Conversion,* vol. 19, no. 4, pp. 715-723, 2004.

[38] S.-Y. Jung, J. Hong, and K. Nam, "Current minimizing torque control of the IPMSM using Ferrari's method," *IEEE Transactions on Power Electronics,* vol. 28, no. 12, pp. 5603-5617, 2013.

[39] T. Inoue, Y. Inoue, S. Morimoto, and M. Sanada, "Mathematical model for MTPA control of permanent-magnet synchronous motor in stator flux linkage synchronous frame," *IEEE Transactions on Industry Applications,* vol. 51, no. 5, pp. 3620-3628, 2015.

[40] Y.-s. Jeong, S. Sul, S. Hiti, and K. M. Rahman, "Online minimum-copper-loss control of an interior permanent-magnet synchronous machine for automotive applications," *IEEE Transactions on Industry Applications,* vol. 42, no. 5, pp. 1222-1229, 2006.

[41] T. Matsuo, A. El-Antably, and T. A. Lipo, "A new control strategy for optimum-efficiency operation of a synchronous reluctance motor," *IEEE Transactions on Industry Applications,* vol. 33, no. 5, pp. 1146-1153, 1997.

[42] S. Vaez, V. John, and M. Rahman, "An on-line loss minimization controller for interior permanent magnet motor drives," *IEEE Transactions on Energy Conversion,* vol. 14, no. 4, pp. 1435-1440, 1999.

[43] A. Dianov, K. Young-Kwan, L. Sang-Joon, and L. Sang-Taek, "Robust self-tuning MTPA algorithm for IPMSM drives," in *2008 34th Annual Conference of IEEE Industrial Electronics*, 2008: IEEE, pp. 1355-1360.

[44] T. Sun, J. Wang, and X. Chen, "Maximum torque per ampere (MTPA) control for interior permanent magnet synchronous machine drives based on virtual signal injection," *IEEE Transactions on Power Electronics,* vol. 30, no. 9, pp. 5036-5045, 2014.

[45] T. Sun, J. Wang, and M. Koc, "Virtual signal injection-based direct flux vector control of IPMSM drives," *IEEE Transactions on Industrial Electronics,* vol. 63, no. 8, pp. 4773-4782, 2016.

[46] Q. Chen, W. Zhao, G. Liu, and Z. Lin, "Extension of virtual-signal-injection-based MTPA control for five-phase IPMSM into fault-tolerant operation," *IEEE Transactions on Industrial Electronics,* vol. 66, no. 2, pp. 944-955, 2018.

[47] R. Lagerquist, I. Boldea, and T. J. Miller, "Sensorless-control of the synchronous reluctance motor," *IEEE Transactions on Industry Applications,* vol. 30, no. 3, pp. 673-682, 1994.

[48] Y. Inoue, S. Morimoto, and M. Sanada, "A novel control scheme for maximum power operation of synchronous reluctance motors including maximum torque per flux control," in *2009 International Conference on Electrical Machines and Systems*, 2009: IEEE, pp. 1-6.

[49] M. Barzegaran, M. Kamruzzaman, H. Mahmud, and O. Mohammed, "Direct torque control of permanent magnet synchronous machine using Sparse matrix converter with SiC switches," in *2015 IEEE International Electric Machines & Drives Conference (IEMDC)*, 2015: IEEE, pp. 1683-1688.

[50] A. Shinohara, Y. Inoue, S. Morimoto, and M. Sanada, "Direct calculation method of reference flux linkage for maximum torque per ampere control in DTC-based IPMSM drives," *IEEE Transactions on Power Electronics*, vol. 32, no. 3, pp. 2114-2122, 2016.

[51] A. Shinohara, Y. Inoue, S. Morimoto, and M. Sanada, "A calculation method of reference flux to realize maximum torque per ampere control in direct torque controlled permanent magnet synchronous motor drives," in *2013 IEEE 10th International Conference on Power Electronics and Drive Systems (PEDS)*, 2013: IEEE, pp. 205-210.

[52] A. Shinohara, Y. Inoue, S. Morimoto, and M. Sanada, "Correction of reference flux for MTPA control in direct torque controlled interior permanent magnet synchronous motor drives," in *2014 International Power Electronics Conference (IPEC-Hiroshima 2014-ECCE ASIA)*, 2014: IEEE, pp. 324-329.

[53] D. Jones, "A new buried magnet brushless PM motor for a traction application," in *Proceedings: Electrical Insulation Conference and Electrical Manufacturing and Coil Winding Technology Conference (Cat. No. 03CH37480)*, 2003: IEEE, pp. 421-429.

[54] P. C. Sen, *Principles of electric machines and power electronics*. John Wiley & Sons, 2007.

[55] S. T. Lee, "Development and Analysis of Interior Permanent Magnet Synchronous Motor with Field Excitation Structure," PhD Dissertation, University of Tennessee - Knoxville, 2009. [Online]. Available: https://citeseerx.ist.psu.edu/viewdoc/download?doi=10.1.1.817.9744&rep=rep1&type=pdf

[56] O. Ojo, "The generalized discontinuous PWM scheme for three-phase voltage source inverters," *IEEE Transactions on Industrial Electronics*, vol. 51, no. 6, pp. 1280-1289, 2004.

[57] N. Mohan, T. M. Undeland, and W. P. Robbins, *Power electronics: converters, applications, and design*. John wiley & sons, 2003.

[58] P. H. Chappell, *Introduction to power electronics*. Artech House, 2013.

[59] B. Bose, "Modern Power Electronics and AC Drives Prentice Hall PTR," *Upper Saddle River*, 2002.

[60] J. Wang, B. Yang, J. Zhao, Y. Deng, X. He, and X. Zhixin, "Development of a compact 750KVA three-phase NPC three-level universal inverter module with specifically designed busbar," in *2010 Twenty-Fifth Annual IEEE Applied Power Electronics Conference and Exposition (APEC)*, 2010: IEEE, pp. 1266-1271.

[61] Y. Jiao, S. Lu, and F. C. Lee, "Switching performance optimization of a high power high frequency three-level active neutral point clamped phase leg," *IEEE Transactions on power electronics*, vol. 29, no. 7, pp. 3255-3266, 2013.

[62] J. Weidong, L. Wang, J. Wang, X. Zhang, and P. Wang, "A carrier-based virtual space vector modulation with active neutral-point voltage control for a neutral-point-clamped three-level inverter," *IEEE Transactions on Industrial Electronics*, vol. 65, no. 11, pp. 8687-8696, 2018.

[63] Z. Wang *et al.*, "A compact 250 kW silicon carbide MOSFET based three-level traction inverter for heavy equipment applications," in *2018 IEEE Transportation Electrification Conference and Expo (ITEC)*, 2018: IEEE, pp. 1129-1134.

[64] J. Pou, R. Pindado, D. Boroyevich, and P. Rodríguez, "Evaluation of the low-frequency neutral-point voltage oscillations in the three-level inverter," *IEEE transactions on industrial electronics*, vol. 52, no. 6, pp. 1582-1588, 2005.

[65] T. Adamson, "Design and Optimization of a High Power Density Silicon Carbide Traction Inverter," 2019.

[66] P. C. Perera, F. Blaabjerg, J. K. Pedersen, and P. Thogersen, "A sensorless, stable V/f control method for permanent-magnet synchronous motor drives," *IEEE Transactions on Industry Applications*, vol. 39, no. 3, pp. 783-791, 2003.

[67] B. K. Bose, "Power electronics and AC drives," *Englewood Cliffs*, 1986.

[68] J. Cai, "Implementation and Analysis of Direct Torque Control for Permanent Magnet Synchronous Motor Using Gallium Nitride based Inverter," 2018.

[69] F. Blaschke, "The principle of field orientation as applied to the new TRANSVECTOR closed loop control system for rotating field machines," *Siemens review*, vol. 34, no. 5, pp. 217-220, 1972.

[70] D. W. Novotny and T. A. Lipo, *Vector control and dynamics of AC drives*. Oxford university press, 1996.

[71] G. S. Buja and M. P. Kazmierkowski, "Direct torque control of PWM inverter-fed AC motors-a survey," *IEEE Transactions on industrial electronics*, vol. 51, no. 4, pp. 744-757, 2004.

[72] P. Vas, *Sensorless vector and direct torque control*. Oxford Univ. Press, 1998.

[73] R. Krishnan, *Electric motor drives: modeling, analysis, and control*. Pearson, 2001.

[74] L. Zhong, M. F. Rahman, W. Y. Hu, and K. Lim, "Analysis of direct torque control in permanent magnet synchronous motor drives," *IEEE transactions on power electronics,* vol. 12, no. 3, pp. 528-536, 1997.

[75] H. Le-Huy, "Comparison of field-oriented control and direct torque control for induction motor drives," in *Conference record of the 1999 IEEE industry applications conference. Thirty-forth IAS annual meeting (Cat. No. 99CH36370)*, 1999, vol. 2: IEEE, pp. 1245-1252.

[76] C. French and P. Acarnley, "Direct torque control of permanent magnet drives," *IEEE Transactions on Industry Applications,* vol. 32, no. 5, pp. 1080-1088, 1996.

[77] Z. Zhang, "Direct Torque Control of Permanent Magnet Synchronous Machines with Applications to Motor Drives and Wind Energy Conversion Systems," 2015.

[78] G. F. H. Beng, "Sensorless direct torque and flux control of interior permanent magnet synchronous motors at very low speeds including standstill," *Ph. D. dissertation,* 2010.

[79] L. Jian and L. Shi, "Stability analysis for direct torque control of permanent magnet synchronous motors," in *2005 International Conference on Electrical Machines and Systems*, 2005, vol. 2: IEEE, pp. 1672-1675.

[80] J. Weidong *et al.*, "A novel modulation strategy with unconditional neutral point voltage balance and three switching actions in one switching cycle for neutral point clamped three-level converter," *IEEE Transactions on Industrial Electronics,* vol. 66, no. 7, pp. 5025-5038, 2018.

[81] W. Alhosaini, Y. Wu, and Y. Zhao, "An enhanced model predictive control using virtual space vectors for grid-connected three-level neutral-point clamped inverters," *IEEE Transactions On Energy Conversion,* vol. 34, no. 4, pp. 1963-1972, 2019.

[82] G. Brando, A. Dannier, A. Del Pizzo, R. Rizzo, and I. Spina, "Generalised look-up table concept for direct torque control in induction drives with multilevel inverters," *IET Electric Power Applications,* vol. 9, no. 8, pp. 556-567, 2015.

[83] C. Zhu, Z. Zeng, and R. Zhao, "Comprehensive analysis and reduction of torque ripples in three-phase four-switch inverter-fed PMSM drives using space vector pulse-width modulation," *Ieee transactions on power electronics,* vol. 32, no. 7, pp. 5411-5424, 2016.

[84] S. Busquets-Monge, J. Bordonau, D. Boroyevich, and S. Somavilla, "The nearest three virtual space vector PWM-a modulation for the comprehensive neutral-point balancing in the three-level NPC inverter," *IEEE power electronics letters,* vol. 2, no. 1, pp. 11-15, 2004.

[85] W. S. S. Alhosaini, "A Virtual Space Vectors based Model Predictive Control for Three-Level Converters," 2020.

[86] W. Alhosaini, F. Diao, M. H. Mahmud, Y. Wu, and Y. Zhao, "A Virtual Space Vectors based Model Predictive Control for Inherent DC Link Voltage Balancing of Three-Level

T-Type Converters," *IEEE Journal of Emerging and Selected Topics in Power Electronics*, 2020.

[87] T. Miyajima, H. Fujimoto, and M. Fujitsuna, "A precise model-based design of voltage phase controller for IPMSM," *IEEE Transactions on Power Electronics*, vol. 28, no. 12, pp. 5655-5664, 2013.

[88] K. Renu, N. K. Kumari, and D. R. Kumar, "Flux Weakening Operation of PMSM with Hysteresis PWM Current Controller," in *2017 14th IEEE India Council International Conference (INDICON)*, 2017: IEEE, pp. 1-6.

[89] R. Antonello, M. Carraro, and M. Zigliotto, "Towards the automatic tuning of MTPA algorithms for IPM motor drives," in *2012 XXth International Conference on Electrical Machines*, 2012: IEEE, pp. 1121-1127.

[90] S. Morimoto, M. Sanada, and Y. Takeda, "Wide-speed operation of interior permanent magnet synchronous motors with high-performance current regulator," *IEEE Transactions on Industry Applications*, vol. 30, no. 4, pp. 920-926, 1994.

[91] T. Sun, J. Wang, and M. Koc, "Self-learning direct flux vector control of interior permanent-magnet machine drives," *IEEE Transactions on Power Electronics*, vol. 32, no. 6, pp. 4652-4662, 2016.

[92] R. Antonello, M. Carraro, and M. Zigliotto, "Maximum-torque-per-ampere operation of anisotropic synchronous permanent-magnet motors based on extremum seeking control," *IEEE Transactions on Industrial Electronics*, vol. 61, no. 9, pp. 5086-5093, 2013.

[93] S. Kim, Y.-D. Yoon, S.-K. Sul, and K. Ide, "Maximum torque per ampere (MTPA) control of an IPM machine based on signal injection considering inductance saturation," *IEEE Transactions on Power Electronics*, vol. 28, no. 1, pp. 488-497, 2012.

[94] S. Bolognani, R. Petrella, A. Prearo, and L. Sgarbossa, "Automatic tracking of MTPA trajectory in IPM motor drives based on AC current injection," *IEEE Transactions on Industry Applications*, vol. 47, no. 1, pp. 105-114, 2010.

[95] T. Sun, J. Wang, M. Koc, and X. Chen, "Self-learning MTPA control of interior permanent-magnet synchronous machine drives based on virtual signal injection," *IEEE Transactions on Industry Applications*, vol. 52, no. 4, pp. 3062-3070, 2016.

[96] T. Sun and J. Wang, "Extension of virtual-signal-injection-based MTPA control for interior permanent-magnet synchronous machine drives into the field-weakening region," *IEEE Transactions on Industrial Electronics*, vol. 62, no. 11, pp. 6809-6817, 2015.

[97] Y. Tan, W. H. Moase, C. Manzie, D. Nešić, and I. M. Mareels, "Extremum seeking from 1922 to 2010," in *Proceedings of the 29th Chinese control conference*, 2010: IEEE, pp. 14-26.

[98] R. Leyva, C. Alonso, I. Queinnec, A. Cid-Pastor, D. Lagrange, and L. Martinez-Salamero, "MPPT of photovoltaic systems using extremum-seeking control," *IEEE transactions on aerospace and electronic systems,* vol. 42, no. 1, pp. 249-258, 2006.

[99] Y. Zhao, C. Wei, Z. Zhang, and W. Qiao, "A review on position/speed sensorless control for permanent-magnet synchronous machine-based wind energy conversion systems," *IEEE Journal of Emerging and Selected Topics in Power Electronics,* vol. 1, no. 4, pp. 203-216, 2013.

[100] K. B. Ariyur and M. Krstić, *Real time optimization by extremum seeking control*. Wiley Online Library, 2003.

[101] K. J. Åström and B. Wittenmark, *Adaptive control*. Courier Corporation, 2013.

[102] M. Krstic and H.-H. Wang, "Stability of extremum seeking feedback for general nonlinear dynamic systems," *Automatica,* vol. 36, no. 4, pp. 595-601, 2000.

[103] H.-H. Wang and M. Krstic, "Extremum seeking for limit cycle minimization," *IEEE Transactions on Automatic control,* vol. 45, no. 12, pp. 2432-2436, 2000.

[104] H. K. Khalil and J. W. Grizzle, *Nonlinear systems*. Prentice hall Upper Saddle River, NJ, 2002.

[105] T. Salem, D. Urciuoli, R. Green, and G. Ovrebo, "High-temperature high-power operation of a 100 A SiC DMOSFET module," in *2009 Twenty-Fourth Annual IEEE Applied Power Electronics Conference and Exposition*, 2009: IEEE, pp. 653-657.

[106] H. Sheng, Z. Chen, F. Wang, and A. Millner, "Investigation of 1.2 kV SiC MOSFET for high frequency high power applications," in *2010 Twenty-Fifth Annual IEEE Applied Power Electronics Conference and Exposition (APEC)*, 2010: IEEE, pp. 1572-1577.

[107] S. Hazra, S. Madhusoodhanan, G. K. Moghaddam, K. Hatua, and S. Bhattacharya, "Design considerations and performance evaluation of 1200-V 100-A SiC MOSFET-based two-level voltage source converter," *IEEE Transactions on Industry Applications,* vol. 52, no. 5, pp. 4257-4268, 2016.

[108] A. Nawawi *et al.*, "Design of high power density converter for aircraft applications," in *2015 International Conference on Electrical Systems for Aircraft, Railway, Ship Propulsion and Road Vehicles (ESARS)*, 2015: IEEE, pp. 1-6.

[109] S. Yin *et al.*, "Gate driver optimization to mitigate shoot-through in high-speed switching SiC half bridge module," in *2015 IEEE 11th International Conference on Power Electronics and Drive Systems*, 2015: IEEE, pp. 484-491.

[110] S. Yin *et al.*, "An accurate subcircuit model of SiC half-bridge module for switching-loss optimization," *IEEE Transactions on Industry Applications,* vol. 53, no. 4, pp. 3840-3848, 2017.

[111] P. Tu, P. Wang, X. Hu, C. Qi, S. Yin, and M. A. Zagrodnik, "Analytical evaluation of IGBT turn-on loss with double pulse testing," in *2016 IEEE 11th Conference on Industrial Electronics and Applications (ICIEA)*, 2016: IEEE, pp. 963-968.

[112] X. Gong and J. A. Ferreira, "Investigation of conducted EMI in SiC JFET inverters using separated heat sinks," *IEEE transactions on industrial electronics*, vol. 61, no. 1, pp. 115-125, 2013.

[113] Z. Zhang, F. Wang, L. M. Tolbert, and B. J. Blalock, "Active gate driver for crosstalk suppression of SiC devices in a phase-leg configuration," *IEEE Transactions on Power Electronics*, vol. 29, no. 4, pp. 1986-1997, 2013.

[114] L. Ceccarelli, R. Kotecha, F. Iannuzzo, and A. Mantooth, "Fast Electro-thermal Simulation Strategy for SiC MOSFETs Based on Power Loss Mapping," in *2018 IEEE International Power Electronics and Application Conference and Exposition (PEAC)*, 2018: IEEE, pp. 1-6.

[115] M. Jin, Q. Gao, Y. Wang, and D. Xu, "A temperature-dependent SiC MOSFET modeling method based on MATLAB/simulink," *IEEE Access*, vol. 6, pp. 4497-4505, 2017.

[116] X. Wang, Z. Zhao, K. Li, Y. Zhu, and K. Chen, "Analytical methodology for loss calculation of SiC MOSFETs," *IEEE Journal of Emerging and Selected Topics in Power Electronics*, vol. 7, no. 1, pp. 71-83, 2018.

[117] M. R. Ahmed, R. Todd, and A. J. Forsyth, "Predicting SiC MOSFET behavior under hard-switching, soft-switching, and false turn-on conditions," *IEEE Transactions on Industrial Electronics*, vol. 64, no. 11, pp. 9001-9011, 2017.

[118] Y. Ren, M. Xu, J. Zhou, and F. C. Lee, "Analytical loss model of power MOSFET," *IEEE transactions on power electronics*, vol. 21, no. 2, pp. 310-319, 2006.

[119] M. Feurtado *et al.*, "High-performance 300 kW 3-phase SiC inverter based on next generation modular SiC power modules," in *PCIM Europe 2019; International Exhibition and Conference for Power Electronics, Intelligent Motion, Renewable Energy and Energy Management*, 2019: VDE, pp. 1-8.

[120] Wolfpseed, "CAB450M12XM3," 2019-06-01. [Online]. Available: https://www.wolfspeed.com/downloads/dl/file/id/1493/product/482/cab450m12xm3.pdf

[121] "1200V Silicon Carbide MOSFETs 1.2 kV, 160 mΩ." [Online]. Available: https://www.wolfspeed.com/downloads/dl/file/id/1647/product/643/c3m0160120d.pdf

APPENDIX

Table A-1
Machine Parameters Used in the Dissertation

Nominal Power	250 W
Maximum torque	0.8 Nm
Flux linkage	0.035Wb
Average L_d	1.12 mH
Average L_q	1.58 mH
Base speed	3000 RPM
Pole-pair number, P	2
Stator resistance, R	0.27 Ω

Define $\Delta L = L_d - L_q$, The expressions of g, l, h, and m in (5.16-b) are

$$l(i_d) = 2a\Delta L(\psi_m + \Delta L i_d)$$

$$a(i_d) = 9P^2\Delta L^2 i_d^4 + 9P^2\Delta L\psi_m i_d^3 + 9P^2\psi_m^2 + 4T_{em,0}^2$$

$$m(i_d) = b\Delta L(\psi_m + \Delta L i_d)$$

$$b(i_d) = \psi_m^4 + 2\psi_m^3\Delta L i_d + \Delta L^2\psi_m^2 i_d^2 + 2\psi_m^3 L_d i_d + 4\psi_m^2 L_d\Delta L i_d^2 + 2\psi_m L_d\Delta L^2 i_d^3 + \Delta L^2 {L_d}^2 i_d^4 + 2\psi_m {L_d}^2\Delta L i_d^3$$

$$g(i_d) = 9P^2\Delta L i_d^2 \cdot (\Delta L^2 i_d^2 + \psi_m\Delta L i_d + \psi_m^2) \times (4\Delta L i_d + 3\psi_m)$$

$$h(i_d) = 9P^2(\psi_m + \Delta L i_d)^2 \times \begin{pmatrix} \Delta L\psi_m^3 + \Delta L^2\psi_m^2 i_d + L_d\psi_m^3 + \\ 4\psi_m^2 L_d\Delta L i_d + 3\psi_m L_d\Delta L^2 i_d^2 + \\ 2\Delta L^2 L_d^2 i_d^3 + 3\psi_m\Delta L {L_d}^2 i_d^2 \end{pmatrix}$$

Table A-2
Major Parameters of XM3 Power Module

Drain-Source Voltage	1200 V
DC Continuous Drain Current	450 A
Maximum Virtual Junction Temperature under Switching Conditions	-40ºC to 175 ºC
Internal Gate Resistance	2.5 Ω

Table A-3
Major Parameters of Loss model for Operating Condition-1

Nominal Power	200 kW
Power factor	0.82
Dead time	1e-6
$R_{j\rightarrow case}$	0.11 (Datasheet XM3)
$R_{case\rightarrow cold\ plate}$	0.0036 (thermal paste)
$R_{cold\ plate\rightarrow coolant}$	0.016 (Datasheet CP3012)
R_{gext}	1 Ω
Fundamental frequency	400 Hz
f_{sw}	20 kHz; 16 kHz; 12 kHz
$T_{coolant}$	105ºC; 85ºC; 75ºC

Table A-4
Major Parameters of Loss model for Operating Condition-2

Nominal Power	300 kW
Power factor	1
Dead time	1e-6
$R_{j\rightarrow case}$	0.11 (Datasheet XM3)
$R_{case\rightarrow cold\ plate}$	0.0036 (thermal paste)
$R_{cold\ plate\rightarrow coolant}$	0.016 (Datasheet CP3012)
R_{gext}	1 Ω
Fundamental frequency	300 Hz
f_{sw}	20 kHz; 15 kHz; 10 kHz
$T_{coolant}$	30ºC

Table A-5
Machine Parameters Used in the Dissertation

Nominal Power	300 W
Maximum torque	2 Nm
Flux linkage	0.0138Wb
Average L_d	0.275 mH
Average L_q	0.364 mH
Base speed	2500 RPM
Pole-pair number, P	4
Stator resistance, R	0.23 Ω